STRUCTURAL AND THERAPEUTIC INSIGHTS FROM THE HIV-1 RNA GENOME

Justin Thomas Low

A dissertation submitted to the faculty of the University of North Carolina at Chapel Hill in partial fulfillment of the requirements for the degree of Doctor of Philosophy in the Department of Biochemistry and Biophysics.

Chapel Hill
2012

Approved by:

Howard M. Fried, Ph.D

Brian Kuhlman, Ph.D

Ronald I. Swanstrom, Ph.D

Kevin M. Weeks, Ph.D

David A. Wohl, M.D.

Abstract

JUSTIN LOW: Structural and Therapeutic Insights from the HIV-1 RNA Genome
(Under the direction of Kevin M. Weeks)

Infection with HIV currently affects an estimated 30-36 million people throughout the world. Due in part to the poor replication fidelity of this RNA virus, resistance to antiretrovirals develops rapidly. Finding new ways of targeting HIV is therefore an ever urgent need. However, despite the wealth of ongoing research in HIV drug development, most new drug candidates continue to target only a few well-defined protein domains, chosen for their functional importance in HIV replication. Targeting the RNA genome itself in a structure-directed manner presents an opportunity to greatly expand the repertoire of potential target sites for anti-HIV therapeutics. We use a high-resolution SHAPE-directed secondary structure model of an entire HIV-1 RNA genome (1) to refine existing models of the Gag-Pol frameshift element, an important regulatory element and promising therapeutic target, and (2) to investigate the structural determinants for RNAi-based inhibition of HIV-1. We show that the Gag-Pol frameshift element folds into a complex structure that is distinct from currently accepted models and capable of switching between two different conformations. Additionally, we discovered that there exists a strong correlation between shRNA-mediated inhibition of HIV-1 production in a quantitative cell-based

assay and very simple thermodynamic features in the SHAPE-directed RNA genome structure model. Both of these results are highly dependent on having an accurate secondary structural model, as obtained by SHAPE data. We anticipate that these results will be broadly applicable to RNA-directed antiretroviral development efforts.

To my parents

Acknowledgements

I am grateful to many advisors, peers, friends, and family who have enriched my graduate experience. I wish to especially thank:

My advisor, Dr. Kevin Weeks, for his enthusiasm and encouragement throughout my graduate career.

Fellow Weeks lab members, for four fun years of science, friendship, and entertainment.

My thesis committee members, for their time, advice and interest in my work.

Dr. Robert Gorelick, for producing HIV RNA and for entertaining so many viral assay requests and ideas.

Drs. Steffie Knoepfel and Ben Berkhout, for their indispensable role in our shRNA collaboration.

Dr. Eugene Orringer and the staff, students, and advisors of the MD-PhD program, for their continuing support.

My family, for their love and support.

Table of Contents

List of Tables

List of Figures

List of Abbreviations

ΔG	Gibbs free energy
1M6	1-methyl-6-nitroisatoic anhydride
1M7	1-methyl-7-nitroisatoic anhydride
AIDS	Acquired immune deficiency syndrome
CA	Capsid protein
cDNA	complementary DNA
CMV	cytomegalovirus
DMEM	Dulbecco's modified Eagle's medium
DNA	deoxyribonucleic acid
dNTP	deoxynucleotide triphosphate
DMSO	dimethyl sulfoxide
DTT	dithriotreitol
EDTA	ethylenediaminetetraacetic acid
ELISA	Enzyme-linked immunosorbent assay
ex virio	Latin expression meaning extracted from virions
FACS	Fluorescence-activated cell sorting
FCS	fetal calf serum
Gag	Group-specific antigen
GFP	Green fluorescent protein

HEPES	N-2-hydroxyethylpiperazine-N'-2-ethanesulfonic acid
HIV	Human immunodeficiency virus
in vitro	Latin expression meaning in a test tube
in virio	Latin expression meaning inside virions
IRES	Internal ribosomal entry site
kcal	kilocalorie
KOAc	potassium acetate
Leu	Leucine
LNA	locked nucleic acid
MOI	multiplicity of infection
mRNA	messenger RNA
N	number of nucleotides in an RNA
NED	proprietary fluorescent dye
NMIA	N-methylisatoic anhydride
NMR	nuclear magnetic resonance
NN	nearest neighbor
nt	nucleotide
NTP	nucleotide triphosphate
O	Big O notation, the response of an algorithm to changes in input size
Phe	Phenylalanine
PI	protease inhibitor
Pol	precursor polyprotein for retroviral enzymes
PPV	positive predictive value

r	Pearson product-moment correlation coefficient
RISC	RNA-induced silencing complex
RNA	ribonucleic acid
RNAi	RNA interference
rRNA	ribosomal RNA
SHAPE	Selective 2'-Hydroxyl Acylation analyzed by Primer Extension
shRNA	short hairpin RNA
siRNA	short interfering RNA
TE	10 mM Tris (pH 7.5), 1 mM EDTA
Tris	tris(hydroxymethyl)aminomethane
tRNA	transfer RNA
VIC	proprietary fluorescent dye

CHAPTER 1

INTRODUCTION

1.1 Introduction

Infec[1]tion with human immunodeficiency virus (HIV) is a major public health concern. HIV is a positive-sense RNA retrovirus that infects cells of the immune system such as T helper cells and macrophages. Ultimately, the destruction of these cells renders the host susceptible to numerous infections that a healthy immune system would suppress. These are termed opportunistic infections and are the clinical hallmarks of acquired immune deficiency syndrome (AIDS). During latent HIV infection, a copy of the viral genome is incorporated into the genomic DNA of infected immune cells. Mitigating the disease progression to AIDS therefore requires lifelong treatment with antiretroviral drugs, and there remains a need for new classes of antiretroviral medications. All current therapeutic approaches target processes crucial to the viral replication cycle.

The replication cycle begins when an HIV virion recognizes target host cells via binding of glycoproteins on the viral envelope with host cell receptors. This binding event triggers the fusion of viral and host cell plasma membranes allowing entry of viral contents into the host cell. The viral contents contain two copies of the viral genome

---

Portions of this chapter have been published in Low, J.T. and Weeks, K.M. *Methods.* 2010. **52**:150-158.

packaged with structural proteins matrix, capsid, and nucleocapsid, and viral enzymes reverse transcriptase, integrase, and protease. This package is uncoated to release the RNA genome and viral enzymes. The RNA genome is used as a template for reverse transcription into cDNA by the viral reverse transcriptase. Following transport to the nucleus, the double-stranded DNA product is integrated into the host cell genome by the viral integrase enzyme. Once integrated, full-length viral RNA can be generated by the host transcriptional machinery. This RNA can function as genomic RNA, mRNA for Gag and Gag-Pol, or spliced to form subgenomic mRNA. These viral mRNAs are translated by host ribosomes and the resulting precursor proteins are assembled together with two copies of the RNA genome. This assembly buds out of the host cell, taking part of the cell membrane as its envelope. Precursor proteins within this immature viral particle then undergo proteolytic cleavage via the action of the viral protease enzyme to generate the mature, infectious particle.

1.2 The HIV RNA as a target for antiretrovirals

In principle, each step of this replication cycle could be a target for antiretroviral therapeutics. Currently available drugs target critical proteins involved in four of these stages. Three of these classes of drugs target the three viral enzymes (reverse transcriptase, protease, and integrase), while the fourth targets proteins involved in fusion of virus and host cell membranes. However, no existing drugs target the HIV RNA, which is a central player in many stages of the replication cycle. The high mutation rate of HIV poses special challenges for the development of antiretroviral medications. Nevertheless, the relatively short length of the HIV genome (~9200

nucleotides) means that the essential, evolutionarily stable, replication information encoded within the genome must be relatively densely packed.

1.3 Structure-based targeting of HIV-1 RNA

In principle, the regular base-pairing properties of RNA make designing oligonucleotide inhibitors conceptually straightforward, as one simply uses the reverse complement of target sequences. However, RNA folds into secondary and higher order structures that are critical for carrying out their functions. These structures can reduce the accessibility of component sequences towards oligonucleotide binding. Additionally, three-dimensional structural motifs represent an additional avenue for therapeutic recognition beyond the linear primary sequence. Detailed knowledge of RNA structure is consequently critical for developing RNA-directed inhibitors of HIV-1.

1.4 SHAPE-directed RNA secondary structure prediction

1.4.1 The RNA secondary structure prediction problem

Determining the complete three-dimensional (termed the tertiary) structure is the ultimate goal for many RNAs. However, only limited sets of RNAs are candidates for current high-resolution crystallography and NMR approaches. A simpler problem is to determine the base-pairing pattern (termed the secondary structure) of an RNA. Secondary structure determination, independent of higher order structural information, is possible because the hydrogen bonding and stacking interactions that collectively form secondary structure are usually stronger than tertiary interactions (1-4), and because RNA folding is often hierarchical (5,6), with many secondary structural motifs forming prior to tertiary contacts. Additionally, knowledge of the secondary

structure greatly restricts possible three-dimensional conformations and facilitates tertiary structure prediction (7-9). Moreover, a subset of RNA functions may depend more directly on secondary structural motifs than on global folds.

Insight into the secondary structure can be gleaned using computer-based predictions performed using the sequence alone, or in combination with sequence alignment information or experimental data. Sequence-based folding generally includes two main elements: an energy function based on experimentally derived thermodynamic parameters, and an algorithm that explores the conformational space available to the RNA and ranks computed structures. Most energy functions use the Turner *et al.* (10,11) set of nearest neighbor parameters, derived from optical melting experiments. A summary of these parameters is available at the Nearest-Neighbor Database (12). Exploring conformational space is challenging because of the vast number of possible secondary structures, which is estimated to scale exponentially as $\sim 1.8^N$, where N is the number of nucleotides in the RNA (13). This means that a "brute force" approach that samples every possible conformation is impossible both from a computational standpoint and from the perspective of efficient RNA folding *in vivo*. Consequently, the intrinsic thermodynamics and kinetics of RNA folding must conspire to restrict the folding pathway to a narrow subset of these structures, only one (or perhaps a few) of which is likely to dominate the equilibrium ensemble. Especially for short RNAs, thermodynamic considerations are likely paramount and thus the structure with the lowest free energy is the biologically active one.

1.4.2 Dynamic programming algorithms for RNA secondary structure prediction

Programs based on the Zuker dynamic programming algorithm (14,15) are

widely used to search for the minimum free energy structure (16-22). These algorithms are deterministic, meaning that given a defined set of energy rules, they always find the lowest free energy structure. The Zuker algorithm scales as $O(N^3)$ in time, where N is the number of nucleotides in the sequence. This means that doubling the sequence length requires eight times as much time to predict the structure. Nevertheless, on modern computers, the time to make a prediction is reasonably fast. The guarantee that the optimal structure can be computed and the relative computational efficiency are made possible, first, by incorporating simplifying assumptions into the energy function, and second, by limiting the types of allowed RNA folds.

The total energy is assumed to be a simple sum over all energetic components that characterize local structural elements. Two features primarily contribute to the total energy: negative (favorable) free energies arising from stabilizing base stacking and hydrogen bonding interactions in and adjacent to helices, and positive (unfavorable) free energies arising from the entropic cost of restricting conformational freedom in loops. Helix energy terms are sequence-dependent, reflect the energetic bonus of adding a base pair to a helix, and implicitly include both canonical hydrogen bonding and base stacking. These terms depend solely on interactions involving adjacent base pairs or interactions at the ends of helices. This local interaction model is termed the nearest-neighbor approximation (23).

The dynamic programming algorithm calculates the energy of the lowest free energy structure (but does not compute the complete structure itself) for all possible subsequences of an RNA. This approach is efficient because the solution for each

subsequence is computed from solutions for pre-computed smaller subsequences, allowing the energies for each structural element to be computed only once. The results are stored in triangular $N \times N$ arrays whose elements *i,j* represent the optimal folding energy for an RNA subsequence from nucleotide *i* to nucleotide *j*. The structure for the entire RNA sequence is obtained by tracing a structure through an optimal combination of component subsequences in the array (24).

Thermodynamics-based dynamic programming algorithms have several limitations. First, computing the minimum free energy structure in a relatively efficient $O(N^3)$ manner excludes consideration of non-nested topologies. These include the biologically important case of pseudoknots, in which a loop in one helix forms the stem of another helix. Second, the assumption that the minimum free energy structure is the biologically active one may not always hold for larger RNAs, where folding kinetics may play a prominent role. Third, the biologically relevant ensemble may be dominated by several interconverting states, making a single structural model inadequate. Finally, incomplete thermodynamic rules and the simplifications inherent in the nearest neighbor model introduce uncertainty to the energy calculations.

The net effect of these limitations is that the current best-performing algorithms achieve prediction accuracies of 50-70% (11,25-29). Accuracies tend to be especially poor for larger RNAs. For example, for *Escherichia coli* 16S rRNA, which is probably the most thoroughly studied large RNA, the prediction accuracy based on sequence alone is less than 50% (26,30).

1.4.3 Incorporating experimental data

Significant improvements to RNA secondary structure prediction can be

achieved when computer predictions are constrained by experimental data derived from structure-sensitive enzymatic cleavage and chemical probing reagents (11,31,32). However, the net improvement gained from using traditional reagents is often modest. First, traditional reagents tend to react with only a subset of nucleotides, so the absence of reactivity cannot usually be taken as evidence for likely base pairing. Second, different reagents are required to react with all four RNA nucleotides and some of the more useful reagents, like dimethyl sulfate (DMS), react at different base functional groups depending on the nucleotide. Third, the dynamic range for many reagents is low, making it difficult to distinguish levels of reactivity beyond a qualitative "low," "medium," and "high" scale. Finally, while alternative chemistries such as in-line probing (33) and hydroxyl radical footprinting (34) provide valuable insight into higher order structures and react broadly with all four RNA nucleotides, they less directly report the intrinsic nucleotide flexibilities that largely characterize secondary structure. Thus, it is challenging to create quantitative relationships between reagent reactivity and RNA secondary structure.

1.4.4 Towards accurate SHAPE-directed secondary structure prediction

Our lab has developed the Selective 2′-Hydroxyl Acylation analyzed by Primer Extension (SHAPE) (35,36) chemical probing technology that largely addresses these challenges. SHAPE yields quantitative reactivity information for nearly every nucleotide in an RNA. Advantageously, SHAPE is not limited by RNA size and is remarkably insensitive to solvent accessibility (35,37,38). Additionally, SHAPE can be applied to both *in vitro* transcripts and also to RNAs from native-like cellular and viral environments. Combining SHAPE information with a thermodynamics-based dynamic

programming algorithm, as implemented in RNAstructure (11), results in highly accurate secondary structure models (30). This approach has been benchmarked and shown to yield secondary structures for diverse RNAs, including the *E. coli* 16S rRNA (1542 nucleotides), with >95% accuracy as judged by sensitivity (percentage of known base pairs predicted correctly) and positive predictive value (PPV, percentage of predicted base pairs in the known structure) (30) (Table 1.1). SHAPE has been used to propose experimentally-informed secondary structural models for many RNAs, including an entire HIV-1 genome (38).

SHAPE technology involves covalently modifying RNA in a structure-dependent manner (selective 2′-hydroxyl acylation), followed by detecting the sites of modification by primer extension (original protocols described in (39,40)). The RNA modification involves the nucleophilic attack of the 2′-hydroxyl group of the RNA ribose moiety on an electrophilic SHAPE reagent to form a 2′-*O*-adduct (Fig. 1A) (35). This reaction occurs more readily with conformationally unconstrained or flexible nucleotides such as those in single stranded regions, loops, or bulges (spheres, Fig. 1B). Flexible nucleotides react preferentially because they more readily sample conformations conducive to nucleophilic attack. In contrast, nucleotides in highly structured regions are conformationally constrained and less frequently achieve an optimal geometry, making them less reactive towards SHAPE reagents. In general, solvent inaccessible, but unconstrained, nucleotides are still reactive by SHAPE.

Following modification of the RNA, modified positions are detected by primer extension using end-labeled, target-specific primers and a thermostable reverse transcriptase (Fig. 1C). Since the reverse transcriptase enzyme cannot proceed past 2′-

O-modified sites in RNA, the lengths of the resulting cDNA products correspond to the distance between the primer binding and 2′-*O*-adduct sites. Due to differential modification of structured versus unstructured nucleotides, the frequency of producing a given cDNA product reflects the underlying RNA structure. Comparison with dideoxy nucleotide sequencing ladders allows each SHAPE reagent-dependent peak to be matched with the corresponding nucleotide position (Fig. 1D).

SHAPE technology can be implemented in an efficient and high-throughput way by automated capillary electrophoresis using DNA sequencing instruments (Fig. 1E). The capillary electrophoresis data are analyzed using the software program QuShape (41) to yield normalized SHAPE reactivity values (Fig. 1F). These reactivities can be converted to $\Delta G_{\mathrm{SHAPE}}$ pseudo-free energy terms and used with the energy function in the RNAstructure program to yield, generally highly accurate, secondary structure models for RNA (Table 1.1) (11,30).

1.4.5 SHAPE experimental procedure

The experimental component of a SHAPE analysis has been recently reviewed in detail (40,42). Briefly, RNA is modified in a structure-selective way using an electrophilic SHAPE reagent. While SHAPE has been most commonly performed on *in vitro* RNA transcripts or RNAs extracted from biological environments, SHAPE reagents readily cross biological membranes and, for example, react with RNAs inside authentic HIV-1 particles (36).

Approximately 2 pmol of RNA is needed in each primer extension reaction to obtain adequate signal intensity in the capillary electrophoresis detection step, using commercially available instruments. We routinely achieve read lengths of 300 – 650

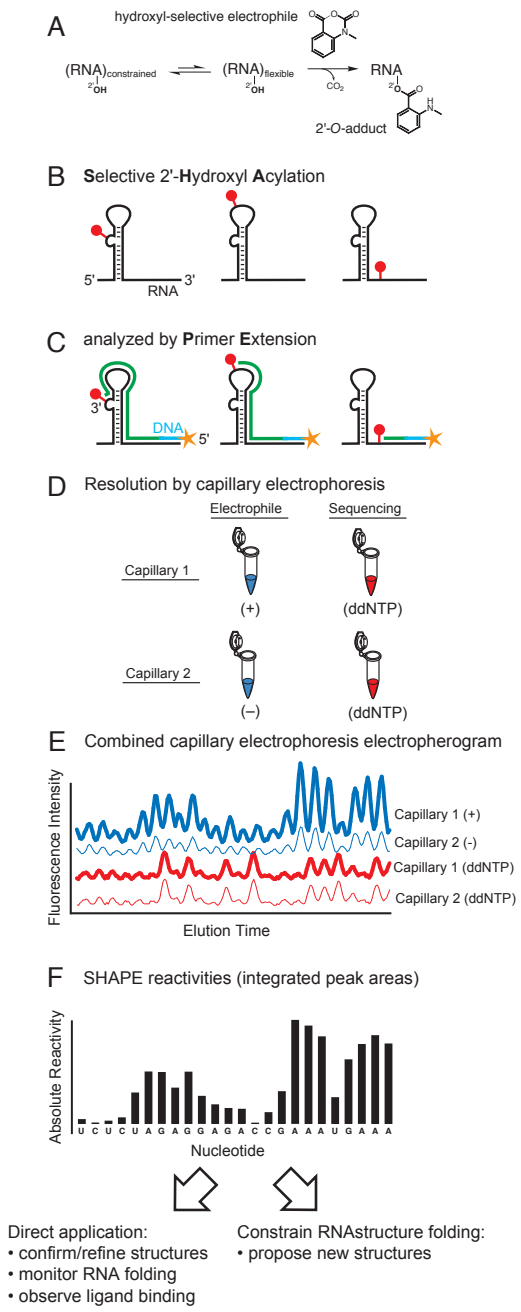

Figure 1.1 Overview of SHAPE experimental and data analysis steps. Adapted from ref. (44)

RNA	Size (nts)	No constraints		With SHAPE	
		Sensitivity	PPV	Sensitivity	PPV
Yeast tRNA ^{Asp}	75	95	95	100	100
HCV IRES domain	95	57	59	96	100
Bacillus subtilis RNase P, specificity domain	154	53	51	75	83
bI3 group I intron, P546 domain	155	43	44	96	98
E. coli 16S rRNA	1542	50	46	97	95

Table 1.1 RNA secondary structure prediction accuracies for folding calculations performed without and with SHAPE constraints.

nucleotides in each primer extension reaction (43,44). For longer RNAs, information obtained from multiple primers, with overlapping read windows, can be combined to create datasets spanning arbitrarily long lengths (30,36,38).

To maintain a native-like conformation, the RNA must be renatured (*in vitro* transcripts) or maintained (RNAs from cellular or viral sources) in a physiological-like folding buffer. We typically use a simple standard solution (50 mM HEPES (pH 8.0), 200 mM potassium acetate (pH 8.0), 3 mM $MgCl_2$), and incubate at 37 °C for 10 – 30 min prior to modification. SHAPE works well under a wide variety of conditions, including in the presence of biological amines and carbohydrates and proteins that bind RNA. The main requirement for SHAPE is that the pH be maintained in the 7.6 – 8.3 range (35).

RNA structure is interrogated by adding a SHAPE reagent. Initial work in our laboratory used the commercially available NMIA reagent (39); more recent work has utilized the faster-reacting 1M7 reagent, whose synthesis is described in (45). A variety of other reagents with subtly different reactivity preferences have also been developed to identify nucleotides engage in slower (46) or faster (47) conformational dynamics. Additionally, a SHAPE reagent that reacts preferentially with nucleotides that present an unoccupied nucleobase for π-π stacking is also under development (48). The SHAPE reagent is dissolved in DMSO and added to the RNA solution to a final concentration of about 5 mM. The optimal reagent concentration varies and can be system-specific: too high a concentration of SHAPE reagent results in significant signal decay and reduced read lengths, while too low a concentration yields data with a poor signal. Background signals in the primer extension reaction are measured by performing a no-reagent

control in which DMSO is added in place of the SHAPE reagent, in an otherwise identical reaction. Both reactions should be incubated at 37 °C for either 35 min if using NMIA or 70 sec if using 1M7. Both reagents self-quench by reacting with water in the aqueous solution.

Following an ethanol precipitation step, fluorescently-labeled primers are annealed to the (+) and (–) reagent-treated RNA and to untreated RNAs or DNA plasmids (the latter are used for sequencing). A thermostable reverse transcriptase enzyme is used for the primer extension reactions to convert the structural information into cDNA libraries. We perform the separation step in two capillaries: the (+) reagent reaction and one sequencing ladder in one capillary and the (–) reagent reaction and an identical sequencing ladder in a second capillary (41). Since each capillary contains two cDNA libraries (one (+) or (-) reagent library and one sequencing ladder), we use two fluorescent dyes, chosen to have similar electrophoretic mobilities to simplify the alignment of the electropherograms during the data processing steps. Reagent traces from both capillaries are aligned to each other and to their primary nucleotide sequences using their identical sequencing ladders. The cDNA products are recovered by ethanol precipitation, resuspended in formamide, and resolved on a commercial capillary electrophoresis DNA sequencing instrument. Electrophoresis data are processed using custom software (41) to created SHAPE reactivities that are normalized on a scale where a normalized reactivity of 1.0 is defined as the average intensity of the top 10% most reactive peaks, excluding a few highly reactive nucleotides taken to be outliers. Reactivities typically span a scale from 0 to ~1.5, where 0 indicates no reactivity (and a highly constrained nucleotide) and reactivities

>0.7 typically indicate highly flexible nucleotides.

1.4.6 SHAPE-constrained RNAstructure folding

A major challenging endeavor in RNA biology is to consistently and efficiently develop correct secondary structure models for RNAs of arbitrary length and complexity. The thermodynamics-based computational methods outlined above (Section 1.1) are highly useful for rapid computation of candidate structural models. However, prediction accuracies are inconsistent for many RNAs and tend to be particularly poor for large RNAs. These limitations can be broadly attributed to simplifications inherent in the nearest-neighbor model and incomplete knowledge of RNA energetics. However, for many RNAs, it is possible to obtain robust secondary structure predictions by incorporating SHAPE reactivities into the energy function used in a nearest neighbor dynamic programming algorithm. This approach has been implemented in the RNAstructure program.

The RNAstructure energy function is modified by adding pseudo-free energy change terms derived from SHAPE reactivities. This approach is grounded in the observation that SHAPE reactivities correlate strongly with local nucleotide flexibility (35,37) and, thus, also with the probability that a nucleotide is single stranded. The NMIA and 1M7 SHAPE reagents react with all four RNA nucleotides with limited base-dependent preferences (49). It is therefore possible to create a softer, continuous, and more physically grounded restraint function than is typically used with conventional chemical mapping reagents that exhibit strong idiosyncratic and nucleotide-specific reactivities. In essence, these additional energetic terms provide a knowledge-based correction to the nearest-neighbor energy function.

We derive a pseudo-free energy change term for each base-paired residue *i* from its SHAPE reactivity:

$$\Delta G_{\mathrm{SHAPE}}(i) = m \ln(\text{SHAPE reactivity}(i) + 1) + b \quad (1.1)$$

The empirical parameters *m* and *b* serve to scale the strength of the experimental contribution to the energy function (Fig. 1.2 A). The intercept *b* represents the pseudo-free energy contribution of a base-paired nucleotide whose SHAPE reactivity is zero. The sign of *b* is negative to reflect an energetic bonus for base pairing by constrained nucleotides. In contrast, the slope *m* represents the strength of the energetic penalty assigned for pairing nucleotides with high SHAPE reactivities and consequently has a positive sign.

Optimal values for *m* and *b* were determined by assessing the prediction accuracy for *E. coli* 23S rRNA over a range of slope and intercept values (30). This work identified *m* = 2.6 kcal/mol and *b* = -0.8 kcal/mol as optimal values for folding large ribosomal RNAs and, importantly, also established these values as being located at the center of a "sweet spot" of a broad set of *m* and *b* values that yields accurate SHAPE-directed structure predictions (30) (emphasized in red, Fig. 1.2B). Given the large size (2,904 nts) of the *E. coli* 23S rRNA and the diversity of structural motifs it contains, these parameter values are also likely to work well for other RNAs. We empirically find this to be the case, although slightly different parameter values, still in the sweet spot (Fig. 1.2B), can be chosen heuristically to refine predictions for some RNAs (38). The logarithmic relationship between SHAPE reactivities and the derived $\Delta G_{\mathrm{SHAPE}}$ term has the effect of forgiving differences among the most highly reactive nucleotides. The usefulness of this behavior reflects the observation that highly reactive nucleotides are the most sensitive

A

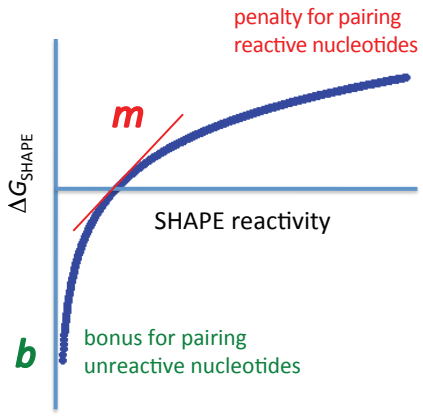

B

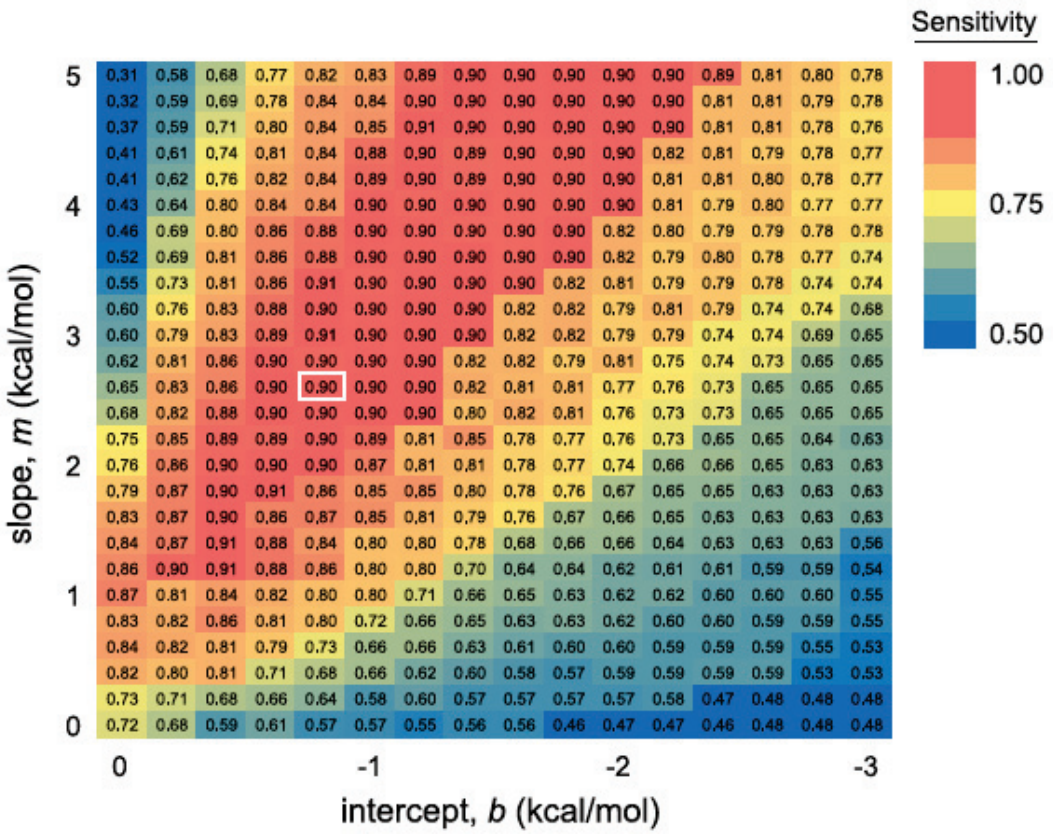

Figure 1.2 (A) SHAPE-derived pseudo-free energy function and (B) base pair prediction sensitivities for *E. coli* 23S rRNA for a range of slope (m) and intercept (b) values (Eqn. (1.1)). Optimal values of m = 2.6 kcal/mol and b = -0.8 kcal/mol are depicted by the white box. Adapted from Ref. (30).

to signal processing artifacts and have the highest variance. Furthermore, the logarithmic relationship between SHAPE reactivity and pseudo-free energy change loosely reflects a statistical mechanical interpretation of SHAPE reactivity, which indirectly measures the number of conformational states accessible to each nucleotide.

We illustrate the combined nearest-neighbor and SHAPE energy function, as implemented in RNAstructure, for a short fragment of an HIV-1 RNA sequence (Fig. 1.3). Nucleotides are color-coded by their SHAPE reactivities as reported in (38). The energy function (12) includes favorable nearest-neighbor energy terms for helix stacking (in green, Fig. 1.3) and entropic penalties for anchoring loops (in red, Fig. 1.3). Stacking terms are added for all helical interactions, including terminal mismatches and dangling ends at helix termini, as well as for coaxial stacking between adjacent helices (25,50). Stacking terms depend on the sequence identity of all nucleotides participating in the stack (the nearest-neighbors), while loop entropy terms depend primarily on the number of nucleotides in the loop.

In contrast to the nearest-neighbor thermodynamics-based energy parameters, pseudo-free energy terms ($\Delta G_{\mathrm{SHAPE}}$) are calculated for each nucleotide individually (Fig. 1.3, black and grey numbers). Nucleotides with high SHAPE reactivities have positive pseudo-free energies and those with low SHAPE reactivities have negative pseudo-free energies (Eqn. 1.1). $\Delta G_{\mathrm{SHAPE}}$ terms are only added to the free energy calculation for base paired nucleotides (Fig. 1.3, black numbers). $\Delta G_{\mathrm{SHAPE}}$ terms for nucleotides at the ends of helices are counted once and those in the interior of helices are counted twice since they contribute to two stacks (Fig. 1.3, blue ×1 and ×2 symbols, respectively). Base paired nucleotides with high SHAPE reactivities contribute large

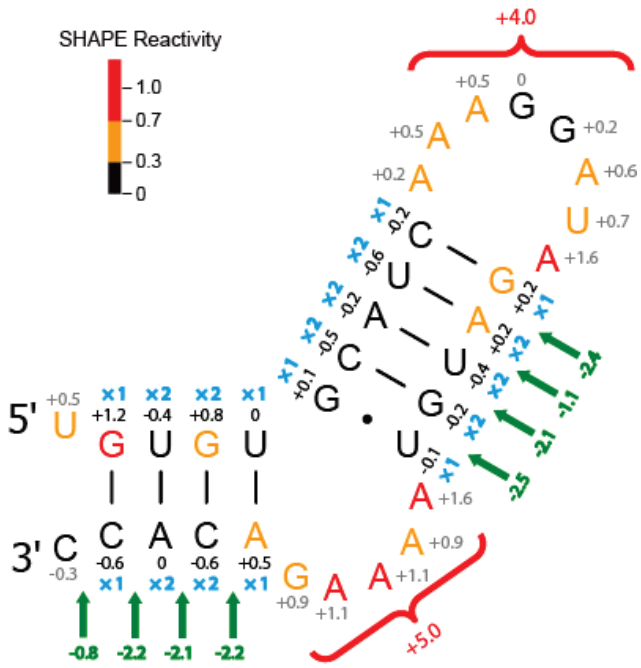

$$\Delta G_{NN} = \sum \Delta G_{stacks} + \sum \Delta G_{loops}$$

$$\Delta G_{SHAPE} = 1 \times \sum \Delta G_{ends} + 2 \times \sum \Delta G_{interior}$$

$$\Delta G_{total} = \Delta G_{NN} + \Delta G_{SHAPE}$$

Figure 1.3 Summary of thermodynamic and SHAPE-derived free energy change contributions for a simple HIV-1 hairpin (NL4-3 nucleotides 594–626) (38). Favorable nearest-neighbor stacking and unfavorable loop thermodynamic terms are shown in green and red, respectively. The total nearest-neighbor free energy change ΔG_{NN} is the sum over all these contributions. ΔG_{SHAPE} pseudo-free energy change terms are shown for base-paired (black) and non-base-paired (grey) nucleotides; only base-paired values are included in the net free energy change. The ΔG_{SHAPE} term is added once for each nucleotide at the ends of helices and twice for interior nucleotides (blue symbols). The ΔG_{SHAPE} calculations used m = 3.0 kcal/mol and b = -0.6 kcal/mol. The total folding free energy change, ΔG_{total}, is the sum of nearest-neighbor and SHAPE-derived contributions.

positive pseudo-free energies (for example, see the red G in Fig. 1.3). Such nucleotides are more likely to be allowed at the end, as opposed to the interior, of a helix because they are added to the total free energy only once. This is consistent with the observation that nucleotides at the ends of helices are more dynamic, and experience greater fraying, than interior nucleotides. On the other hand, unpaired nucleotides with low SHAPE reactivities represent an incomplete model and could suggest non-canonical interactions that are not currently predicted by the algorithm (for example, see the tandem black G residues in the apical loop of Fig. 1.3). The total folding energy (ΔG_{total}) is simply the sum of all nearest neighbor thermodynamic terms (ΔG_{NN}) and pseudo-free energy (ΔG_{SHAPE}) contributions (Fig. 1.3). This sum is used to rank RNA structures and should not be interpreted as a physical energy because it includes both thermodynamic terms and SHAPE-derived pseudo-free energy change terms.

1.4.7 Secondary structure model of an entire HIV-1 genome

This SHAPE-directed RNAstructure folding approach was used to create a nucleotide-resolution secondary structure model of an entire HIV-1 genome (38). Structural models proposed by this work largely agreed with prior studies of important regulatory motifs. However, SHAPE-directed modeling suggested an alternative model for an important regulatory domain, the Gag-Pol frameshift element. Additionally, prior studies collectively span only about 15% of the HIV-1 genome, and the SHAPE-directed model revealed many more structured elements in regions that had not been investigated in prior work.

1.5 Research overview

1.5.1 Structure of the HIV-1 frameshift domain

In Chapter 2, we consider the structure of the Gag-Pol frameshift domain, given both its functional importance for viral replication and the disagreement between the SHAPE-directed and conventionally accepted models. This important regulatory element uses a highly structured motif to regulate translation of all viral-encoded enzymes and is therefore a promising potential therapeutic target in the HIV-1 RNA genome. Using high-affinity locked nucleic acid oligonucleotides to disrupt three helices unique to this new model, we obtain strong support for the SHAPE-directed frameshift domain. We also use SHAPE to examine the thermodynamic stability of helices in the frameshift domain by probing HIV-1 RNA in the presence of the denaturant formamide. We discover that the frameshift domain is anchored by two very stable helices, and that less stable helices within the domain have the propensity to both unfold and switch from the SHAPE-directed to the conventional conformation. We hypothesize that this conformational switch occurs during the frameshifting process, raising the possibility of a functional role for both the SHAPE-directed and conventional models. We furthermore find that formation of the SHAPE-directed model is dependent upon the presence of the complete 140-nucleotide domain, underscoring the importance of global sequence context for RNA folding.

1.5.2 Structure-based design of shRNA inhibitors of HIV-1

In Chapter 3, we use whole-genome SHAPE information to investigate the structural basis for targeting HIV-1 RNA via the RNA interference pathway. The cellular

RNA interference (RNAi) pathway can be exploited using short hairpin RNAs (shRNAs) to durably inactivate pathogenic genes. Prediction of optimal target sites is notoriously inaccurate and current approaches applied to HIV-1 show weak correlations with virus inhibition. In contrast, when using the SHAPE-directed model of an entire HIV-1 genome, we discovered strong correlations between inhibition of HIV-1 production in a quantitative cell-based assay and very simple thermodynamic features in the target RNA. Strongest inhibition occurs at RNA target sites that both have an accessible "seed region" and, unexpectedly, are structurally accessible in a newly identified downstream flanking sequence. We then used these simple rules to create a new set of shRNAs and achieved inhibition of HIV-1 production of 90% or greater for up to 82% of designed shRNAs. These shRNAs inhibit HIV-1 replication in therapy-relevant T-cells and show no or low cytotoxicity. The remarkable success of this straightforward SHAPE-based approach emphasizes that RNAi is governed, in significant part, by very simple, predictable rules reflecting the underlying RNA structure and illustrates principles likely to prove broadly useful in understanding transcriptome-scale biological recognition and therapeutics involving RNA.

1.6 Acknowledgements

Work described in this chapter was supported by National Institutes of Health grant AI068462 (to K.M.W.), National Research Service Award F30DA027364 (to J.T.L.), and Medical Scientist Training Program T32GM008719. Work in our laboratory on experimentally-directed RNA secondary structure prediction benefits from a close and lively collaboration with David Mathews (University of Rochester). We thank David Mauger and David Mathews for critically reviewing this manuscript.

1.7 References

1. Crothers, D.M., Cole, P.E., Hilbers, C.W. and Shulman, R.G. (1974) The molecular mechanism of thermal unfolding of Escherichia coli formylmethionine transfer RNA. *J Mol Biol*, **87**, 63-88.

2. Banerjee, A.R., Jaeger, J.A. and Turner, D.H. (1993) Thermal unfolding of a group I ribozyme: the low-temperature transition is primarily disruption of tertiary structure. *Biochemistry*, **32**, 153-163.

3. Mathews, D.H., Banerjee, A.R., Luan, D.D., Eickbush, T.H. and Turner, D.H. (1997) Secondary structure model of the RNA recognized by the reverse transcriptase from the R2 retrotransposable element. *RNA*, **3**, 1-16.

4. Onoa, B., Dumont, S., Liphardt, J., Smith, S.B., Tinoco, I., Jr. and Bustamante, C. (2003) Identifying kinetic barriers to mechanical unfolding of the T. thermophila ribozyme. *Science*, **299**, 1892-1895.

5. Tinoco, I., Jr. and Bustamante, C. (1999) How RNA folds. *J Mol Biol*, **293**, 271-281.

6. Greenleaf, W.J., Frieda, K.L., Foster, D.A., Woodside, M.T. and Block, S.M. (2008) Direct observation of hierarchical folding in single riboswitch aptamers. *Science*, **319**, 630-633.

7. Holbrook, S.R. (2008) Structural principles from large RNAs. *Annu Rev Biophys*, **37**, 445-464.

8. Bailor, M.H., Sun, X. and Al-Hashimi, H.M. (2010) Topology links RNA secondary structure with global conformation, dynamics, and adaptation. *Science*, **327**, 202-206.

9. Hajdin, C.E., Ding, F., Dokholyan, N.V. and Weeks, K.M. (2010) On the significance of an RNA tertiary structure prediction. *RNA,* **16**, 1340-1349.

10. Xia, T., SantaLucia, J., Jr., Burkard, M.E., Kierzek, R., Schroeder, S.J., Jiao, X., Cox, C. and Turner, D.H. (1998) Thermodynamic parameters for an expanded nearest-neighbor model for formation of RNA duplexes with Watson-Crick base pairs. *Biochemistry*, **37**, 14719-14735.

11. Mathews, D.H., Disney, M.D., Childs, J.L., Schroeder, S.J., Zuker, M. and Turner, D.H. (2004) Incorporating chemical modification constraints into a dynamic programming algorithm for prediction of RNA secondary structure. *Proc Natl Acad Sci U S A*, **101**, 7287-7292.

12. Turner, D.H. and Mathews, D.H. (2010) NNDB: the nearest neighbor parameter database for predicting stability of nucleic acid secondary structure. *Nucleic Acids Res*, **38**, D280-282.

13. Zuker, M., and Sankoff, D. (1984) RNA secondary structures and their prediction. *Bull. Math. Biol.*, **46**, 591-621.

14. Zuker, M. and Stiegler, P. (1981) Optimal computer folding of large RNA sequences using thermodynamics and auxiliary information. *Nucleic Acids Res*, **9**, 133-148.

15. Zuker, M. (1989) On finding all suboptimal foldings of an RNA molecule. *Science*, **244**, 48-52.

16. Durbin, R., Eddy, S.R., Krogh, A. and Mitchison, G. (1998) *Biological sequence analysis : probabilistic models of proteins and nucleic acids*. Cambridge University Press, Cambridge.

17. Mathews, D.H. and Zuker, M. (2005) In Baxevanis, A. D. and Ouellette, B. F. F. (eds.), *Bioinformatics : a practical guide to the analysis of genes and proteins*. 3rd ed. Wiley, Hoboken, N.J., pp. 143 - 170.

18. Mathews, D.H., Schroeder, S.J., Turner, D.H. and Zuker, M. (2006) In Gesteland, R. F., Cech, T. and Atkins, J. F. (eds.), *The RNA world : the nature of modern RNA suggests a prebiotic RNA world*. 3rd ed. Cold Spring Harbor Laboratory Press, Cold Spring Harbor, N.Y., pp. 631 - 657.

19. Mathews, D.H. and Turner, D.H. (2006) Prediction of RNA secondary structure by free energy minimization. *Curr Opin Struct Biol*, **16**, 270-278.

20. Reeder, J., Hochsmann, M., Rehmsmeier, M., Voss, B. and Giegerich, R. (2006) Beyond Mfold: recent advances in RNA bioinformatics. *J Biotechnol*, **124**, 41-55.

21. Shapiro, B.A., Yingling, Y.G., Kasprzak, W. and Bindewald, E. (2007) Bridging the gap in RNA structure prediction. *Curr Opin Struct Biol*, **17**, 157-165.

22. Schroeder, S.J. (2009) Advances in RNA structure prediction from sequence: new tools for generating hypotheses about viral RNA structure-function relationships. *J Virol*, **83**, 6326-6334.

23. Turner, D.H. (1996) Thermodynamics of base pairing. *Curr Opin Struct Biol*, **6**, 299-304.

24. Eddy, S.R. (2004) How do RNA folding algorithms work? *Nat Biotechnol*, **22**, 1457-1458.

25. Mathews, D.H., Sabina, J., Zuker, M. and Turner, D.H. (1999) Expanded sequence dependence of thermodynamic parameters improves prediction of RNA secondary structure. *J Mol Biol*, **288**, 911-940.

26. Doshi, K.J., Cannone, J.J., Cobaugh, C.W. and Gutell, R.R. (2004) Evaluation of the suitability of free-energy minimization using nearest-neighbor energy parameters for RNA secondary structure prediction. *BMC Bioinformatics*, **5**, 105.

27. Dowell, R.D. and Eddy, S.R. (2004) Evaluation of several lightweight stochastic context-free grammars for RNA secondary structure prediction. *BMC Bioinformatics*, **5**, 71.

28. Dima, R.I., Hyeon, C. and Thirumalai, D. (2005) Extracting stacking interaction parameters for RNA from the data set of native structures. *J Mol Biol*, **347**, 53-69.

29. Do, C.B., Woods, D.A. and Batzoglou, S. (2006) CONTRAfold: RNA secondary structure prediction without physics-based models. *Bioinformatics*, **22**, e90-98.

30. Deigan, K.E., Li, T.W., Mathews, D.H. and Weeks, K.M. (2009) Accurate SHAPE-directed RNA structure determination. *Proc Natl Acad Sci U S A*, **106**, 97-102.

31. Ehresmann, C., Baudin, F., Mougel, M., Romby, P., Ebel, J.P. and Ehresmann, B. (1987) Probing the structure of RNAs in solution. *Nucleic Acids Res*, **15**, 9109-9128.

32. Knapp, G. (1989) Enzymatic approaches to probing of RNA secondary and tertiary structure. *Methods Enzymol*, **180**, 192-212.

33. Regulski, E.E. and Breaker, R.R. (2008) In-line probing analysis of riboswitches. *Methods Mol Biol*, **419**, 53-67.

34. Tullius, T.D. and Greenbaum, J.A. (2005) Mapping nucleic acid structure by hydroxyl radical cleavage. *Curr Opin Chem Biol*, **9**, 127-134.

35. Merino, E.J., Wilkinson, K.A., Coughlan, J.L. and Weeks, K.M. (2005) RNA structure analysis at single nucleotide resolution by selective 2'-hydroxyl acylation and primer extension (SHAPE). *J Am Chem Soc*, **127**, 4223-4231.

36. Wilkinson, K.A., Gorelick, R.J., Vasa, S.M., Guex, N., Rein, A., Mathews, D.H., Giddings, M.C. and Weeks, K.M. (2008) High-throughput SHAPE analysis reveals structures in HIV-1 genomic RNA strongly conserved across distinct biological states. *PLoS Biol*, **6**, e96.

37. Gherghe, C.M., Shajani, Z., Wilkinson, K.A., Varani, G. and Weeks, K.M. (2008) Strong correlation between SHAPE chemistry and the generalized NMR order parameter (S2) in RNA. *J Am Chem Soc*, **130**, 12244-12245.

38. Watts, J.M., Dang, K.K., Gorelick, R.J., Leonard, C.W., Bess, J.W., Jr., Swanstrom, R., Burch, C.L. and Weeks, K.M. (2009) Architecture and secondary structure of an entire HIV-1 RNA genome. *Nature*, **460**, 711-716.

39. Wilkinson, K.A., Merino, E.J. and Weeks, K.M. (2006) Selective 2'-hydroxyl acylation analyzed by primer extension (SHAPE): quantitative RNA structure analysis at single nucleotide resolution. *Nat Protoc*, **1**, 1610-1616.

40. McGinnis, J.L., Duncan, C.D.S. and Weeks, K.M. (2009) High-Throughput Shape and Hydroxyl Radical Analysis of RNA Structure and Ribonucleoprotein Assembly. *Methods Enzymol*, **468**, 67-89.

41. Karabiber, F., McGinnis, J.L., Favorov, O.V. and Weeks, K.M. (submitted) QuShape: Rapid, Accurate and Best-Practices Quantification of Nucleic Acid Probing Information, Resolved by Capillary Electrophoresis.

42. Mortimer, S.A. and Weeks, K.M. (2009) Time-resolved RNA SHAPE chemistry: quantitative RNA structure analysis in one-second snapshots and at single-nucleotide resolution. *Nat Protoc*, **4**, 1413-1421.

43. Duncan, C.D. and Weeks, K.M. (2008) SHAPE analysis of long-range interactions reveals extensive and thermodynamically preferred misfolding in a fragile group I intron RNA. *Biochemistry*, **47**, 8504-8513.

44. Vasa, S.M., Guex, N., Wilkinson, K.A., Weeks, K.M. and Giddings, M.C. (2008) ShapeFinder: a software system for high-throughput quantitative analysis of nucleic acid reactivity information resolved by capillary electrophoresis. *RNA*, **14**, 1979-1990.

45. Mortimer, S.A. and Weeks, K.M. (2007) A fast-acting reagent for accurate analysis of RNA secondary and tertiary structure by SHAPE chemistry. *J Am Chem Soc*, **129**, 4144-4145.

46. Gherghe, C.M., Mortimer, S.A., Krahn, J.M., Thompson, N.L. and Weeks, K.M. (2008) Slow conformational dynamics at C2'-endo nucleotides in RNA. *J Am Chem Soc*, **130**, 8884-8885.

47. Mortimer, S.A. and Weeks, K.M. (2008) Time-resolved RNA SHAPE chemistry. *J Am Chem Soc*, **130**, 16178-16180.

48. Steen, K.-A., Rice, G.M. and Weeks, K.M. (2012) Fingerprinting Noncanonical and Tertiary RNA Structures by Differential SHAPE Reactivity. *J Am Chem Soc*, **134**, 13160-13163.

49. Wilkinson, K.A., Vasa, S.M., Deigan, K.E., Mortimer, S.A., Giddings, M.C. and Weeks, K.M. (2009) Influence of nucleotide identity on ribose 2'-hydroxyl reactivity in RNA. *RNA*, **15**, 1314-1321.

50. Serra, M.J. and Turner, D.H. (1995) Predicting thermodynamic properties of RNA. *Methods Enzymol*, **259**, 242-261.

CHAPTER 2

STRUCTURE OF THE HIV-1 FRAMESHIFT ELEMENT, INVESTIGATED BY LNA BINDING AND SHAPE PROBING

2.2 Introduction

HIV-1 viral enzymes, including protease, reverse transcriptase, and integrase, are generated by cleavage of the precursor polyprotein Gag-Pol. The *pol* gene cannot be expressed independently as it lacks a translation start site such as a start codon or an internal ribosomal entry site (IRES). Instead, Pol is translated as a fusion product with the Gag polyprotein that lies immediately upstream in the full length HIV-1 mRNA. While these two polyproteins are translated together, the *pol* gene is encoded in a reading frame that is offset from the upstream *gag* reading frame by one nucleotide in the 5′ direction. Consequently, translation of the Gag-Pol fusion protein relies on a process termed programmed ribosomal frameshifting that involves standard translation of the upstream Gag polyprotein followed by a recoding event that shifts the ribosome from the *gag* to the *pol* reading frame (1).

Frameshifting occurs at a specific site at the *gag-pol* junction that requires two key elements: (*i*) a UUUUUUA sequence that is strongly conserved across HIV strains (2) termed the slippery sequence at which the switch in reading frame occurs, and (*ii*) a downstream structural element termed the frameshift stimulatory stem. This downstream structure is thought to function by pausing the ribosome while the A and P

sites are occupied by the slippery sequence. While the precise mechanism remains incompletely understood, this arrangement allows 'slipping' of the ribosome by one nucleotide in the 5′ direction. Frameshifting occurs with a frequency of approximately 5-10% in cultured HIV-transfected human cells and the Gag to Gag-Pol ratio appears to be important for viral fitness (3). The frameshifting process has consequently attracted interest as a target for potential therapeutic development (4,5).

The frameshift stimulatory stem was originally proposed to comprise a single stem-loop (6). However, a number of refinements and extensions of this model have subsequently been proposed, including pseudoknots (7,8), a triplex (9), and a two-helix model (10). NMR studies performed on 41 and 45 nt transcripts have subsequently supported the formation of the two-helix model and this model is therefore now generally accepted as correct (11,12). The two-helix model includes the originally proposed stem, now termed the upper stem, and adds an additional lower stem that is separated from the upper stem by a three-purine bulge (Fig. 2.1). The functional importance of this lower stem is further supported by experiments demonstrating decreased frameshifting when the lower stem is destabilized by mutation (10) or when a truncated construct containing only the classical upper stem is used (13).

An alternative, more complex model was recently suggested based on SHAPE chemical probing experiments performed on an entire HIV-1 genome (14). SHAPE reagents react with RNA in a structure-selective manner. Flexible, single-stranded nucleotides tend to be reactive towards SHAPE reagents, whereas nucleotides in base-paired or otherwise constrained conformations tend to be unreactive. This structure-selective reactivity pattern provides nucleotide-resolution information about RNA

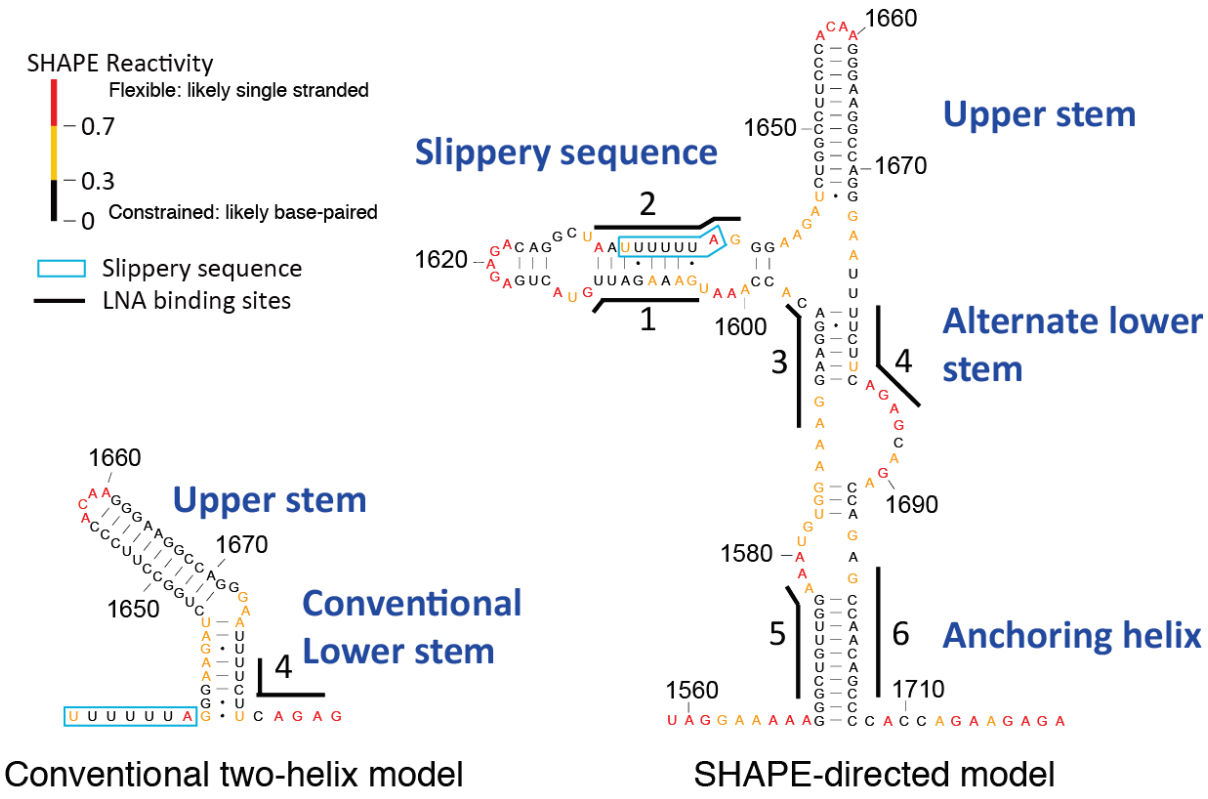

Figure 2.1 Conventional (10) and SHAPE-directed (14) models of the frameshift domain. Nucleotides are colored by *ex virio* SHAPE reactivities and are numbered according to the NL4-3 genome.

secondary structure and is not limited by the size of the RNA under study (15). SHAPE reactivities can be incorporated into the thermodynamics-based computer folding algorithm RNAstructure (16) to obtain highly accurate RNA secondary structure models (17).

The SHAPE-directed model of the frameshift domain includes a total of four main helices (Fig. 2.1). One of these helices is equivalent to the upper stem of the conventional two-helix model. An additional helix involves refolding of the lower stem of the conventional model. We term these alternative base-pairings the alternate lower stem. SHAPE data also support the formation of two additional helices that fall outside the domain traditionally identified as the frameshift element. These include a helix that sequesters most of the slippery sequence in base-pairing interactions, and a 10-nt anchoring helix that completes the 140 nt domain (Fig. 2.1).

Given the critical role RNA structure plays in regulating frameshifting, we sought to confirm the existence of helices proposed by SHAPE and to ask whether the SHAPE-directed model could be reconciled with the conventional two-helix model. Our strategy takes advantage of the high binding affinities of locked nucleic acid (LNA)-containing oligonucleotides to RNA (18,19), in order to selectively bind and thereby disrupt specific helices in the SHAPE-directed frameshift model. We monitored the resulting structural changes by SHAPE. If the targeted helices were present, we expected that binding of LNAs to one strand of the helix would displace nucleotides on the partner strand. Released from their native base-pairing interactions, we anticipated that the resulting SHAPE reactivities of the displaced partner strand would increase.

Throughout this study we used full length genomic RNA extracted from authentic HIV-1 virions, allowing us to probe frameshift domain structures in their complete sequence context. Our results demonstrated SHAPE reactivity changes induced by LNA binding that strongly support the SHAPE-directed frameshift model. Unexpectedly, these experiments also revealed the ability of this domain to adopt the conventional two-helix model upon disruption of specific helices in the domain. Interpreting LNA binding and subsequent disruption as a rough approximation of ribosomal unwinding of the frameshift domain, we speculate that the different structural states induced by helix unwinding could have biological functions during the frameshift process. This interpretation would preserve a role for the conventional two-helix model as the frameshift domain is unwound during translation.

We also investigated the relative stability and conservation of the frameshift domain helices between two distinct biological states by performing SHAPE in the presence of formamide denaturant and in the context of the packaged RNA inside virion particles. We found that the frameshift domain is organized into highly structured, invariant helices with intervening sequences capable of forming varying degrees of structure in different environments. These results provide an experimentally-supported framework for further investigation of the structural dynamics and function of this important regulatory domain.

2.2 Results

2.2.1 Both natively extracted *ex virio* and heat-denatured RNAs adopt similar structures in the frameshift region.

We initially attempted to bind LNAs to sequences in folded full-length genomic RNA extracted from HIV-1 virions. However, addition of LNAs directed against the anchoring helix failed to produce detectable SHAPE reactivity increases at the partner strand. Two possible explanations for this initial result are: (*i*) the preformed, targeted helix was too stable to be disrupted by LNA binding, or (*ii*) inaccuracies in our model meant that the proposed helix was actually not present. To determine if a highly stable helix was the cause, we introduced a heating step where we first heated the HIV-1 RNA at 95˚C for 5 min in the presence of LNA, snap cooled on ice, and incubated in a folding buffer. The goal of this heating step was to denature helices and allow the LNA to out-compete native base pair partners. We found that SHAPE reactivities on the partner strand did increase upon addition of LNA using this procedure. This demonstrates that anchoring helix stability, rather than an incorrect model, was the source of our initial inability to detect SHAPE reactivity changes (Section 2.2.2).

To properly interpret SHAPE reactivity changes following heat denaturation and LNA binding in the frameshift element region we must assume that RNA folding following heat denaturation results in a native-like conformation. To test this assumption, we performed SHAPE on both extracted, natively folded *ex virio* RNA and this same RNA following heat denaturation and refolding. We found that SHAPE reactivities for the genome region near the frameshift element are highly similar in both *ex virio* and refolded RNAs (Fig. 2.2A). A comparison of reactivities from a larger ~700

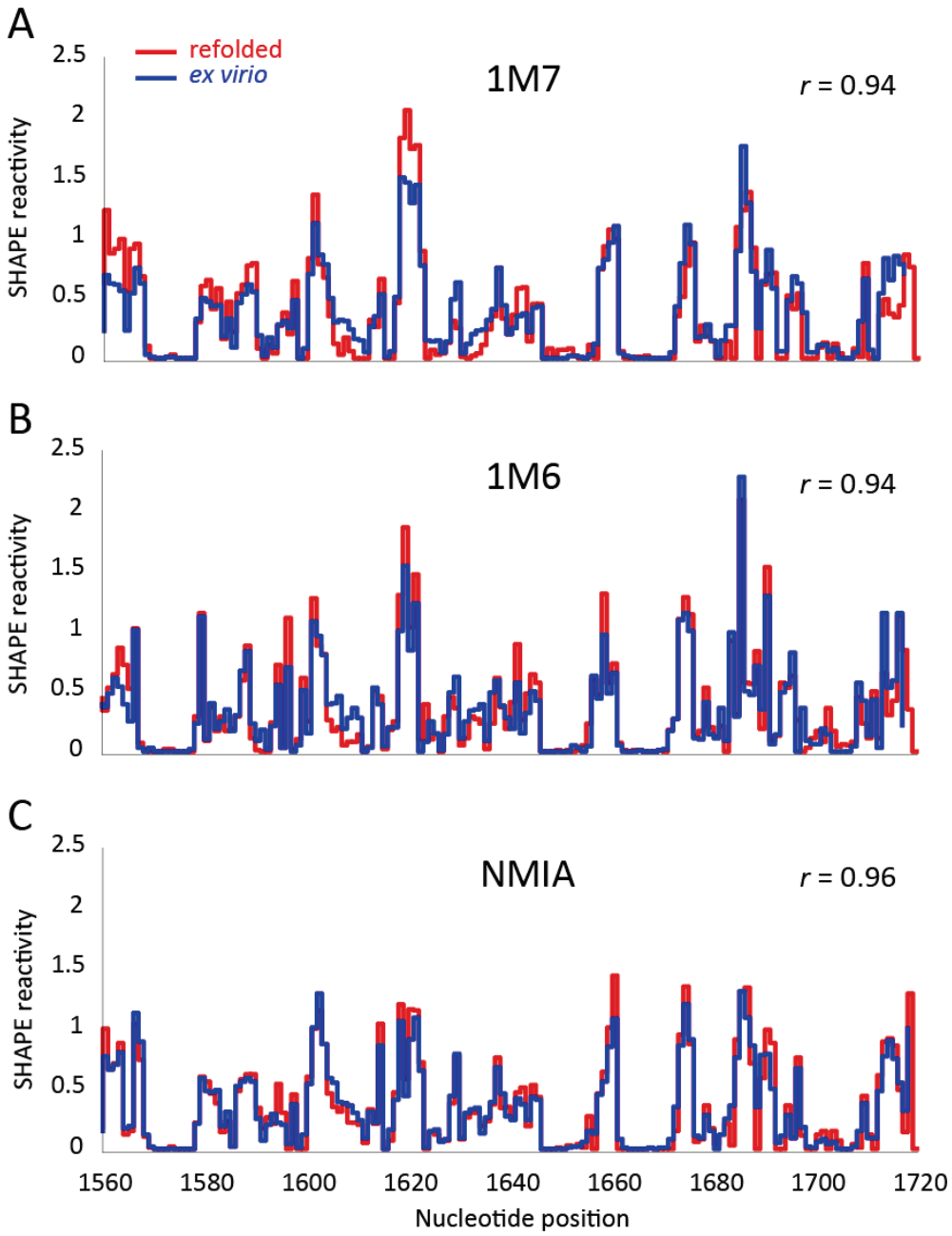

Figure 2.2 Frameshift domain reactivities of extracted *ex virio* RNA and refolded heat denatured RNA using three different SHAPE reagents.

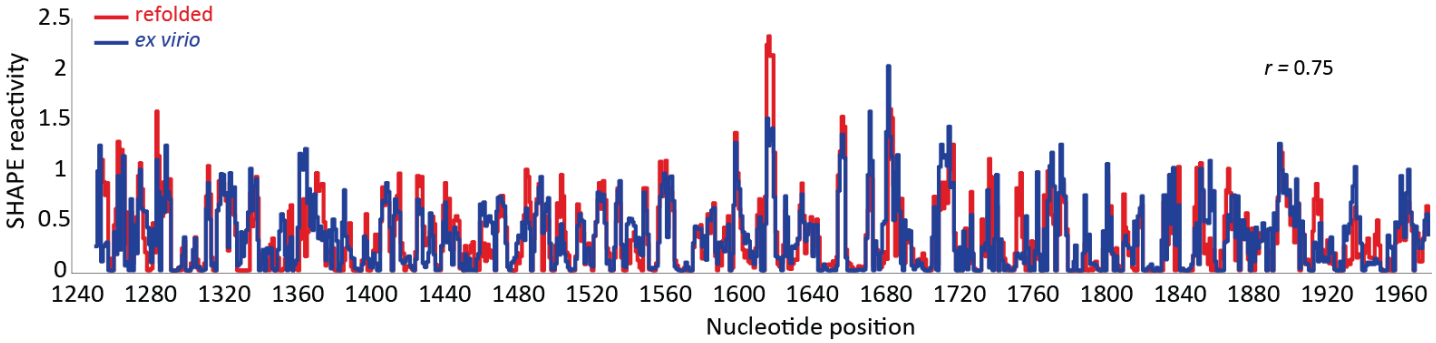

Figure 2.3 Standard SHAPE reactivities (1M7) of extracted *ex virio* RNA and refolded heat denatured RNA for a region spanning ~700 nts surrounding the frameshift domain.

nt region encompassing the frameshift element reveals more significant reactivity differences between *ex virio* and refolded RNA (r = 0.75), but the overall profile is largely the same (Fig. 2.3).

To further probe the differences between *ex virio* and refolded RNA, we performed SHAPE reactions on each RNA state using two alternative SHAPE reagents, 1M6 and NMIA. While these electrophiles are similar to the currently used standard SHAPE reagent 1M7 (20), these reagents exhibit subtle reactivity differences that are sensitive to different local structural states and timescales. In particular, the 1M6 reagent has an enhanced ability to engage in π-π stacking interactions and displays increased reactivity towards nucleotides where one side of the nucleobase stacks with a neighboring nucleotide and the other side is available for stacking with the reagent (21). The NMIA reagent reacts on a slower time scale than 1M6 and 1M7 and can therefore detect nucleotides undergoing slow conformational dynamics (22). These reactivity differences can be used to provide a structural fingerprint of an RNA, and we can compare the two fingerprints to gauge their similarity. Reactivity profiles for all three reagents are similar at the frameshift domain (Fig. 2.2), although at the nucleotide level, some variability is apparent. Pairwise linear correlation coefficients for the 140 nt SHAPE-directed *ex virio* frameshift domain are 0.80 between 1M7 and 1M6, 0.91 between 1M7 and NMIA, and 0.73 between 1M6 and NMIA. In contrast, reactivity profiles between *ex virio* and refolded RNAs for each reagent are much more similar, with linear correlation coefficients of 0.94, 0.94, and 0.96 for 1M7, 1M6, and NMIA, respectively. This high similarity between SHAPE reactivities of *ex virio* and refolded RNA as reported by three different reagents strongly suggests that the structures of

LNA	LNA sequence	Target sequence	Region bound
1	**C**A**ATC**TT**TC**	GAAAGAUUG	1604-1612
2	**CTAAAAAATT**	AAUUUUUUAG	1629-1638
3	**GTCCTTCCT**	AGGAAGGAC	1588-1596
4	**TC**T**G**A**AGA**A	UUCUUCAGA	1678-1686
5	**TCCAACAGC**	GCUGUUGGA	1570-1578
6	**GCTGTTGGC**	GCCAACAGC	1697-1705

Table 2.1 LNA-containing DNA oligonucleotide sequences and target RNA binding sites. LNA nucleotides are underlined.

these two states are extremely similar. We conclude that the refolded frameshift domain adopts essentially the same conformation as the more biologically relevant *ex virio* state. This allows us to use heat denaturation to promote LNA disruption of stable helices while maintaining a native-like fold.

2.2.2 LNA binding experiments support the SHAPE-directed frameshift model

We designed 9- and 10-nt LNA oligonucleotides to bind to and disrupt each of the 3 helices unique to the SHAPE-directed frameshift model (Fig. 2.1 and Table 2.1). We designed one LNA for each helix strand for a total of two LNAs per helix. If the targeted helix existed and if LNA binding was able to out-compete native helical base-pairing, we expected to find increased SHAPE reactivity at the strand complementary to the LNA-bound strand.

The results of the six LNA binding experiments targeting the three helices unique to the SHAPE-directed frameshift model are shown in Fig. 2.4. The partner strand expected to be released from base-pairing by LNA binding is highlighted in grey. In all six cases, SHAPE reactivity increases in at least some nucleotides of the partner strand. These results strongly support the formation of these three helices in the full-length HIV RNA.

2.2.3 LNA binding can switch the SHAPE-directed alternate lower stem to the conventional lower stem.

Although a general increase in reactivity always occurs at the partner strand upon LNA binding, most LNAs also induce additional SHAPE reactivity changes in other regions of the frameshift domain. For example, while LNA 3 is designed to disrupt the

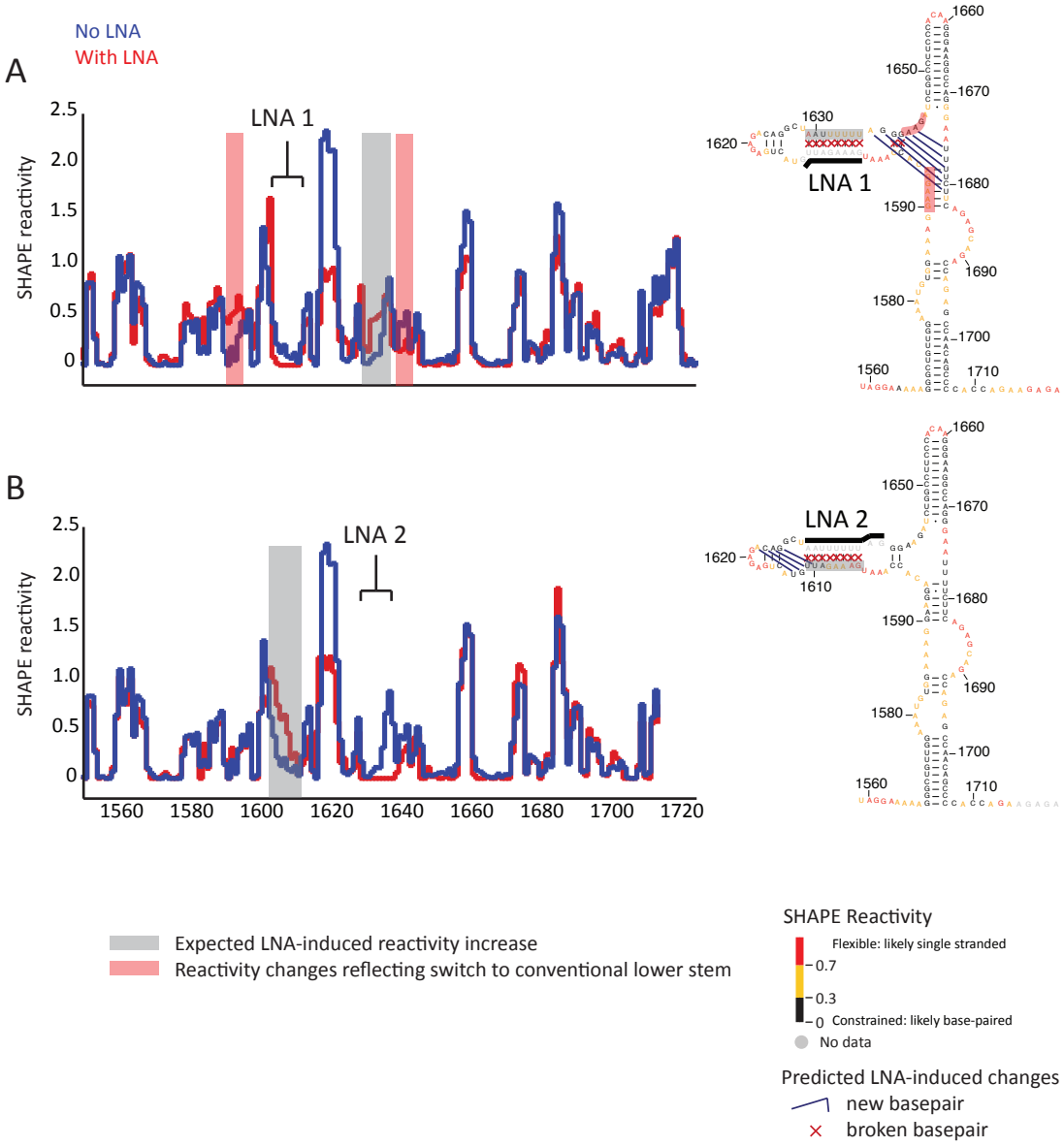

Figure 2.4 (A) and (B) Frameshift region SHAPE reactivities and predicted secondary structure models for HIV-1 RNA bound to LNAs targeting the slippery sequence helix.

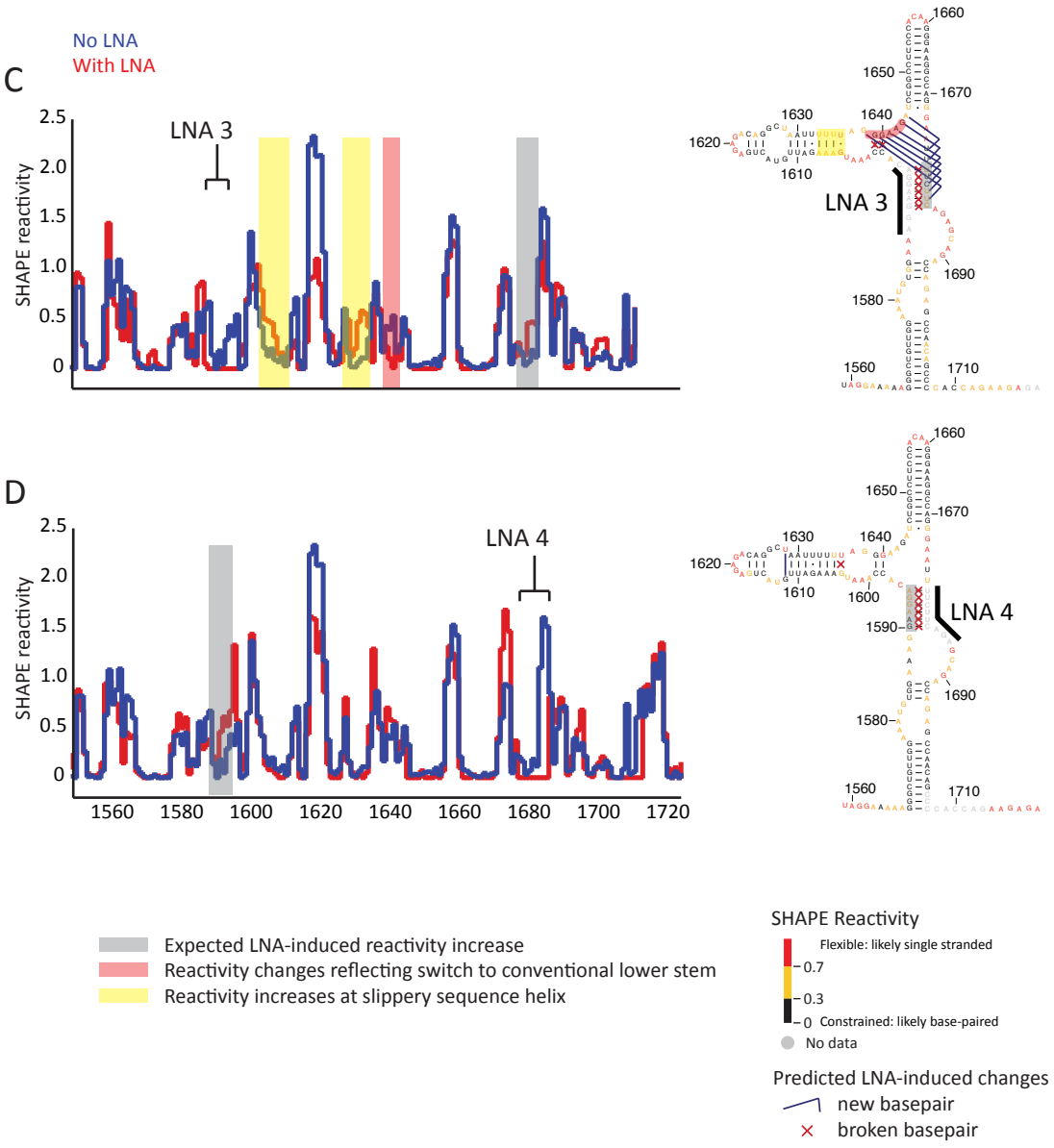

Figure 2.4 (C) and (D) Frameshift region SHAPE reactivities and predicted secondary structure models for HIV-1 RNA bound to LNAs targeting the SHAPE-directed alternate lower stem.

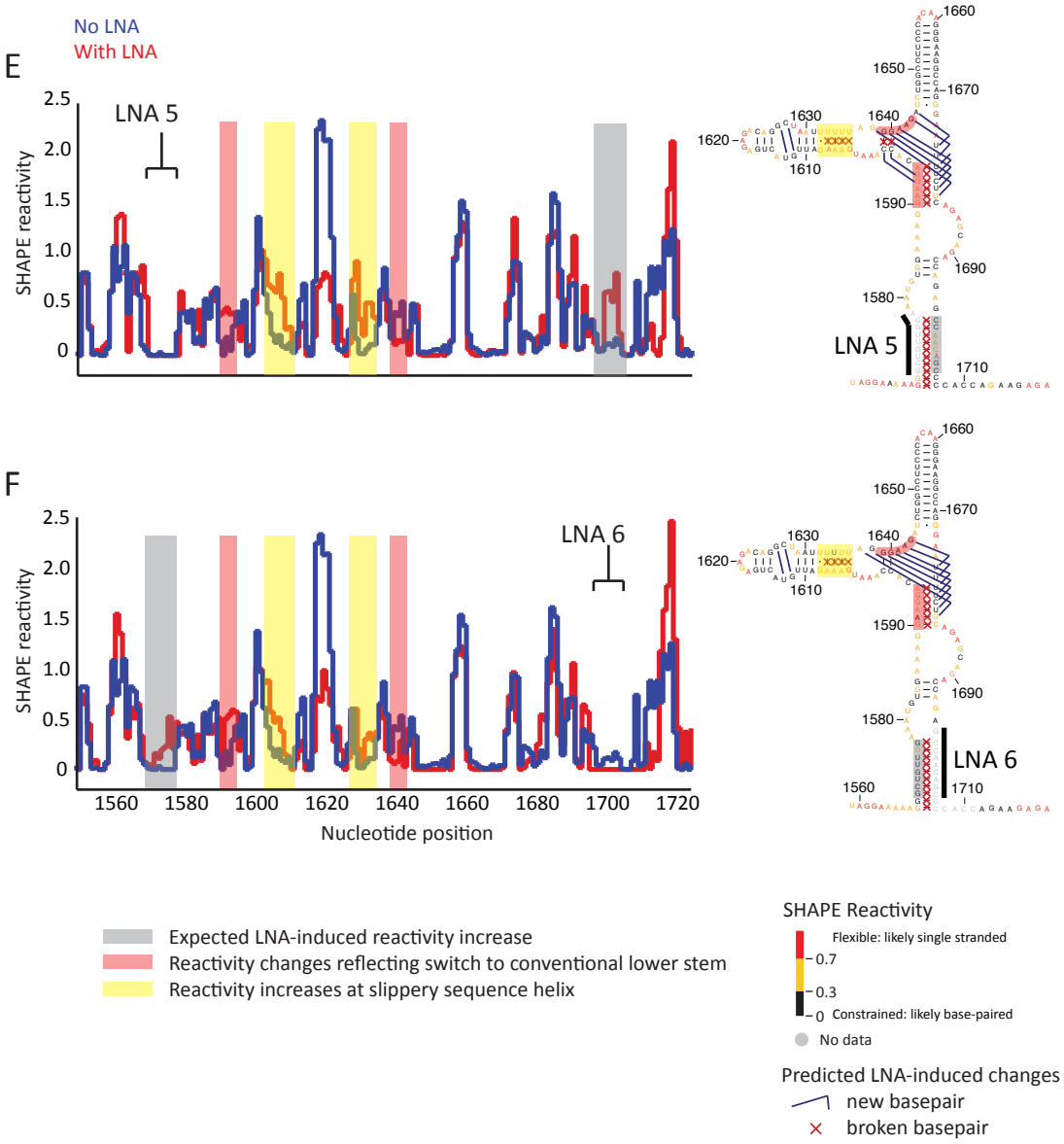

Figure 2.4 (E) and (F) Frameshift region SHAPE reactivities and predicted secondary structure models for HIV-1 RNA bound to LNAs targeting the anchoring helix.

alternate lower stem and causes reactivity increases at the target's partner, these increases are relatively minor and confined to nucleotides 1681-1683 (Fig. 2.4C, grey box). In contrast, more extreme changes in reactivity are present in other regions (Fig. 2.4C, red and yellow boxes). Nucleotides 1641-1643, highlighted in red, exhibit reduced reactivity relative to the no-LNA control. These nucleotides are predicted to be single stranded in the SHAPE-directed frameshift model, and the reduction in SHAPE reactivity upon LNA binding suggests the formation of new base-pairing interactions. Indeed, when the LNA 3-bound SHAPE data are used to direct folding of this domain, these nucleotides are predicted to form novel base-pairing interactions (Fig. 2.4C, purple lines), which largely correspond to the lower stem in the conventional two-helix model. Thus binding of LNA 3 switches the SHAPE-directed alternate lower stem to the conventional lower stem. Formation of this helix furthermore provides an explanation for why SHAPE reactivity increases are noted for only some of the partner nucleotides upon LNA 3 binding: many of these partner nucleotides refold to form part of the conventional lower stem.

Disruption of either strand of the anchoring helix by LNA 5 and LNA 6 results in SHAPE reactivity increases on the corresponding partner strand (Fig. 2.4 E, F). However, additional unexpected changes also occur. These changes closely resemble the changes seen upon LNA 3 binding to the alternate lower stem. SHAPE reactivities decrease for nucleotides 1641-1643 and increase for nucleotides 1590-1595, consistent with a transition from the alternate lower stem to the conventional lower stem. These results suggest that the anchoring helix stabilizes the alternate lower stem.

Disruption of the slippery sequence helix by LNA 1 binding also results in SHAPE reactivity changes that suggest a switch from the alternate to the conventional lower stem (Fig. 2.4A, red boxes). However, binding to the complementary side of the helix by LNA 2 does not result in a switch (Fig. 2.4B). LNA 2 targets nucleotides in close proximity to, and possibly overlapping with, the conventional lower stem. This partial steric occlusion could disfavor formation of the conventional lower stem.

2.2.4 Formation of the conventional lower stem destabilizes the slippery sequence helix.

Binding by LNAs 3, 5 and 6 all result in a switch from the alternate lower stem to the conventional lower stem (Fig. 2.4 C, E, F, red boxes) and may represent an interesting biological function. Binding of these LNAs also result in increased SHAPE reactivity at the slippery sequence helix (Fig. 2.4 C, E, F, yellow boxes). Remarkably, these changes occur upon disruption of the relatively distant anchoring helix by LNAs 5 and 6. In contrast, LNA 4, which destabilizes the alternate lower stem but does not induce formation of the conventional lower stem, does not cause significant SHAPE reactivity changes in the slippery sequence helix (Fig. 2.4D). These results suggest the alternate lower stem and slippery sequence stabilize each other.

2.2.5 Formamide denaturation experiments reveal the relative stabilities of the four frameshift structure helices.

We next examined the relative stabilities of the four main helices present in the SHAPE-directed frameshift element. Our strategy was to incubate HIV-1 RNA in a formamide-containing buffer. Due to the denaturing effects of formamide on nucleic acid (23), we expected to find increased reactivity towards 1M7 as the formamide concentration increased. Less stable helices should denature at lower formamide

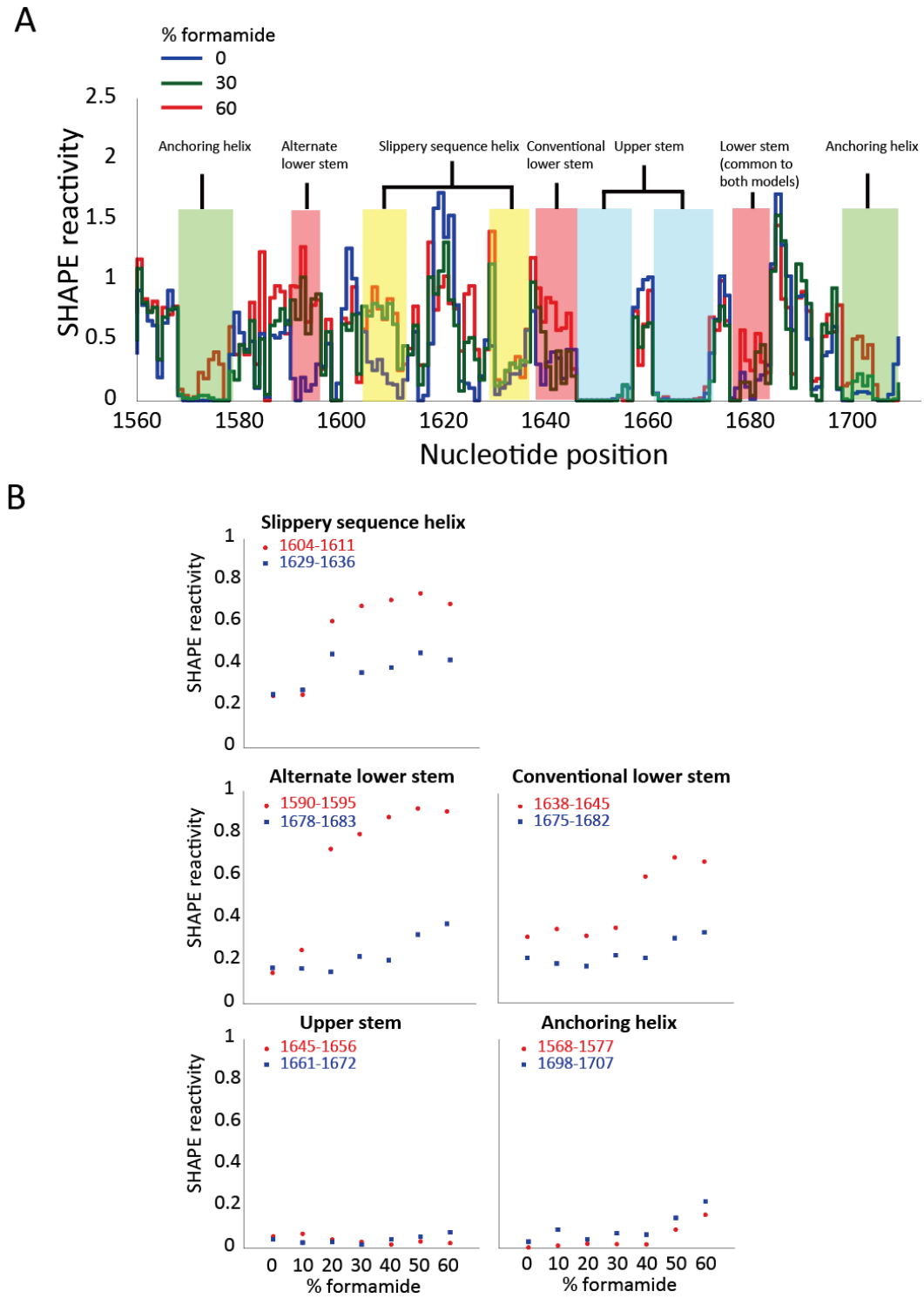

Figure 2.5 (A) SHAPE reactivity profiles for formamide-denatured RNA (red and green) compared with *ex virio* reactivities (blue) and (B) average SHAPE reactivities for each helical strand as a function of formamide concentration. Helices defined by both the SHAPE-directed and conventional models are shown.

concentrations than highly stable helices and this transition from base-paired to single-stranded nucleotides can be detected by SHAPE reactivity.

Following a 20-minute incubation at 37˚C in folding buffer, we added formamide and incubated the solution for a further 20 min before initiating a SHAPE reaction with 1M7. We varied the formamide concentrations from 0% to 60%, in increments of 10%. The resulting SHAPE reactivities show a general increase with formamide concentration, shown in Fig. 2.5A for 0%, 30% and 60% formamide.

Average SHAPE reactivities as a function of formamide concentration are plotted in Fig. 2.5B for all helix strands defined by both the SHAPE-directed and conventional two-helix models. Nucleotides on one side of the slippery sequence helix (1604-1611) have low reactivity in 10% formamide, but show markedly increased reactivity at formamide concentrations of 20% and above. However, only modest reactivity changes are apparent at high formamide concentration on the partner strand (1629-1636) (Fig. 2.5A, yellow). This demonstrates that the slippery sequence helix unfolds at 20% formamide, although one partner strand is able to form stabilizing interactions even in the presence of high denaturant concentration.

Nucleotides 1590-1595 are involved in the alternate lower stem and are unreactive in up to 10% formamide, but are very reactive at 20% formamide and greater. Partner nucleotides 1678-1683, which can pair with either the alternate or conventional lower stem, remain lowly reactive in up to 30% formamide, but then increase modestly in reactivity at higher formamide concentrations. Nucleotides in the conventional lower stem exhibit little change in reactivity in up to 30% formamide but increase after that. These data suggest that the alternate lower stem unfolds in 20%

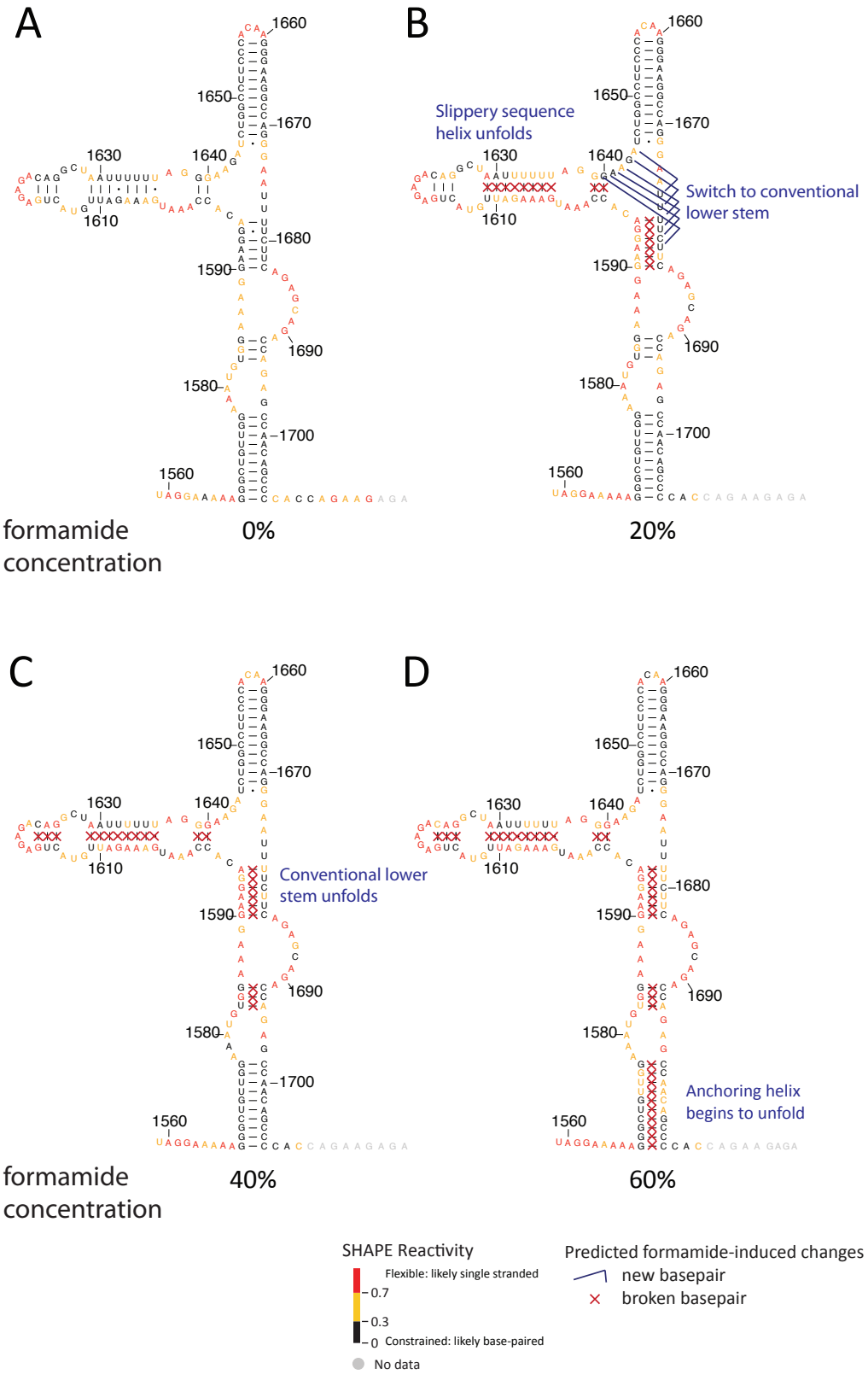

Figure 2.6 Secondary structure models for formamide-denatured RNA.

formamide. At this concentration of denaturant, both its partner nucleotides and nucleotides involved in the conventional lower stem exhibit lower reactivities, and secondary structure modeling of the frameshift domain suggests the formation of the conventional lower stem (Fig. 2.6B). Upon further increases in formamide concentration, the conventional lower stem also unfolds (Fig. 2.6C). Nearest neighbor thermodynamic calculations indicate that the conventional lower stem is slightly more stable than the SHAPE-directed alternate lower stem (-8.4 kcal/mol and -8.2 kcal/mol, respectively). In light of both these results and LNA disruption results, it appears that formation of the alternate lower stem is largely dependent on stabilization from other elements in the domain and that as these interactions are disrupted by formamide, the slightly more stable conventional lower stem is able to form.

The anchoring helix and upper stem show very low SHAPE reactivities up to 40% formamide. Unfolding of the anchoring helix is first apparent in 50% formamide, although the upper stem remains unreactive even in 60% formamide (Fig. 2.6D). This implies that these two helices are highly stable and exist even under denaturing conditions. The high stability of the upper stem has been previously observed (24) and is thought to be attributable both to the high GC content of the helix and the stabilizing atypical ACAA tetraloop that caps the helix. We conclude from these denaturant experiments that the frameshift domain is bounded by two highly stable helices and that the intervening less stable helices have the propensity to both unfold and, in the case of the lower stem, refold into two alternative conformations.

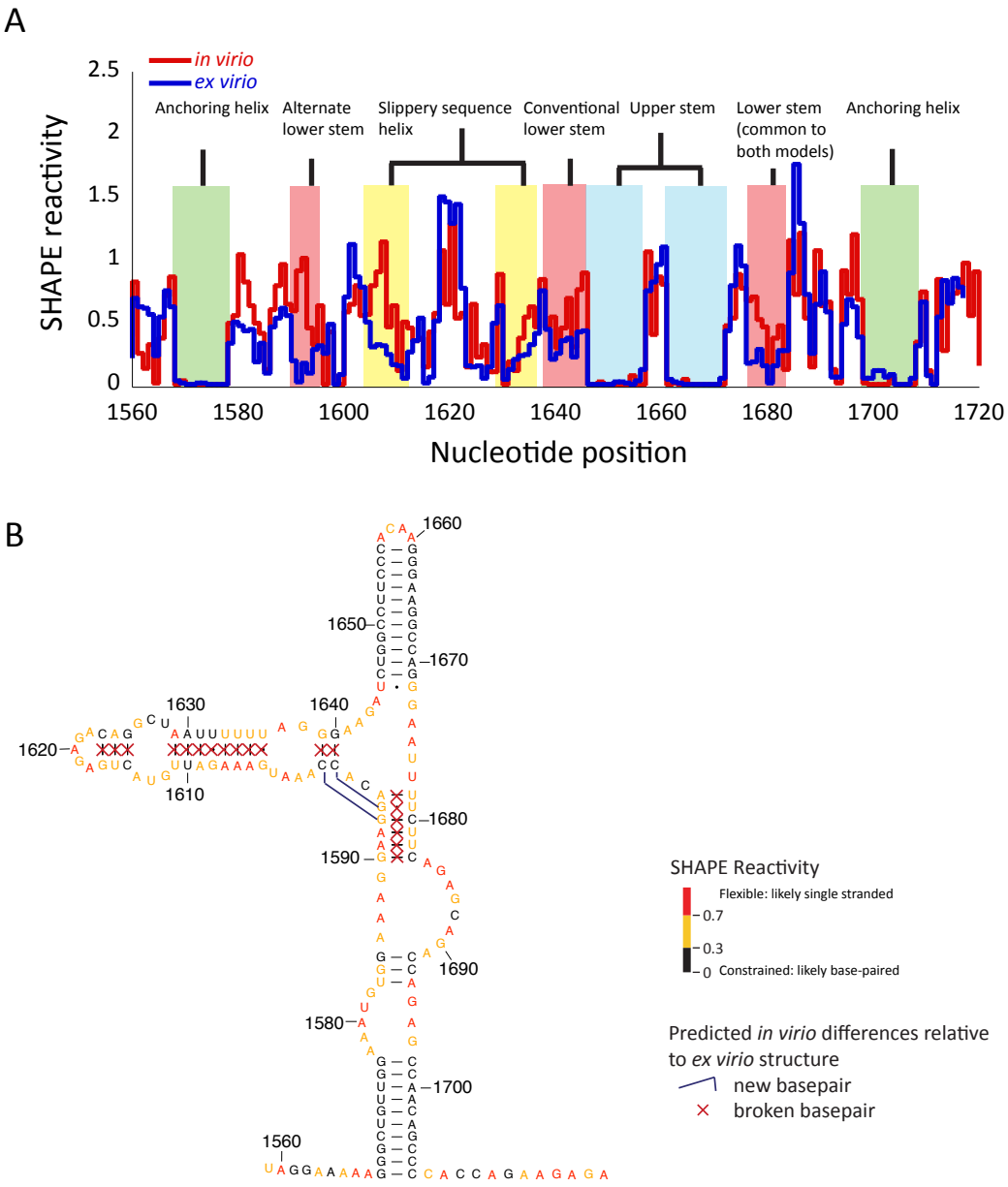

Figure 2.7 (A) SHAPE reactivity profiles and (B) predicted secondary structure models for *in virio* compared with *ex virio* RNA.

2.2.6 SHAPE probing of *in virio* genomic RNA reveals a less structured frameshift domain.

We next probed the frameshift region structure of HIV-1 RNA packaged inside authentic virions. Structural interrogation of this *in virio* state, which includes all proteins packaged with the RNA in the virion, is possible because SHAPE reagents readily cross biological membranes (25). Our results (Fig. 2.7) show that the frameshift domain adopts a much less structured conformation *in virio* as compared to the *ex virio* and refolded states. In particular, nucleotides involved in the slippery sequence helix and lower stem, including both the conventional and alternate base-pairings, display higher SHAPE reactivities. In contrast, the anchoring helix and upper stem are still present and appear to be the only significant structural elements within the frameshift domain.

2.3 Discussion

In this study, we use LNA binding monitored by SHAPE to provide the first independent support for the three helices unique to the frameshift domain model proposed by SHAPE-directed folding of an entire HIV-1 genome (14). Our model shares a stable upper stem with the currently accepted two-helix model but has two primary modifications. First, this study supports alternative pairing partners for the conventional lower stem. Second, the SHAPE-directed model incorporates the standard frameshift region into a larger 140 nt domain. This larger domain includes base-pairing interactions involving the slippery sequence and an additional stable anchoring helix.

A key distinguishing feature between the present study and prior research on the frameshift structure is our use of full-length genomic RNA. This allowed us to structurally interrogate the frameshift element in its complete sequence context. We are thereby able to avoid biases created when a truncated sequence of an RNA is studied. In fact, most past studies of the HIV-1 frameshift, including the NMR verifications of the conventional model, used HIV-1 sequences that were shorter than the 140 nt domain. All of the three helices unique to the SHAPE-directed model are unable to form in these truncated sequences. Furthermore, two of these helices, the alternate lower stem and the frameshift sequence helix, appear to stabilize each other as disruption of one helix by LNA binding can destabilize or cause refolding of the other. Additionally, formation of the stable anchoring helix is required for formation of both these helices.

Interestingly, the frameshift domain adopts the same structure whether the genomic RNA is probed directly after extraction from virions or first heat-denatured and then refolded. This suggests that the differences between the SHAPE-directed model and the conventional model are due primarily to the presence of complete sequence context in the SHAPE-directed model rather than to the native folding pathway which, in general, likely influences folding of long RNAs (26).

While our LNA binding experiments strongly support our 140 nt frameshift domain, our formamide denaturation experiments also indicate that this domain contains both highly stable, likely static structures, as well as less stable helices with the flexibility to form alternative structures. The anchoring helix and upper stem are highly stable and exist even in the presence of high amounts of formamide denaturant.

Their stability even appears to hold across diverse biological states, as these two helices are the only frameshift domain helices that are present inside the packaged virion. Between these two elements, a greater diversity of structural states is possible upon perturbation of the folded domain through either LNA binding or formamide denaturation.

The present study examines the structure and thermodynamics of the frameshift domain but does not directly address the functional implications of the model. Nevertheless, we can use the structural changes induced by LNA binding to provide a rough approximation of frameshift domain structural dynamics as it is unwound and translated by the ribosome (Fig. 2.8). The anchoring helix is the first frameshift domain secondary structural element to be unwound by the translating ribosome (Fig. 2.8B). This causes major structural rearrangement throughout the frameshift domain. The lower stem switches from the SHAPE-directed alternate to the conventional conformation, and the slippery sequence helix is significantly destabilized, potentially releasing slippery sequence nucleotides from their basepairing interactions. It is unclear what the functional implications of this structural rearrangement may be, but we note that the importance of conformational switching has recently been demonstrated in ribosomal frameshifting in related retroviruses (27). Additionally, it seems clear from prior studies that the conventional lower stem is functionally important for frameshifting (10,13).

After unwinding the anchoring helix, the ribosome continues over the slippery sequence and encounters the conventional lower stem. LNA 2 binding data suggest that unwinding of the conventional lower stem results in a switch back to the alternate

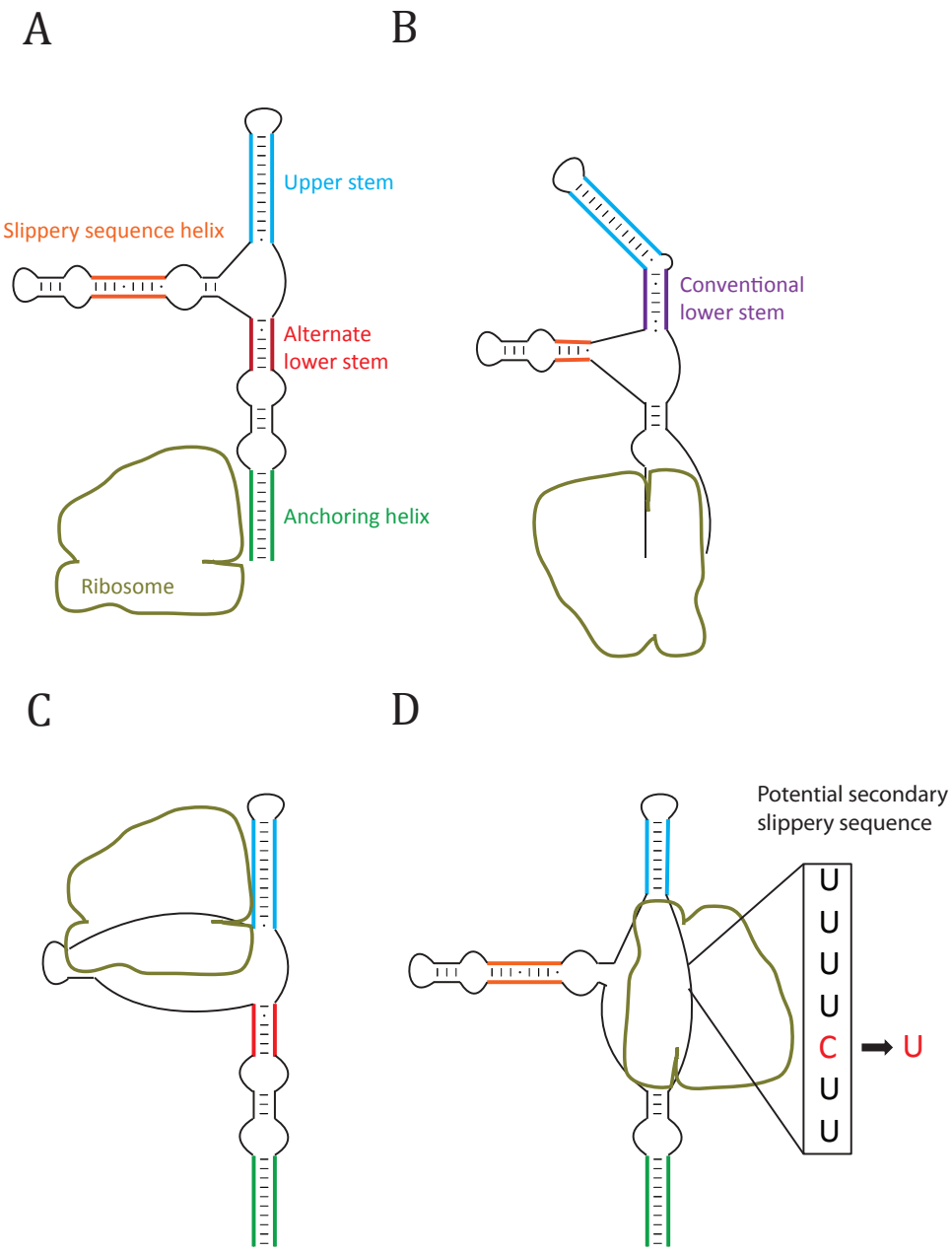

Figure 2.8 Proposed model for frameshift domain unwinding during translation. A PI-induced C-to-U mutation (red) creates a potential secondary slippery sequence.

lower stem (Fig. 2.8C). The ribosome must then unwind the very stable upper stem and switch reading frames. At this point, all frameshift domain helices will have been unwound. However, the high stability of the anchoring helix raises the possibility of its renaturation after the ribosome has translated through it. The ribosome would then encounter the anchoring helix for a second time before exiting the frameshift domain (Fig. 2.8D).

Intriguingly, a UUUUCUU sequence (nucleotides 1676-1682) lies just upstream from this potential second encounter with the anchoring helix (Fig. 2.8D). In viruses resistant to protease inhibitors (PI), this C1680 is frequently mutated to U, resulting in a UUUUUUU (Fig. 2.8D, red C → U) sequence that resembles the standard UUUUUUA slippery sequence at nucleotides 1631-1637 (28). This results in a cleavage site Leu to Phe mutation at the protein level which may increase cleavage efficiency and enhance the generation of functional protease. Additionally, Doyon *et al.* (29) hypothesized that this site could also act as a secondary slippery sequence that increases the overall amount of frameshifting, thereby increasing the relative amount of protease to compensate for reduced PI-induced protease activity. When the standard slippery sequence was inactivated by mutation, the mutant secondary slippery site, but not the wild-type, was able to stimulate frameshifting in *in vitro* translation assays. Furthermore, Doyon *et al.* (29) found evidence for frameshifting from this secondary site in virus-expressing cells. While these *in vitro* results have subsequently been confirmed independently, no evidence for frameshifting from this secondary site in cell culture was detected (30). However, these experiments used HIV sequences that were shorter than the 140 nt domain described here and therefore could not form the

anchoring helix. In future, it would be interesting to ask if, in the context of the complete domain, frameshifting can be enhanced by the PI-induced secondary slippery sequence with the anchoring helix acting as a secondary frameshift stimulatory stem.

In conclusion, this study confirms key structure elements specific to the SHAPE-directed frameshift model. We also demonstrate that this model has the ability to switch between the SHAPE-directed model and the conventionally accepted two-helix model. We hypothesize that this switch likely occurs as the ribosome unwinds the frameshift element, although the functional significance of this switch will need to be assessed in future work. This work underscores the influence of global sequence context on this important regulatory domain and implies that, at a minimum, all 140 nucleotides of the domain should be used when studying frameshifting in HIV-1.

2.4 Methods

2.4.1 HIV-1 virion production

HIV-1 virion particles were prepared as described previously (14,25). Briefly, HIV-1 strain NL4-3 (group M, subtype B) was used to infect a non-Hodgkin's T cell lymphoma cell line (31). Virions were purified by subtilisin digestion and centrifugation through a 20% (w/v) sucrose cushion as previously described (32).

2.4.2 Extraction of RNA genomes from virions

Subtilisin-treated virions were lysed by incubation in a virion lysis buffer (50 mM Tris pH 7.5, 10 mM EDTA, 1% SDS, 100 mM NaCl, 10 mM DTT, 15 μL 20 mg/mL Proteinase K) for 30 min at room temperature. The digest was extracted four times with phenol/chloroform/isoamyl alcohol, followed by four extractions with pure

chloroform. The aqueous layer was brought to a NaCl concentration of 300 mM, precipitated in 70% ethanol, and stored at -20˚C. To extract the RNA, we pelleted this solution by centrifugation at 14,000 rpm for 30 min, eluted off the ethanol layer, and vacuum dried the pellet for 1 min. We then resuspended the RNA pellet in a storage buffer (200 mM KOAc, 50 mM HEPES pH 8) for a final RNA concentration of about 400 nM. These aliquots were flash frozen in liquid N_2 and stored at -80˚C.

2.4.3 Folding of *ex virio* RNA.

For each reaction, 1 µL 400 nM *ex virio* RNA was resuspended in a Mg^{2+}-containing standard folding buffer (200 mM KOAc, 50 mM HEPES pH 8, 3 mM $MgCl_2$) to promote the stabilization of native-like interactions (total volume was 20 µL per reaction). We incubated this mixture at 37˚C for 30 min and then proceeded immediately to the SHAPE modification step (Section 2.4.8).

2.4.4 Formamide denaturation

For the formamide denaturation experiments, 1 µL 400 nM *ex virio* RNA was resuspended in 5 µL folding buffer and incubated at 37˚C for 20 min. A formamide-containing folding buffer (67% v/v deionized formamide, 200 mM KOAc, 50 mM HEPES pH 8, 3 mM $MgCl_2$) was then combined with the appropriate amount of standard folding buffer and added to the reaction mix to obtain the desired formamide concentration in a reaction volume of 20 µL. We performed these experiments in final formamide concentrations of 0% to 60%, in increments of 10%. We incubated this formamide-containing mixture for an additional 20 min at 37˚C and then proceeded immediately to the SHAPE modification step (Section 2.4.8).

2.4.5 LNA oligonucleotide design

We used 9 and 10 nt LNA oligonucleotides (Exiqon) that were the reverse complements of HIV-1 sequences comprising helices proposed in the SHAPE-directed frameshift model. The specific sequences were chosen to avoid self-complementary sequences due to very strong LNA-LNA binding affinities. We also tried to avoid stretches of 3 or more Gs or Cs. These considerations resulted in LNA oligonucleotides that, in the case of the 10-nt anchoring helix bound most of the targeted strand. Additionally, when possible we included flanking single stranded regions as part of the targeted strand to facilitate LNA binding to structured helices. LNA oligonucleotide sequences and binding sites are shown in Table 2.1 and Fig. 2.1

2.4.6 LNA binding to genomic RNA

For each LNA binding experiment, 1 µL 400 nM extracted HIV-1 genomic RNA in storage buffer (200 mM KOAc, 50 mM HEPES pH 8), 2 µL 2 µM LNA, 4.6 µL TE, and 1.7 µL water were mixed and heated at 95˚C for 5 min, and then snap cooled on ice. We then added 9.5 µL 2X storage buffer and 1.2 µL 50 mM $MgCl_2$ (20 µL total in folding buffer conditions) and incubated this mixture for 30 min at 37˚C before proceeding immediately to the SHAPE modification step.

2.4.7 SHAPE modification of *ex virio*, LNA-bound, and formamide denatured RNA

The SHAPE modification was performed by adding 9 µL each of the folded RNA mixture to both 1 µL 40 mM SHAPE reagent (1M7 for standard SHAPE reactions and 1M6 and NMIA for differential SHAPE reactions) and 1 µL neat DMSO as a no-reagent control. The reaction mix was incubated for 4 min at 37˚C. We then added 1 µL 50 mM

EDTA and performed a clean-up step to remove LNA oligonucleotides using the RNeasy Mini Kit (Qiagen) according to the manufacturer's instructions. The resulting mixture (100 µL) was ethanol precipitated by the addition of 10 µL 2 M NaCl and 300 µL ethanol and was stored at -80˚C until the primer extension step.

2.4.8 Primer extension and capillary electrophoresis detection of SHAPE adduct sites

SHAPE-modified RNA pellets were resuspended in 7 µL 0.5 X TE and 6 µL 0.4 µM VIC-labeled DNA primer (Applied Biosciences). Primer extension reactions for LNA binding experiments were performed using primers complementary to nucleotides 1750-1771 (primer 6.2, with sequence ATCGGCTCCTGCTTCTGAGAGG) and 2033-2054 (primer 7, with sequence CAATTATGTTGACAGGTGTAGG). We used primer 6.2 for formamide denaturation experiments and primer 7 for *in virio* experiments. In addition to primers 6.2 and 7, primers complementary to nucleotides 1522-1543 (primer 5.5, with sequence TTGGCTATGTGCCCTTCTTTGC) were also used for the ~700 nt comparison between *ex virio* and refolded RNA. To promote primer binding, this mixture was heated at 65˚C for 5 min, followed by 42˚C for 2 min, and then cooled on ice. We then added 7 µL primer extension reaction mixture (4 µL 5X first strand buffer, 1 µL 0.1 M DTT, 1 µL 10 mM each dNTP, 1 µL 100 U Superscript III reverse transcriptase, Invitrogen). This mixture was incubated at 45˚C for 10 seconds, 52˚C for 20 min, 65˚C for 5 min, and then cooled at 4˚C. The resulting cDNA products were precipitated by addition of 60 µL ethanol and stored at -80˚C for at least 30 min. We then centrifuged this ethanol solution at 14,000 rpm for 45 min, eluted off the ethanol layer, washed in 70% ethanol, pelleted, and then resuspended in 9 µL formamide. The cDNA solution was heated at 95˚C for 3 min to aid in dissolving the pellet. 1 µL of a

NED-labeled dideoxycytosine sequencing ladder stock was added. Dideoxy sequencing reactions (GenomeLab Methods Development Kit; Beckman) were performed using plasmid pNL43 and NED-labeled primers. An Applied Biosystems 3500 capillary electrophoresis instrument was used to quantify the cDNA products.

2.4.9 Data processing

Raw capillary electropherograms were processed using the custom QuShape software as described in (33). Briefly, key processing steps include a mobility shift to correct for small differences in the electrophoretic mobility between the NED and VIC fluorescent dyes, and a signal decay correction to account for signal attenuation as distance from the reverse transcriptase primer binding site increases. Nucleotide positions are assigned to reagent and DMSO control traces by aligning the dideoxy sequencing ladder with the nucleotide sequence using the sequence alignment tool. Peaks in the reagent and DMSO control traces are integrated and scaled relative to each other such that the lowest peaks in the reagent trace, which correspond to lowly reactive nucleotides, are of similar magnitude to their corresponding DMSO control peaks. DMSO control peaks are subtracted from reagent peaks and the resulting SHAPE reactivities are normalized on a scale where a normalized reactivity of 1.0 is defined as the average intensity of the top 10% most reactive peaks, excluding a few highly reactive nucleotides taken to be outliers. The resulting reactivities span a scale from 0 to ~1.5, where 0 indicates no reactivity (and a highly constrained nucleotide) and reactivities >0.7 typically indicate highly flexible nucleotides.

2.4.10 Secondary structure modeling

SHAPE-directed models for the frameshift domain were created by incorporating SHAPE data into the RNAstructure folding algorithm (16,17). SHAPE data are added as experimental corrections to the nearest neighbor energy function (34) as follows:

$$\Delta G_{\mathrm{SHAPE}}(i) = m \ln(\text{SHAPE reactivity}(i) + 1) + b \qquad (2.1)$$

These pseudo-free energy terms are added for each base-paired nucleotide *i* and are weighted by the parameters *m* and *b.* The parameter *m* weights a penalty for pairing nucleotides with high SHAPE reactivity, while the parameter *b,* a negative value, accounts for the energetic bonus of pairing lowly reactive nucleotides. The choice of parameter can depend on the RNA. For HIV, we use values of *m* = 3.0 kcal/mol and *b* = -0.6 kcal/mol. The value for *m* is higher than values typically used for folding more structured RNAs (1.9-2.6) and is used to counteract the tendency for over-prediction of base-pairs by folding algorithms. To account for LNA binding, the LNA target site was made single stranded by imposing artificially high SHAPE reactivity values of 100. For LNA 5 and 6, which target the highly stable anchoring helix, base-pairing was also prohibited at partner nucleotides as their reactivity increases were taken to imply a single stranded state.

2.5 Acknowledgements

We are indebted to Howard Fried for suggesting and advising us on the formamide experiments. We thank Nathan A. Siegfried and Joshua S. Martin for helpful discussions on the LNA binding experiments. This work was supported by National Institutes of Health grant AI068462 (to K.M.W.). J.T.L. was supported by a National

Research Service Award (F30DA027364), the Medical Scientist Training Program (T32GM008719), and the Program in Molecular and Cellular Biophysics (T32GM008570).

2.6 References

1. Brierley, I. and Dos Ramos, F.J. (2006) Programmed ribosomal frameshifting in HIV-1 and the SARS-CoV. *Virus Res*, **119**, 29-42.

2. Biswas, P., Jiang, X., Pacchia, A.L., Dougherty, J.P. and Peltz, S.W. (2004) The human immunodeficiency virus type 1 ribosomal frameshifting site is an invariant sequence determinant and an important target for antiviral therapy. *Journal of Virology*, **78**, 2082-2087.

3. Shehu-Xhilaga, M., Crowe, S.M. and Mak, J. (2001) Maintenance of the Gag/Gag-Pol ratio is important for human immunodeficiency virus type 1 RNA dimerization and viral infectivity. *Journal of Virology*, **75**, 1834-1841.

4. Brakier-Gingras, L., Charbonneau, J. and Butcher, S.E. (2012) Targeting frameshifting in the human immunodeficiency virus. *Expert Opin Ther Targets*, **16**, 249-258.

5. Gareiss, P.C. and Miller, B.L. (2009) Ribosomal frameshifting: an emerging drug target for HIV. *Curr Opin Investig Drugs*, **10**, 121-128.

6. Jacks, T., Power, M.D., Masiarz, F.R., Luciw, P.A., Barr, P.J. and Varmus, H.E. (1988) Characterization of ribosomal frameshifting in HIV-1 gag-pol expression. *Nature*, **331**, 280-283.

7. Le, S.Y., Shapiro, B.A., Chen, J.H., Nussinov, R. and Maizel, J.V. (1991) RNA pseudoknots downstream of the frameshift sites of retroviruses. *Genet Anal Tech Appl*, **8**, 191-205.

8. Du, Z., Giedroc, D.P. and Hoffman, D.W. (1996) Structure of the autoregulatory pseudoknot within the gene 32 messenger RNA of bacteriophages T2 and T6: a model for a possible family of structurally related RNA pseudoknots. *Biochemistry*, **35**, 4187-4198.

9. Dinman, J.D., Richter, S., Plant, E.P., Taylor, R.C., Hammell, A.B. and Rana, T.M. (2002) The frameshift signal of HIV-1 involves a potential intramolecular triplex RNA structure. *Proc Natl Acad Sci U S A*,, **99**, 5331-5336.

10. Dulude, D., Baril, M. and Brakier-Gingras, L. (2002) Characterization of the frameshift stimulatory signal controlling a programmed -1 ribosomal frameshift in the human immunodeficiency virus type 1. *Nucleic Acids Res*, **30**, 5094-5102.

11. Gaudin, C., Mazauric, M.H., Traikia, M., Guittet, E., Yoshizawa, S. and Fourmy, D. (2005) Structure of the RNA signal essential for translational frameshifting in HIV-1. *J Mol Biol*, **349**, 1024-1035.

12. Staple, D.W. and Butcher, S.E. (2005) Solution structure and thermodynamic investigation of the HIV-1 frameshift inducing element. *J Mol Biol*, **349**, 1011-1023.

13. Baril, M., Dulude, D., Gendron, K., Lemay, G. and Brakier-Gingras, L. (2003) Efficiency of a programmed -1 ribosomal frameshift in the different subtypes of the human immunodeficiency virus type 1 group M. *RNA*, **9**, 1246-1253.

14. Watts, J.M., Dang, K.K., Gorelick, R.J., Leonard, C.W., Bess, J.W., Jr., Swanstrom, R., Burch, C.L. and Weeks, K.M. (2009) Architecture and secondary structure of an entire HIV-1 RNA genome. *Nature*, **460**, 711-716.

15. Merino, E.J., Wilkinson, K.A., Coughlan, J.L. and Weeks, K.M. (2005) RNA structure analysis at single nucleotide resolution by selective 2'-hydroxyl acylation and primer extension (SHAPE). *J Am Chem Soc*, **127**, 4223-4231.

16. Mathews, D.H., Disney, M.D., Childs, J.L., Schroeder, S.J., Zuker, M. and Turner, D.H. (2004) Incorporating chemical modification constraints into a dynamic programming algorithm for prediction of RNA secondary structure. *Proc Natl Acad Sci U S A*, **101**, 7287-7292.

17. Deigan, K.E., Li, T.W., Mathews, D.H. and Weeks, K.M. (2009) Accurate SHAPE-directed RNA structure determination. *Proc Natl Acad Sci U S A*, **106**, 97-102.

18. Jepsen, J.S., Sorensen, M.D. and Wengel, J. (2004) Locked nucleic acid: a potent nucleic acid analog in therapeutics and biotechnology. *Oligonucleotides*, **14**, 130-146.

19. Kaur, H., Babu, B.R. and Maiti, S. (2007) Perspectives on chemistry and therapeutic applications of Locked Nucleic Acid (LNA). *Chem Rev*, **107**, 4672-4697.

20. Mortimer, S.A. and Weeks, K.M. (2007) A fast-acting reagent for accurate analysis of RNA secondary and tertiary structure by SHAPE chemistry. *J Am Chem Soc*, **129**, 4144-4145.

21. Steen, K.-A., Rice, G.M. and Weeks, K.M. (2012) Fingerprinting Noncanonical and Tertiary RNA Structures by Differential SHAPE Reactivity. *J Am Chem Soc*, **134**, 13160-13163.

22. Gherghe, C.M., Mortimer, S.A., Krahn, J.M., Thompson, N.L. and Weeks, K.M. (2008) Slow conformational dynamics at C2'-endo nucleotides in RNA. *J Am Chem Soc*, **130**, 8884-8885.

23. Blake, R.D. and Delcourt, S.G. (1996) Thermodynamic effects of formamide on DNA stability. *Nucleic Acids Res*, **24**, 2095-2103.

24. Marcheschi, R.J., Tonelli, M., Kumar, A. and Butcher, S.E. (2011) Structure of the HIV-1 frameshift site RNA bound to a small molecule inhibitor of viral replication. *ACS Chem Biol*, **6**, 857-864.

25. Wilkinson, K.A., Gorelick, R.J., Vasa, S.M., Guex, N., Rein, A., Mathews, D.H., Giddings, M.C. and Weeks, K.M. (2008) High-throughput SHAPE analysis reveals structures in HIV-1 genomic RNA strongly conserved across distinct biological states. *PLoS Biol*, **6**, e96.

26. Garst, A.D. and Batey, R.T. (2009) A switch in time: detailing the life of a riboswitch. *Biochim Biophys Acta*, **1789**, 584-591.

27. Houck-Loomis, B., Durney, M.A., Salguero, C., Shankar, N., Nagle, J.M., Goff, S.P. and D'Souza, V.M. (2011) An equilibrium-dependent retroviral mRNA switch regulates translational recoding. *Nature*, **480**, 561-564.

28. Doyon, L., Croteau, G., Thibeault, D., Poulin, F., Pilote, L. and Lamarre, D. (1996) Second locus involved in human immunodeficiency virus type 1 resistance to protease inhibitors. *Journal of Virology*, **70**, 3763-3769.

29. Doyon, L., Payant, C., Brakier-Gingras, L. and Lamarre, D. (1998) Novel Gag-Pol frameshift site in human immunodeficiency virus type 1 variants resistant to protease inhibitors. *Journal of Virology*, **72**, 6146-6150.

30. Girnary, R., King, L., Robinson, L., Elston, R. and Brierley, I. (2007) Structure-function analysis of the ribosomal frameshifting signal of two human immunodeficiency virus type 1 isolates with increased resistance to viral protease inhibitors. *J Gen Virol*, **88**, 226-235.

31. Means, R.E., Matthews, T., Hoxie, J.A., Malim, M.H., Kodama, T. and Desrosiers, R.C. (2001) Ability of the V3 loop of simian immunodeficiency virus to serve as a target for antibody-mediated neutralization: correlation of neutralization sensitivity, growth in macrophages, and decreased dependence on CD4. *Journal of Virology*, **75**, 3903-3915.

32. Ott, D.E., Coren, L.V., Johnson, D.G., Sowder, R.C., 2nd, Arthur, L.O. and Henderson, L.E. (1995) Analysis and localization of cyclophilin A found in the virions of human immunodeficiency virus type 1 MN strain. *AIDS Res Hum Retroviruses*, **11**, 1003-1006.

33. Karabiber, F., McGinnis, J.L., Favorov, O.V. and Weeks, K.M. (2012) Rapid, accurate and best-practices quantification of nucleic acid probing information, resolved by capillary electrophoresis. *RNA,* **18**, in press

34. Xia, T., SantaLucia, J., Jr., Burkard, M.E., Kierzek, R., Schroeder, S.J., Jiao, X., Cox, C. and Turner, D.H. (1998) Thermodynamic parameters for an expanded nearest-neighbor model for formation of RNA duplexes with Watson-Crick base pairs. *Biochemistry*, **37**, 14719-14735.

CHAPTER 3

SHAPE-DIRECTED DISCOVERY OF POTENT SHRNA INHIBITORS OF HIV-1

3.1 Introduction

Interactions between RNAs and molecular ligands, proteins, and other RNAs govern numerous cellular regulatory processes. These targeting and binding events are strongly influenced by the structure of the target RNA (1). One biologically and clinically important example of intermolecular interactions between RNAs involves the RNA interference (RNAi) pathway (2). The RNAi pathway regulates gene expression in organisms from plants to humans (3) and immune defense via destruction of pathogenic RNAs (4). This pathway can be exploited to destroy pathogenic RNAs using synthetic short interfering RNA (siRNA) or short hairpin RNA (shRNA) expression vectors (5). The ~19 nucleotide guide strands generated from cellular transcripts or synthetic RNAs are loaded into the RNA-[2]induced silencing complex (RISC). Base complementarity between the guide strand and target RNA signals the Argonaute protein in RISC to cleave the target RNA. Both siRNA and shRNA approaches have been used successfully to inhibit HIV-1 production and replication in cell culture (6-8).

The pathways for incorporation of siRNAs into RISC and their recognition of RNA targets are complex and not all sequences can be targeted efficiently. Most

---

This chapter has been published in Low J.T., Knoepfel S.A., Watts J.M., ter Brake O., Berkhout B., Weeks K.M. *Mol Ther*. 2012. **20**: 820-828. The Weeks laboratory created the shRNA design rules and the Berkhout laboratory performed the viral inhibition assays. Low J.T. and Knoepfel S.A. contributed equally.

randomly selected sequences are not efficiently repressed by siRNAs or shRNAs directed against them (6, 9). Accurate identification of repressible sequences remains an unmet challenge that has motivated the development of a wide variety of target selection algorithms (9-22). Most algorithms were developed for selection of siRNAs and are usually assumed to apply to shRNA design, although there is evidence that siRNA and shRNA prediction require distinct, but overlapping, rules (23, 24). Degradation of transfected siRNAs *in vivo* makes them primarily suitable for short-term clinical applications, such as the treatment of acute infection. In contrast, for stable, long-term suppression as likely required for chronic infections, including HIV-1, we are especially interested in understanding the rules that govern shRNA-directed inhibition.

ter Brake *et al*. (6) reported the ability of 84 shRNA constructs to inhibit HIV-1 production in cell culture. This set of inhibitors was attractive as a training dataset because it was developed without using any si/shRNA selection rules. With a view towards potential therapeutic applications, shRNAs were instead chosen based on sequence conservation in the HIV-1 RNA. In addition, viral inhibition was assessed at low, generally sub-saturating, shRNA transfection levels. As a result, viral inhibition levels achieved by these shRNAs spanned a wide range of inhibition levels.

Correlations between virus production inhibition by shRNAs in this dataset (6) and rankings given by previously described prediction algorithms (9, 12, 14-21) are generally poor. This poor performance includes algorithms both that consider sequence signatures in the target RNA sequence and that additionally incorporate thermodynamic metrics to identify favorable interactions between an si/shRNA and its target (Table 3.1).

Algorithm	Reference	$\|r\|$
Approaches based primarily on sequence characteristics:		
Amarzguioui	17	0.33
BIOPREDsi	12	0.30
Dharmacon	9	0.15
DSIR	21	0.51
i-Score	20	0.30
Katoh	18	0.11
Takasaki	19	0.05
Approaches that directly incorporate RNA structure metrics:		
RNAxs	14	0.28
Sirna	15,16	0.13
Approaches based solely on RNA structure metrics, described in this study:		
No constraints		0.36 (ΔG_{target})
		0.38 (ΔG_{total})
With SHAPE		0.72 (ΔG_{target})
		0.61 (ΔG_{total})

Table 3.1: Correlation between HIV-1 inhibition and si/shRNA target prediction algorithms

We therefore sought to explore whether nucleotide-resolution information about an RNA target structure might make it possible to design potent shRNA inhibitors efficiently. We show that, if the underlying RNA structure is known with good accuracy, very simple thermodynamics-based rules yield excellent predictions for highly potent shRNA inhibitors of HIV-1 replication. Our prediction accuracy exceeds all current approaches when applied to the HIV-1 RNA genome, a notable result given that the rules developed in this work are much simpler than alternative approaches. In broad terms, this work shows how profoundly RNA structure influences biological function and emphasizes the importance of developing high-content models for an RNA fold to understand RNA-based therapeutics and biological mechanisms.

3.2 Results

3.2.1 Strategy

To derive new rules for designing shRNA inhibitors, we focused on one of the simplest possible models for the thermodynamics of the guide strand-HIV RNA target interaction. In this model (Fig. 3.1), the unstructured guide strand binds to a complementary region of the target RNA to form the guide strand-target duplex. We assumed that protein contacts with RISC maintained the guide strand in a single stranded conformation, poised to interact with the target RNA. This equilibrium is thus described by a free energy change, ΔG_{duplex}, and is calculated using nearest neighbor thermodynamic rules (25, 26). ΔG_{duplex} depends only on the RNA sequence and is independent of RNA structure because the unstructured guide strand is assumed to interact with a fully unfolded site in the target RNA.

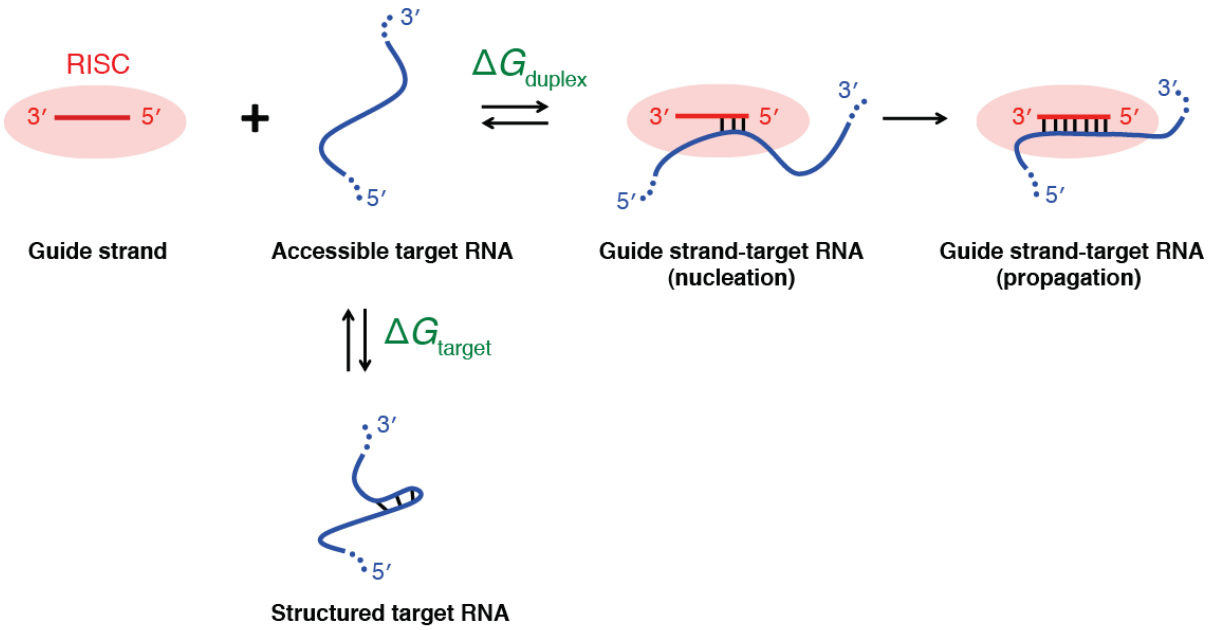

Figure 3.1: The guide strand-target RNA interaction equilibrium. RISC Argonaute protein is represented by a red oval, although only RNA-RNA thermodynamics were considered in this study.

In reality, the target RNA folds back on itself to form base paired secondary (and higher order) structures. Thus, a prerequisite for effective binding by RISC is that a site in the target RNA be unfolded to allow interaction with the guide strand. The strength of these pre-existing interactions is termed ΔG_{target} (Fig. 3.1). We consider a very simple model in which ΔG_{duplex} and ΔG_{target} dominate the equilibrium for forming a putative guide strand-target RNA interaction. The total free energy change ΔG_{total} of the interaction reflects a favorable contribution from duplex formation and the unfavorable cost of disrupting pre-existing structures in the target RNA:

$$\Delta G_{\text{total}} = \Delta G_{\text{duplex}} - \Delta G_{\text{target}} \quad (3.1)$$

In contrast to ΔG_{duplex}, which is independent of RNA structure, accurate calculation of the free energy change required to unfold the target RNA (ΔG_{target}) depends critically on the RNA structure model. Conventional thermodynamics-based RNA secondary structure prediction algorithms typically attain accuracies of 50-70%; accuracies are at the lower end of this range as RNA length increases (26, 27). This level of accuracy provides a helpful overall glimpse of an RNA structure but, in the context of HIV-1 inhibition of shRNAs, is insufficient for consistent prediction of optimal guide strand binding sites (Table 3.1). Secondary structure predictions can be improved dramatically by incorporating additional experimental information. In particular, nucleotide-resolution measurements of molecular structure obtained from SHAPE (selective 2'-hydroxyl acylation analyzed by primer extension) chemical probing experiments (28, 29) can be incorporated as pseudo-free energy corrections into a thermodynamics-based RNA folding algorithm (30). The resulting RNA secondary structure models are generally highly accurate even for RNAs on the kilobase scale (27).

We therefore used a SHAPE-directed secondary structure model of an entire ~9 kb HIV-1 genome (31) to calculate ΔG_{target}.

3.2.2 Concentration dependence of shRNA inhibition.

Ideally, RNAi-mediated knockdown of a target gene should be accomplished using the lowest effective concentration of shRNA, for two reasons. First, the RNAi pathway contains a finite complement of protein mediators, which can become saturated by the expression of large amounts of exogenous siRNA. Such saturation is thought to be an important cause of off-target effects and of general cell toxicity (32, 33). Second, artificial production of large amounts of guide strand-RISC complexes can make it possible to target both optimal and sub-optimal sequences and thus obscure important differences in targetability.

We therefore sought to determine the minimum level of transfected shRNA-encoding plasmid that achieved inhibition of HIV-1 production in our cell-based assay (6). We titrated plasmids expressing five shRNA sequences over the range from 1 to 125 ng (Fig. 3.2). Individual shRNAs differ significantly in their ability to inhibit HIV-1 production and inhibition by a given shRNA increased as amount of transfected plasmid increased. All five shRNA sequences tested showed significantly stronger inhibition at 125 ng transfected plasmid versus 25 ng plasmid. In this work, we use 25 ng transfected plasmid because this amount showed a high level of knockdown for optimal sequences, was sub-saturating in our experimental system, and is therefore most appropriate for facilitating accurate identification of highly potent shRNAs.

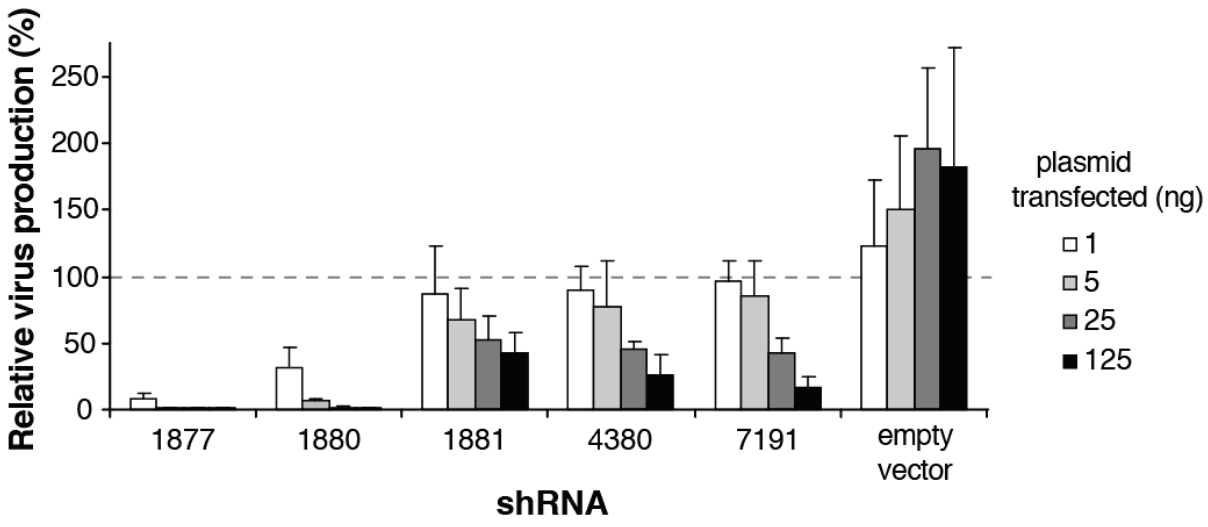

Figure 3.2: Relative levels of virus production for five shRNAs. shRNA-encoding plasmids were transfected into 293T cells in amounts ranging from 1 to 125 ng per well. Each shRNA is labeled by the first nucleotide position of its binding site on the NL4-3 HIV-1 mRNA (see Appendix 1).

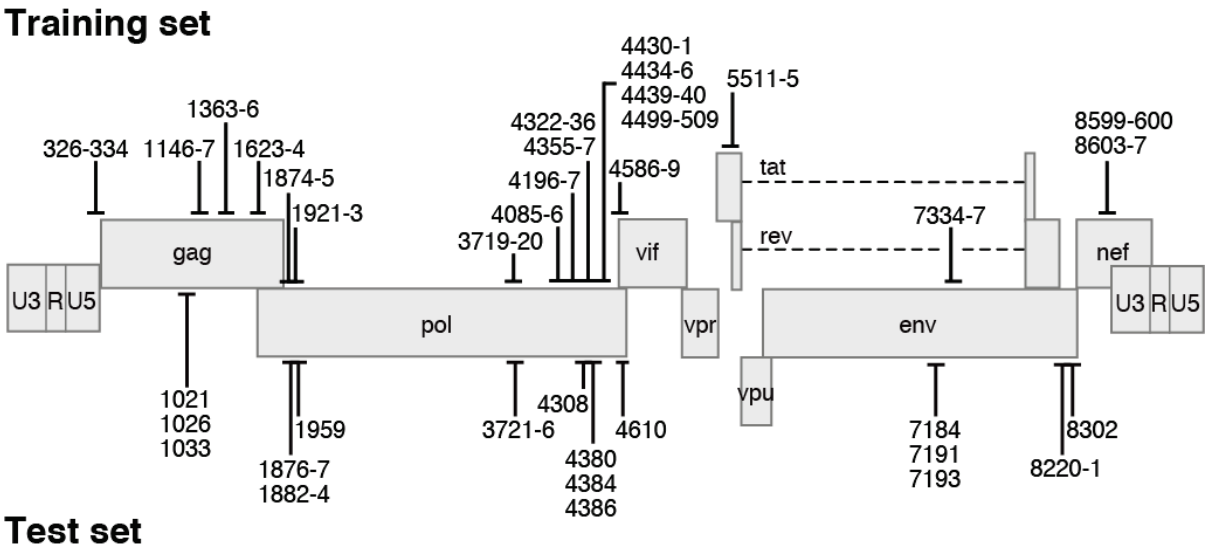

Figure 3.3: HIV-1 genome locations of the 84 target sequences for the shRNAs in the ter Brake *et al.* dataset (6) used to derive design rules (top) and of the 26 sequences which matched the design rules defined in this work (bottom). Numbers indicate the position of the 5′ nucleotide of each shRNA target site in the HIV-1 NL4-3 mRNA.

3.2.3 Weak target folding energy characterizes effectively repressed sequences.

Local accessibility has been shown to be an important determinant for efficient si/shRNA-mediated knockdown of a target gene (14, 16, 34-37) (see ΔG_{target}, Fig. 3.1). However, it is not obvious precisely which portion of the target RNA sequence needs to be accessible, or unfolded. An unfolding window is characterized by two parameters: its size and position. We calculated the free energy change, ΔG_{target}, of base pair formation in the SHAPE-based HIV-1 RNA structure (31) as a function of window size and position. We then calculated the linear correlation coefficient, *r*, between these ΔG_{target} values and the experimental viral production inhibition values obtained by ter Brake *et al*. (6) for each of the 84 shRNAs in the training set (Fig. 3.3 and Appendix 1). The magnitudes of the correlation coefficients quantify the strength of the ΔG_{target} metric for predicting inhibition, whereas the window size and position parameters identify the target RNA window that should be unstructured for optimal shRNA-mediated inhibition (Fig. 3.4).

The strongest correlation was obtained for a 13-nt window that begins at position 14 of the target RNA (Fig. 3.4A, white box) and has an *r*-value of -0.72 (Fig. 3.5A). The negative correlation confirmed that more readily unfolded, or less structured, target windows were more readily silenced. The first 5-6 nucleotides of the position window overlapped closely with the "seed region", the guide strand sequence that interacts initially with the target RNA prior to complete unfolding of the target to form the ~19-nt long duplex (38) (Fig. 3.1).

Unexpectedly, the 13-nt window also extended 7 nucleotides beyond the 3′ end of the target RNA binding site (Fig. 3.4B, grey box). This indicates that the most

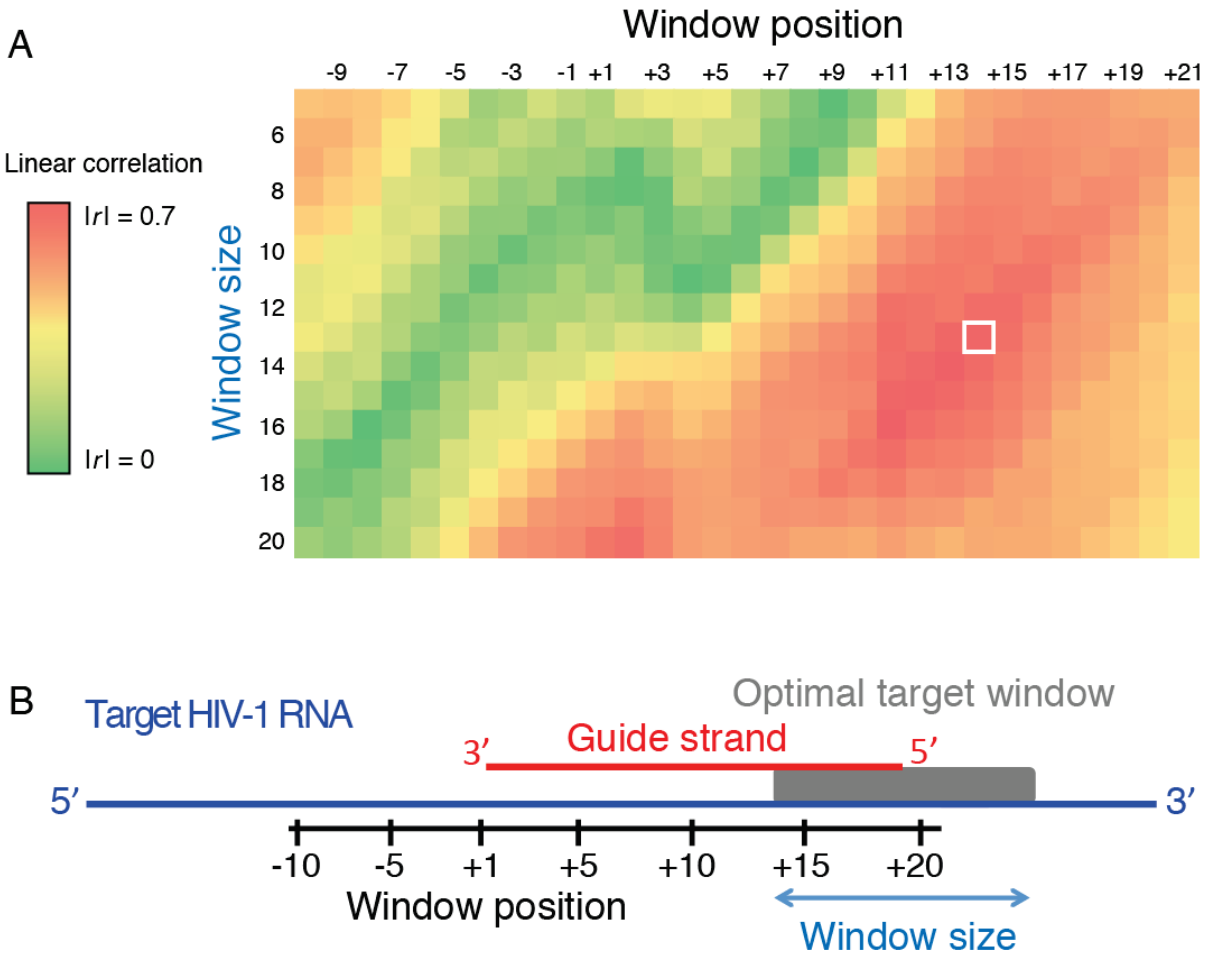

Figure 3.4: Correlation coefficients (r) between calculated target folding energies, ΔG_{target}, and experimental activity values for the 84 shRNAs in the training dataset. (A) Linear r-values as a function of target unfolding window size (vertical axis) and position (horizontal axis). Colors denote the relative strength of the correlation. A white box highlights the strongest correlation. (B) Optimal accessible target window. Window positions are numbered relative to the 5′ end of the guide strand binding site on the target RNA. The window size denotes the length of the window extending downstream of the window position value. The accessible target window that yielded the strongest correlation is shown by a grey rectangle.

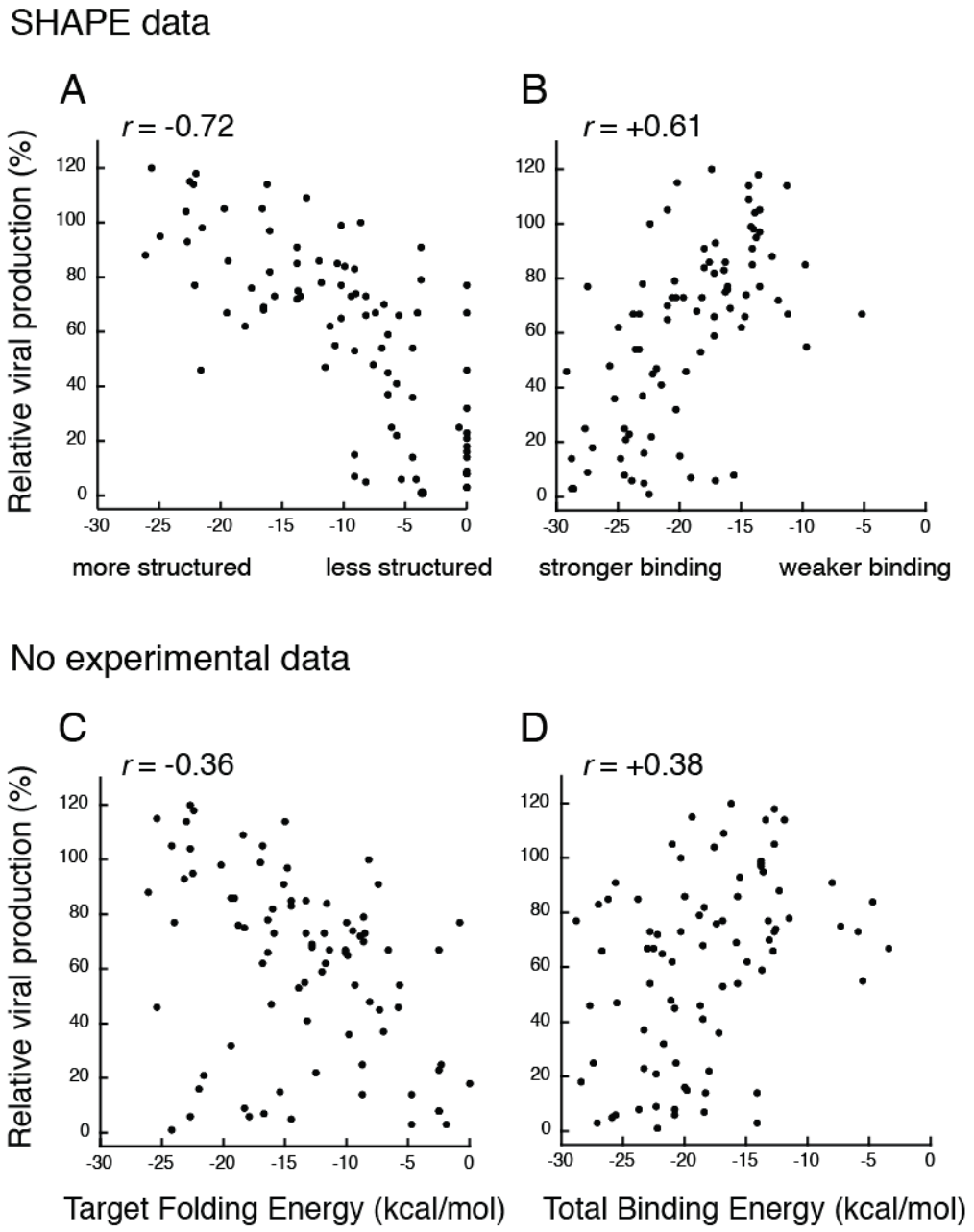

Figure 3.5: Relative viral production versus (A) target folding energies, ΔG_{target}, and (B) total binding energies, ΔG_{total}, for the 84 shRNAs in the training dataset. The optimal target unfolding window, identified in Fig. 3.4, was used for ΔG_{target} calculations. The SHAPE-directed HIV-1 secondary structure model (31) was used to calculate ΔG_{target}. The same correlations for (C) ΔG_{target} and (D) ΔG_{total} calculated *without* using experimental constraints to estimate the secondary structure.

effectively targeted RNA sequences are characterized by a 13-nt unstructured window that includes the seed region binding site and a previously unrecognized requirement that extends ~7 additional nucleotides beyond the region directly bound by the guide strand in RISC.

3.2.4 Strong total binding energy characterizes effectively repressed sequences.

The formation of an approximately 19-nt duplex between guide strand and target is required for proper recognition and subsequent cleavage of the target by RISC Argonaute proteins. We estimated the strength of this binding as the overall binding free energy ΔG_{total} of the complete 19-nt interface. We then computed the correlation between ΔG_{total} and viral production inhibition for each of the shRNAs in the training set. Total binding energy correlated strongly with shRNA inhibition (r = 0.61) (Fig. 3.5B).

3.2.5 Strong thermodynamic correlations are specific to the SHAPE-directed RNA structure model.

Strong correlations between HIV-1 inhibition and the energetic cost of disrupting pre-existing structures in the viral RNA (ΔG_{target}) and for overall strength of guide strand binding (ΔG_{total}) were obtained when these free energies were calculated using the experimentally-supported model for an HIV-1 genomic RNA (31). This model was obtained using authentic genomic RNA gently extracted from virions and was used to represent structures at any targetable stage in the HIV-1 replication cycle. This SHAPE-directed model shares only ~45% of base pairs with a model obtained using the same nearest-neighbor parameters but without experimental data (data not shown).

Using the structure predicted without experimental SHAPE constraints, we obtained much weaker correlations between viral inhibition and any simple thermodynamic metric for guide strand interaction. The correlations between viral production values for the training set shRNAs and ΔG_{target} calculated for the 13-nt window or for ΔG_{total}, which includes the guide strand-target duplex formation interaction, had modest *r*-values of -0.36 and +0.38, respectively (Figs. 3.5 C, D). These correlations, although poor, are actually at the higher end relative to current si/shRNA prediction algorithms (Table 3.1), even though these later approaches use more complex rules than the very simple thermodynamic approach outlined here (Fig. 3.1).

These results emphasize that target RNA secondary structure plays a profound role in RNAi activity, that current thermodynamics-only calculations do not recapitulate this contribution, and that SHAPE-directed secondary structure prediction provides significant additional information.

3.2.6 Experimental validation of shRNA design rules.

The strong correlations between inhibition of viral production and ΔG_{target} and ΔG_{total}, calculated using the SHAPE-derived secondary structure for HIV-1 (Figs. 3.5 A, B), suggest two remarkably simple rules for shRNA design. First, the target RNA in the newly defined, optimal 13-nt window should have minimal pre-existing structure. Second, the total binding energy for the guide strand-target RNA interaction should be strong. We tested these two rules by designing a new, independent set of shRNA inhibitors and measured their ability to inhibit HIV-1 viral production. We calculated ΔG_{target} and ΔG_{total} for all possible 19-nt sequences in the 9,173 nt NL4-3 HIV-1 genome and initially required ΔG_{target} to be greater than or equal to 0 kcal/mol and ΔG_{total} to be

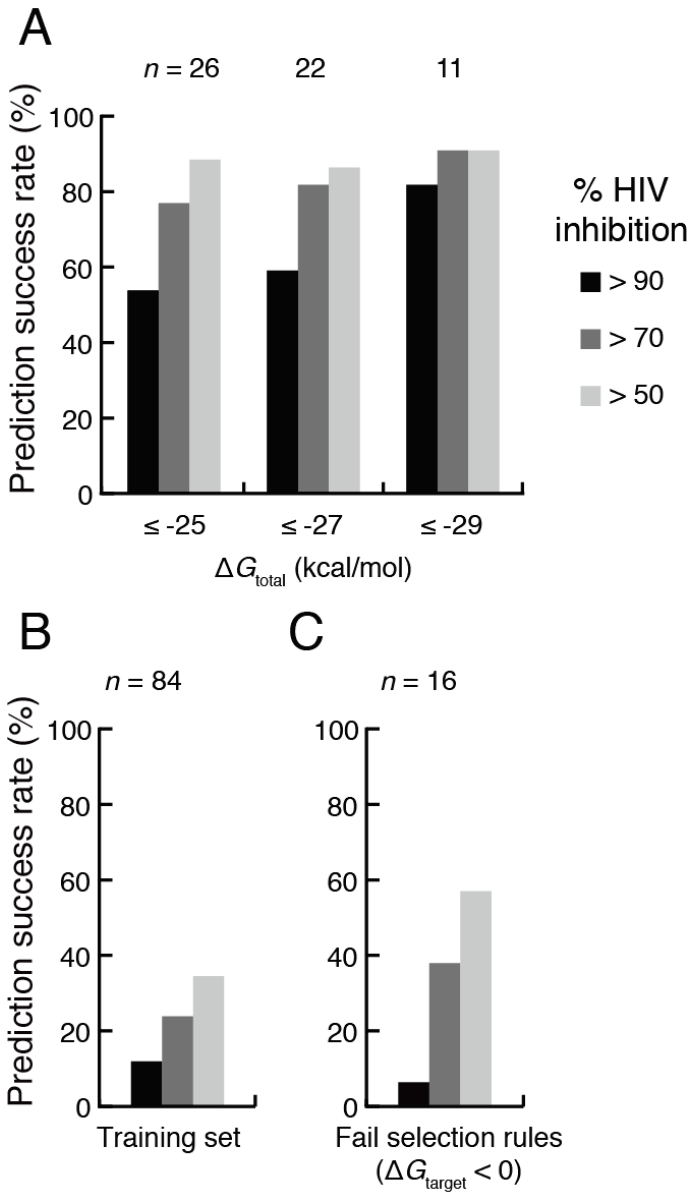

Figure 3.6: Prediction success rates of designed shRNAs. (A) Inhibition of HIV-1 production by shRNAs in the Test set. Target sequences were chosen to have accessible 13-nt windows ($\Delta G_{\text{target}} \geq 0$ kcal/mol) and strong overall binding energy ΔG_{total}. Prediction success rates are shown for ΔG_{total} criteria of -25, -27 and -29 kcal/mol; *n*, the numbers of shRNAs meeting this threshold. (B) Inhibition of HIV-1 production by shRNAs in the 84-member Training set. (C) Prediction success rates for 16 shRNAs that failed the target accessibility criterion. A $\Delta G_{\text{target}} < 0$ corresponds to RNA target sites with some pre-existing structure.

less than -25 kcal/mol. Approximately 500 sequences (~5% of all possible 19-mers) satisfied these two rules. Of these, we tested 26 randomly-selected sequences (Fig. 3.3, bottom panel; and Appendix 2).

The percentages of shRNAs that achieved a defined level of HIV-1 inhibition were calculated for the initial training set and for the independently designed test sequences (Fig. 3.6A). Strikingly, 23 of the 26 shRNAs (88%) selected based on our rules reduced HIV-1 production by a factor of 2 or more. Moreover, this simple thermodynamics-based approach was especially successful at identifying highly potent inhibitors: 54% (14/26) of the designed shRNAs inhibited viral production by 90% or greater (see -25 kcal/mol data, Fig. 3.6A). Very simple thermodynamics-based selection rules thus yielded a dramatic improvement in selection of potent shRNAs (compare Figs. 6A and 6B).

The total binding energy plays a major role in governing shRNA inhibition. Increasing the stringency of ΔG_{total} from -25 to -27 and to -29 kcal/mol yields a monotonic increase in prediction success of the most potent shRNA inhibitors in the test set (Fig. 3.6A). At the -29 kcal/mol threshold, 82% (9/11) of designed shRNAs inhibit viral production by 90% or greater (Fig. 3.6A). In the HIV-1 genome, only about 2% of 19-mers are both completely accessible in the 13-nucleotide optimal window and bind at the ≤ -29 kcal/mol threshold.

To further evaluate the importance of the target accessibility rule, we also assayed 16 shRNAs that had total binding energies < -25 kcal/mol but did not conform to the rules developed here because they had nonzero target folding energies in the optimal 13 nt window. Of these sequences, 56% (9/16) reduce HIV-1 viral production

by a factor of 2 or more but only one of the sixteen shRNAs (6%) resulted in highly potent, greater than 90%, inhibition (black column, Fig. 3.6C). Poor inhibition by these sequences emphasizes the importance of an accessible optimal target window for potent RNAi-mediated repression.

3.2.7 shRNA repression and toxicity in human T cells.

Measuring shRNA-mediated inhibition by the 293T cell transfection assay used in this study has significant advantages because of its quantitative accuracy. However, an shRNA-based HIV-1 therapeutic will need to be effective in natural host immune cells. We therefore used a lentiviral vector to stably transduce a human T cell line, SupT1, with single copies of selected shRNA expression constructs identified in our test set. Cells were subsequently challenged with low and high doses of HIV-1 and the durability of inhibition was monitored (Fig. 3.7). In all cultures, HIV-1 production was either completely inhibited or was significantly delayed by shRNA expression, whereas HIV-1 replicated efficiently on cells transduced with the empty JS1 vector.

A key concern for therapeutic shRNA use is the potential for stimulating unintended off-target and cytotoxic effects. To quantify these effects, we transduced SupT1 cells with lentiviral constructs expressing this same set of shRNAs and measured the impact of lentiviral vector integration and shRNA expression using a competitive cell growth assay (39). No negative effect was caused by integration of the empty lentiviral vector, as observed previously (39). Of the shRNA constructs from our test set that were evaluated (Fig. 3.8), we observed no effects for shRNAs 1033, 1876, 4308, 4610, and 8302, and only minimal effects on SupT1 cell growth for shRNAs 8220 and 8221. Only one shRNA (4384) caused a significant reduction in cell growth (of ~4.5%).

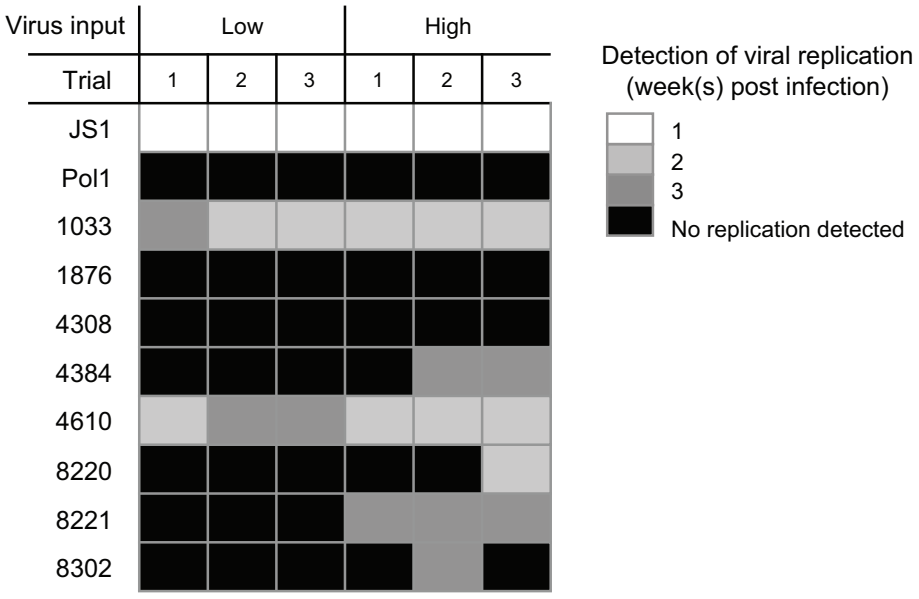

Figure 3.7: Inhibition of HIV-1 replication in transduced SupT1 T cells. Cells were transduced with the empty JS1 lentivirus (negative control), JS1-shPol1 (a known effective inhibitor) (6), or lentiviral variants expressing 8 shRNAs randomly selected from among the most potent test set shRNAs. Cultures with CA-p24 amounts above a 1 ng/ml threshold were scored as positive for viral replication. The color code indicates when virus replication was apparent: within one week (white), two weeks (light grey), three weeks (dark grey), or no observable replication for up to 2 months (black).

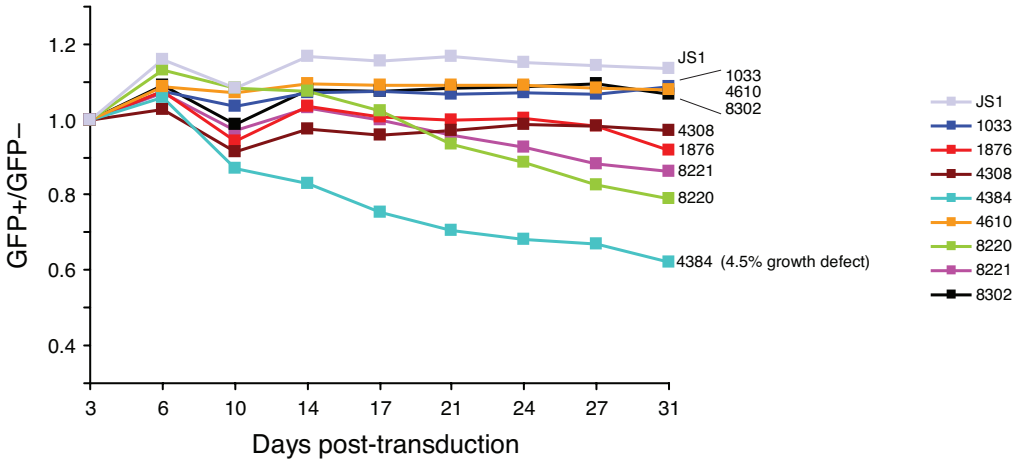

Figure 3.8: Competitive cell growth curves of representative potent shRNAs from the test set. SupT1 T cells were transduced with lentiviral vectors expressing both shRNA and GFP and cultured together with non-transduced SupT1 T cells. To score effects induced by the lentiviral integration, cells were transduced with the empty JS1 vector expressing GFP but no shRNA. FACS measurements were used to quantify GFP+ and GFP– cell populations, corresponding to transduced and non-transduced cells, respectively. We plot GFP+/GFP– ratios (y-axis), which quantify cell growth defects (39). Cell samples were obtained twice weekly directly before cell passaging. One representative experiment of two repetitions is shown.

In sum, shRNAs identified in the quantitative cell-based assay using 293T cells (Fig. 3.6) also inhibit HIV-1 replication when stably transduced into T cells (Fig. 3.7) and generally show no or minimal impairment of cellular replication (Fig. 3.8).

3.2.8 Partial SHAPE information is sufficient to identify potent shRNA inhibitors.

The requirement for performing SHAPE to develop a high-content secondary structure model is the experimental cost of this approach for accurate shRNA design. SHAPE is rapidly becoming easier to perform and, with current mature technologies, it is straightforward to obtain structural data for ~500 nts (29). We thus evaluated whether obtaining partial SHAPE information might be sufficient to identify potent shRNA inhibitors. Prior experience emphasizes that there can be very strong "end effects" in RNA folding such that incorrect definition of the 5′ and 3′ ends of an RNA can cause large re-folding at internal sequences. We therefore used SHAPE data from two 500-nt regions, each flanked by 1,000 additional nucleotides of HIV-1 sequence in our folding analysis. Two test regions were chosen based on their spanning the largest number of shRNAs in our test set. We folded each of the two 2,500 nt regions (spanning nucleotides 601-3100 and 3201-5700), using SHAPE data for only the central 500 nucleotides (1601-2100 and 4200-4700). We then calculated the resulting free energies ΔG_{target} and ΔG_{total} for the test shRNAs in these regions. The energy values obtained using these partial folds are similar to energies obtained when using the complete genome model. In contrast, the structural models obtained without using SHAPE constraints yield free energy values that agree poorly with the SHAPE-directed models (Appendix 3). This analysis suggests that shRNA design is significantly improved through the inclusion of partial SHAPE data for a large RNA.

3.3 Discussion

Essentially all recognition processes involving RNA are critically dependent on the underlying base paired secondary (and higher-order tertiary) structure. The central role of accessibility at single target sites is well established for RNAi-mediated knockdown (14, 16, 34-37). Correspondingly, siRNA and shRNA prediction methods often incorporate estimates of target site accessibility into their algorithms. However, the structure of a long target RNA is generally incompletely understood *a priori* and the resulting correlations between predicted and effective si/shRNAs are often poor (Table 3.1). Given this difficulty, newer algorithms have tended to become more complex and meld thermodynamic calculations with sequence signature and heuristic rules. However, these rules, applied to shRNA-mediated inhibition of HIV-1 production, do not consistently identify potent inhibitors.

In this work, we find that an extremely simple approach, involving the calculation of only two straightforward thermodynamic terms, significantly outperforms existing approaches when applied to inhibition of HIV-1 (Table 3.1). Our model considered only two simple RNA-RNA interactions central to the RISC ribonucleoprotein machinery (Fig. 3.1). Strong inhibition correlated with weak free energies of target folding (r = -0.72) within an optimal 13-nt window (Fig. 3.4b, grey bar) and with strong total binding energy (r = 0.61). These correlations were much weaker when SHAPE data was not used to direct calculation of the target HIV-1 RNA secondary structure model (Fig. 3.5 and Table 3.1), highlighting the requirement for an accurate target RNA structure in selection of shRNAs.

The correlation coefficient for our total binding energy metric is moderately weaker than that for the target folding energy metric ($|r|$ = 0.61 versus 0.72, respectively). However, requiring stronger ΔG_{total} improves the prediction success rate for sequences containing an optimal, fully accessible target window. Additionally, sequences with strong ΔG_{total} but less accessible optimal target windows were rarely potently repressed (Fig. 3.6C). Thus, a completely accessible optimal window appears critical for efficient repression and, once this condition is met, strong total binding energy improves prediction accuracies.

The correlations are consistent with models of target RNA association with the guide strand that involve an initial interaction with the seed region, followed by propagation to form a duplex containing all guide strand nucleotides (Fig. 3.1) (38, 40, 41). Our data also identify a previously unrecognized feature in which the optimal accessible target window extends 7 nucleotides downstream of the seed region binding site (Fig. 3.4). The required lack of secondary structure in this region of the target RNA may reflect unexplored interactions involving protein components of RISC.

Many RNAi design criteria are based on specific sequence signatures found more frequently in effectively repressed shRNA targets. Some of these signatures are consistent with the results of the present study. In particular, the observed preference for (more weakly pairing) A/U nucleotides at the 3′ end of the target binding interface (9, 42, 43), sometimes termed the asymmetry rule, likely corresponds to a qualitative sequence signature for an accessible seed region, which we quantify as ΔG_{target}. Our work emphasizes that strong correlations can be obtained using structure-based

thermodynamic metrics without considering sequence characteristics, and may reflect a more direct physical basis for observed sequence effects.

In designing shRNAs to test our two structure-based design principles, we ignored other design criteria. Consequently, many of our successful test shRNAs violate sequence-based si/shRNA design principles identified in previous studies. These include having an A/U at position 10 of the guide strand to facilitate cleavage at this site (44) and avoidance of consecutive runs of identical nucleotides. Nevertheless, our tested shRNAs achieved highly potent HIV-1 inhibition (Fig. 3.6A), suggesting that these sequence-based design rules have limited applicability in this system.

There were two distinctive features of this study that may explain differences, and the relative success of our simple approach, as compared to prior work.

First, several prediction algorithms have emphasized the role of pre-existing target RNA structure in reducing RNAi efficiency (14-16, 22) and have obtained good siRNA predictions in the systems studied. However, we find that these measures of target accessibility do not correlate with shRNA-mediated knockdown for the training dataset used in our study (Table 3.1). The importance of structural accessibility and for an accurate model of secondary structure in the target RNA may vary with the targeted system and it appears to be especially critical in the context of shRNA-mediated inhibition of the highly structured (31) HIV-1 RNA genome.

Second, RNAi-mediated knockdown is highly sensitive to the effective concentration of the si/shRNA. Higher concentrations of shRNA yield increased inhibition (Fig. 3.2 and ref. (8)) but also potentially contribute to saturation of the RNAi machinery, yield off-target effects, and stimulate cytotoxic innate immune responses

(32, 33). We therefore focused on shRNA-mediated inhibition at sub-saturating amounts of transfected shRNA constructs. Importantly, when we probed cytotoxic effects induced by shRNA transduction of SupT1 T cells using a sensitive competitive cell growth assay (39), we found that all but one designed shRNA showed no or minimal reduction in cell growth.

The use of sub-saturating shRNA amounts may also permit the simultaneous expression of several different shRNAs and thereby reduce the chance of developing escape mutants. This is an especially important consideration for clinical applications when targeting rapidly mutating viruses such as HIV-1 with RNAi-based gene therapies (45, 46). Potential shRNA-based therapeutics will have to function in human T-cells, the natural HIV-1 host. While we used human 293T cells in our quantitative virus production inhibition studies, the potent shRNA inhibitors that we identified in 293T cells were generally able to inhibit HIV-1 replication in human SupT1 T-cells, consistent with the observation that determinants of shRNA repression appear to be conserved between evolutionarily disparate cell types (42).

In sum, an extremely simple model is sufficient to identify potent shRNAs that strongly inhibit HIV-1 production in cell culture, even when the shRNAs are used at sub-saturating concentrations. These sequences are strong candidate targets for further evaluation in pre-clinical anti-HIV assays. Critically, our approach emphasizes the profound role of RNA structure in tuning RNAi function and absolutely requires an accurate secondary structure model of the RNA target, as obtainable from SHAPE chemical probing information. The inclusion of partial SHAPE data, corresponding to that obtainable in a single experiment covering ~500 nts, also yields significant

improvements in identification of potent shRNA inhibitors. In the broadest terms, this work shows how profoundly RNA structure influences biological function and emphasizes that, if a high-content model for an RNA fold is obtained experimentally, deep insight into underlying mechanisms can be obtained.

3.4 Methods

3.4.1 Plasmid constructs

The shRNA expression plasmids pSuper-shRNA were constructed as described (47), were verified by sequencing, and were expected to yield 19-nucleotide guide strands upon processing by the cellular miRNA biogenesis pathway. The pLAI plasmid was used to express the HIV-1 isolate LAI (GenBank accession K02013). The pRL-CMV plasmid (Promega) expressing *Renilla* luciferase was co-transfected to control for transfection efficacy. For shRNA titration experiments, the pBluescript plasmid (Stratagene) was used to normalize plasmid amounts (6). To generate lentiviral vectors expressing the shRNAs, the H1-shRNA cassettes were cloned into the lentiviral vector JS1 (pRRLcpptpgkgfppreSsin) (48), as described previously (6). JS1 harbors a GFP cassette for easy identification of transduced cells. For lentivirus production, the JS1 variants were co-transfected with the packaging plasmids pSYNGP, pVSVg, and 250 ng pRSV-rev.

3.4.2 Cell culture

Human embryonic kidney 293T adherent cells were grown in Dulbecco's modified Eagle's medium (DMEM), supplemented with 10% fetal calf serum (FCS), 100 U/ml penicillin, and 100 μg/ml streptomycin in a humidified chamber at 37 °C and 5%

CO_2. The SupT1 T cell line was maintained in Advanced RPMI (Gibco, Carlsbad, USA) supplemented with L-glutamine, 1% FCS, 30 U/ml penicillin and 30 µg/ml streptomycin; cells were maintained at 37 °C and 5% CO_2.

3.4.3 Transfections and HIV-1 production experiments

For the HIV-1 production assay, co-transfections of pLAI and the shRNA vector were performed in a 24-well format. On the first day, 1.5×10^5 293T cells were seeded per well in DMEM without antibiotics. The next day, 250 ng pLAI, 25 ng of shRNA vector, and 1 ng pRL-CMV in Lipofectamine 2000 (Invitrogen, following the manufacturer's protocol) were added. After 48 hours, samples of cell supernatant were taken for CA-p24 ELISA quantification and cells were lysed for measurement of *Renilla* luciferase activity (Renilla Luciferase Assay System, Promega). All transfections were carried out in duplicate and repeated twice. Negative controls were performed using an empty pSuper vector and with an shRNA directed against the firefly luciferase gene. Positive inhibition controls were performed using shRNAs directed against known efficiently repressed HIV-1 targets (LDR9, GagC, Pol1, and Nef19) (6). For shRNA titrations, 250 ng pLAI was co-transfected with 1 to 125 ng pSuper shRNA variants and 1 ng pRL-CMV. Variable amounts of pBluescript were added to yield equivalent DNA concentrations per transfection. All data from transfection experiments were corrected with Factor Correction to compensate for inter-experimental differences (49).

For lentivirus production, 293T cells were seeded in a 6-well-plate format one day prior to transfection to reach 70% confluency and subsequently transfected with 950 ng lentiviral plasmid JS1-shRNA or empty JS1, 600 ng pSYNGP, 330 ng pVSVg, and 250 ng pRSV-rev with Lipofectamine 2000, as described (6).

The HIV-1 virus stock was produced in 293T cells, which were seeded in a T75 flask to yield 70% confluency one day prior to transfection. 40 μg HIV-1 pLAI was transfected following the Lipofectamine 2000 protocol and supernatant was harvested at 48 hours post transfection. Cells were removed by centrifugation (4000 ×g) and the supernatant was aliquoted and stored at -80 °C. The HIV-1 LAI virus stock was quantified for CA-p24 by ELISA measurement.

3.4.4 Lentiviral transduction, HIV- challenge experiments, and competitive cell growth assay.

First, lentiviral titers were determined via titration on SupT1 cells, scoring the percentage of GFP-positive cells by FACS (6). Then, a multiplicity of infection (MOI) of 0.15 was used for transduction of SupT1 T cells (6). Four days later, cells were sorted for GFP-expression by fluorescence-activated cell sorting. 2×10^5 transduced SupT1 cells were challenged with HIV-1 (0.01 or 0.05 ng CA-p24, corresponding to low and high titers, respectively) and monitored daily for up to 90 days by eye and light microscopy to score for cytopathic effects. Supernatants were collected in parallel three times per week to determine CA-p24 levels. Transduced SupT1 cells were screened for a negative impact on the cell growth as induced by lentiviral integration (JS1 control cells) and shRNA expression using the competitive cell growth (CCG) assay (39). In brief, SupT1 cells were transduced to obtain around 30% GFP+ cells. The GFP+/GFP– ratio was analyzed over a 30 day period by FACS measurement, and the ratio at day 3 was normalized to 1. Impact on cell growth can be converted as percentage reduction in cell growth (39).

3.4.5 Free energy calculations

Free energies were calculated using the OligoWalk algorithm in the RNAstructure package (50). OligoWalk takes an RNA secondary structure model as input and considers a bimolecular equilibrium between this folded RNA and every possible complementary RNA oligonucleotide of a user-defined length. The duplex annealing energy ΔG_{duplex} and target unfolding energy ΔG_{target} are calculated. We assumed that shRNAs were cleaved into 19-nt guide strands. The target unfolding energy ΔG_{target} was calculated as the energy required to break base pairs in the input secondary structure model (break local structure option in OligoWalk). The structural model was inputted in connect file (.ct) format. Our SHAPE-based secondary structure model differs from the published model (31) in two regions: the tRNA primer and a heuristically predicted pseudoknot are absent in our input file because OligoWalk only permits single molecule inputs and does not allow pseudoknots. We excluded shRNA target sequences in these two regions because removal of their binding partners resulted in falsely weak target folding energies and falsely strong total binding energies; these regions are highly inaccessible and thus poor candidates for RNAi targets (31). We also created a secondary structure model of the NL4-3 HIV-1 RNA using only thermodynamic parameters by folding the RNA in RNAstructure without any experimental constraints. Perl scripts were created to vary the length and position parameters by changing the input oligomer length and by shifting the target energy window relative to the guide strand binding site, respectively.

3.4.6 Correlation calculations for other algorithms

We calculated correlation coefficients between our 84 member training dataset

and siRNA design algorithm scores using the i-Score Designer tool (http://www.med.nagoya-u.ac.jp/neurogenetics/i_Score/i_score.html) for all methods except for RNAxs and Sirna. Sirna scores were calculated using the online Sfold package (http://sfold.wadsworth.org). We applied the RNAxs algorithm using Perl scripts generously provided by the Hofacker lab. RNAxs predicts accessible sequences that are subsequently further ranked based on the worst scores among six different metrics. Twenty of our 84 sequences were predicted to be good inhibitors by RNAxs. We calculated the linear correlation between the RNAxs ranks of these 20 sequences and our experimental data.

3.4.7 Viral production datasets

We used fully independent datasets to train and test our rules (Fig. 3.3). Our training dataset was comprised of the shRNA sequences previously published by ter Brake *et al*. (6). Viral production values were obtained using relatively low plasmid transfection amounts (20 ng) and sequences were chosen without using si/shRNA selection rules; instead, sequences were selected based on sequence conservation among HIV-1 isolates. A total of 86 HIV-1 sequences were targeted by the shRNAs in this dataset. However, two sequences were, by coincidence, identical (Appendix 1, asterisks). In the current study, we averaged the viral production values for the identical sequences and used the resulting 84 sequences in our correlation calculations. The 26-member test dataset was created as described in the text by applying the two thermodynamic rules identified derived from the training dataset. As with the training dataset, no additional si/shRNA design rules were invoked.

3.5 Acknowledgements

This work was supported by National Institutes of Health grant AI068462 (to K.M.W.) and a Netherlands Organization for Scientific Research Division of Chemical Sciences (NWO-CW) TOP grant (to B.B.). J.T.L. was supported by National Research Service Award F30DA027364 and Medical Scientist Training Program T32GM008719; S.A.K. was supported by a fellowship from the Deutscher Akademischer Austausch Dienst (DAAD); and J.M.W. was a Postdoctoral Fellow of the UNC Lineberger Comprehensive Cancer Center.

3.6 Appendix 1

shRNA training dataset sequences and their relative viral production values. A relative viral production value of 1 represents no inhibition whereas low values represent strong inhibition. Two sequences were coincidentally identical and are denoted by asterisks.

No.	NL4-3 starting position	guide strand core sequence	target RNA sequence	Relative viral production
1	326	CGCACCCAUCUCUCUCCUU	AAGGAGAGAGAUGGGUGCG	0.47
2	327	UCGCACCCAUCUCUCUCCU	AGGAGAGAGAUGGGUGCGA	0.05
3	328	CUCGCACCCAUCUCUCUCC	GGAGAGAGAUGGGUGCGAG	0.06
4	329	UCUCGCACCCAUCUCUCUC	GAGAGAGAUGGGUGCGAGA	0.01
5	330	CUCUCGCACCCAUCUCUCU	AGAGAGAUGGGUGCGAGAG	0.06
6	331	GCUCUCGCACCCAUCUCUC	GAGAGAUGGGUGCGAGAGC	0.32
7	332	CGCUCUCGCACCCAUCUCU	AGAGAUGGGUGCGAGAGCG	0.16
8	333	ACGCUCUCGCACCCAUCUC	GAGAUGGGUGCGAGAGCGU	0.21
9	334	GACGCUCUCGCACCCAUCU	AGAUGGGUGCGAGAGCGUC	0.09
10	1146	ACAUUCUUACUAUUUUAUU	AAUAAAAUAGUAAGAAUGU	0.73
11	1147	UACAUUCUUACUAUUUUAU	AUAAAAUAGUAAGAAUGUA	0.7
12	1363	GCUGUCAUCAUUUCUUCUA	UAGAAGAAAUGAUGACAGC	0.54
13	1364	UGCUGUCAUCAUUUCUUCU	AGAAGAAAUGAUGACAGCA	0.36
14	1365	AUGCUGUCAUCAUUUCUUC	GAAGAAAUGAUGACAGCAU	0.14
15	1366	CAUGCUGUCAUCAUUUCUU	AAGAAAUGAUGACAGCAUG	0.25
16	1623	UCCCUAAAAAAUUAGCCUG	CAGGCUAAUUUUUUAGGGA	0.78
17	1624	UUCCCUAAAAAAUUAGCCU	AGGCUAAUUUUUUAGGGAA	0.75
18	1874	CUGUAUCAUCUGCUCCUGU	ACAGGAGCAGAUGAUACAG	0.03
19	1875	ACUGUAUCAUCUGCUCCUG	CAGGAGCAGAUGAUACAGU	0.14
20	1921	UAUCAUUUUUGGUUUCCAU	AUGGAAACCAAAAAUGAUA	0.37
21	1922	CUAUCAUUUUUGGUUUCCA	UGGAAACCAAAAAUGAUAG	0.45
22	1923	CCUAUCAUUUUUGGUUUCC	GGAAACCAAAAAUGAUAGG	1
23	3719	CUUGUUCAUUUCCUCCAAU	AUUGGAGGAAAUGAACAAG	0.03
24	3720	ACUUGUUCAUUUCCUCCAA	UUGGAGGAAAUGAACAAGU	0.46
25	4085	CUGGCCAUCUUCCUGCUAA	UUAGCAGGAAGAUGGCCAG	0.41
26	4086	ACUGGCCAUCUUCCUGCUA	UAGCAGGAAGAUGGCCAGU	0.22
27	4196	UUUGGGGAUUGUAGGGAAU	AUUCCCUACAAUCCCCAAA	0.55
28	4197	CUUUGGGGAUUGUAGGGAA	UUCCCUACAAUCCCCAAAG	0.67
29	4322	CUUUUCUUUUAAAAUUGUG	CACAAUUUUAAAAGAAAAG	0.73
30	4323	CCUUUUCUUUUAAAAUUGU	ACAAUUUUAAAAGAAAAGG	1.05
31	4324	CCCUUUUCUUUUAAAAUUG	CAAUUUUAAAAGAAAAGGG	0.68
32	4325	CCCCUUUUCUUUUAAAAUU	AAUUUUAAAAGAAAAGGGG	0.69
33	4326	CCCCCUUUUCUUUUAAAAU	AUUUUAAAAGAAAAGGGGG	0.62

34	4327	CCCCCCUUUUCUUUUAAAA	UUUUAAAAGAAAAGGGGGG	0.98	*
35	4328	UCCCCCCUUUUCUUUUAAA	UUUAAAAGAAAAGGGGGGA	0.95	*
36	4329	AUCCCCCCUUUUCUUUUAA	UUAAAAGAAAAGGGGGGAU	0.77	
37	4330	AAUCCCCCCUUUUCUUUUA	UAAAAGAAAAGGGGGGAUU	0.88	
38	4331	CAAUCCCCCCUUUUCUUUU	AAAAGAAAAGGGGGGAUUG	1.04	
39	4332	CCAAUCCCCCCUUUUCUUU	AAAGAAAAGGGGGGAUUGG	0.86	
40	4333	CCCAAUCCCCCCUUUUCUU	AAGAAAAGGGGGGAUUGGG	0.82	
41	4334	CCCCAAUCCCCCCUUUUCU	AGAAAAGGGGGGAUUGGGG	0.76	
42	4335	CCCCCAAUCCCCCCUUUUC	GAAAAGGGGGGAUUGGGGG	1.09	
43	4336	CCCCCCAAUCCCCCCUUUU	AAAAGGGGGGAUUGGGGGG	0.86	
44	4355	UUCUUUCCCCUGCACUGUA	UACAGUGCAGGGGAAAGAA	0.25	
45	4356	AUUCUUUCCCCUGCACUGU	ACAGUGCAGGGGAAAGAAU	0.77	
46	4357	UAUUCUUUCCCCUGCACUG	CAGUGCAGGGGAAAGAAUA	0.18	
47	4430	CCCGAAAAUUUUGAAUUUU	AAAAUUCAAAAUUUUCGGG	0.66	
48	4431	ACCCGAAAAUUUUGAAUUU	AAAUUCAAAAUUUUCGGGU	0.74	
49	4434	UAAACCCGAAAAUUUUGAA	UUCAAAAUUUUCGGGUUUA	0.84	
50	4435	AUAAACCCGAAAAUUUUGA	UCAAAAUUUUCGGGUUUAU	0.73	
51	4436	AAUAAACCCGAAAAUUUUG	CAAAAUUUUCGGGUUUAUU	0.59	
52	4439	UGUAAUAAACCCGAAAAUU	AAUUUUCGGGUUUAUUACA	0.79	
53	4440	CUGUAAUAAACCCGAAAAU	AUUUUCGGGUUUAUUACAG	0.91	
54	4499	CCCCUUCACCUUUCCAGAG	CUCUGGAAAGGUGAAGGGG	0.85	
55	4500	GCCCCUUCACCUUUCCAGA	UCUGGAAAGGUGAAGGGGC	0.83	
56	4501	UGCCCCUUCACCUUUCCAG	CUGGAAAGGUGAAGGGGCA	0.66	
57	4502	CUGCCCCUUCACCUUUCCA	UGGAAAGGUGAAGGGGCAG	0.73	
58	4503	ACUGCCCCUUCACCUUUCC	GGAAAGGUGAAGGGGCAGU	0.65	
59	4504	UACUGCCCCUUCACCUUUC	GAAAGGUGAAGGGGCAGUA	0.54	
60	4505	CUACUGCCCCUUCACCUUU	AAAGGUGAAGGGGCAGUAG	0.67	
61	4506	ACUACUGCCCCUUCACCUU	AAGGUGAAGGGGCAGUAGU	0.23	
62	4507	UACUACUGCCCCUUCACCU	AGGUGAAGGGGCAGUAGUA	0.08	
63	4508	UUACUACUGCCCCUUCACC	GGUGAAGGGGCAGUAGUAA	0.67	
64	4509	AUUACUACUGCCCCUUCAC	GUGAAGGGGCAGUAGUAAU	0.08	
65	4586	CUGCCAUCUGUUUUCCAUA	UAUGGAAAACAGAUGGCAG	0.72	
66	4587	CCUGCCAUCUGUUUUCCAU	AUGGAAAACAGAUGGCAGG	0.91	
67	4588	ACCUGCCAUCUGUUUUCCA	UGGAAAACAGAUGGCAGGU	0.85	
68	4589	CACCUGCCAUCUGUUUUCC	GGAAAACAGAUGGCAGGUG	0.67	
69	5511	GCUUCUUCCUGCCAUAGGA	UCCUAUGGCAGGAAGAAGC	0.48	
70	5512	CGCUUCUUCCUGCCAUAGG	CCUAUGGCAGGAAGAAGCG	0.62	
71	5513	CCGCUUCUUCCUGCCAUAG	CUAUGGCAGGAAGAAGCGG	0.53	
72	5514	UCCGCUUCUUCCUGCCAUA	UAUGGCAGGAAGAAGCGGA	0.15	
73	5515	CUCCGCUUCUUCCUGCCAU	AUGGCAGGAAGAAGCGGAG	0.07	
74	7334	CCCAUAGUGCUUCCUGCUG	CAGCAGGAAGCACUAUGGG	1.14	
75	7335	GCCCAUAGUGCUUCCUGCU	AGCAGGAAGCACUAUGGGC	0.97	
76	7336	AGCCCAUAGUGCUUCCUGC	GCAGGAAGCACUAUGGGCG	0.99	

77	7337	CAGCCCAUAGUGCUUCCUG	CAGGAAGCACUAUGGGCGC	0.77	
78	8599	CCCCUUUUCUUUUAAAAAG	CUUUUUAAAAGAAAAGGGG	0.46	
79	8600	CCCCCUUUUCUUUUAAAAA	UUUUUAAAAGAAAAGGGGG	1.15	
80	8601	CCCCCCUUUUCUUUUAAAA	UUUUAAAAGAAAAGGGGGG	1.07	*
81	8602	UCCCCCCUUUUCUUUUAAA	UUUAAAAGAAAAGGGGGGA	0.96	*
82	8603	GUCCCCCCUUUUCUUUUAA	UUAAAAGAAAAGGGGGGAC	1.2	
83	8604	AGUCCCCCCUUUUCUUUUA	UAAAAGAAAAGGGGGGACU	0.93	
84	8605	CAGUCCCCCCUUUUCUUUU	AAAAGAAAAGGGGGGACUG	1.14	
85	8606	CCAGUCCCCCCUUUUCUUU	AAAGAAAAGGGGGGACUGG	1.05	
86	8607	UCCAGUCCCCCCUUUUCUU	AAGAAAAGGGGGGACUGGA	1.18	

3.7 Appendix 2

shRNA test dataset core sequences designed using the two thermodynamic rules identified in this study and their relative viral production values.

No.	NL4-3 starting position	guide strand core sequence	target RNA sequence	Relative viral production
1	1021	UCACUUCCCCUUGGUUCUC	GAGAACCAAGGGGAAGUGA	0.45
2	1026	CUAUGUCACUUCCCCUUGG	CCAAGGGGAAGUGACAUAG	0.55
3	1033	GUUCCUGCUAUGUCACUUC	GAAGUGACAUAGCAGGAAC	0.1
4	1876	UACUGUAUCAUCUGCUCCU	AGGAGCAGAUGAUACAGUA	0.02
5	1877	AUACUGUAUCAUCUGCUCC	GGAGCAGAUGAUACAGUAU	0.01
6	1882	UUCUAAUACUGUAUCAUCU	AGAUGAUACAGUAUUAGAA	0.02
7	1883	CUUCUAAUACUGUAUCAUC	GAUGAUACAGUAUUAGAAG	0.02
8	1884	UCUUCUAAUACUGUAUCAU	AUGAUACAGUAUUAGAAGA	0.3
9	1959	UCAUACUGUCUUACUUUGA	UCAAAGUAAGACAGUAUGA	0.77
10	3721	UACUUGUUCAUUUCCUCCA	UGGAGGAAAUGAACAAGUA	0.05
11	3722	CUACUUGUUCAUUUCCUCC	GGAGGAAAUGAACAAGUAG	0.02
12	3723	UCUACUUGUUCAUUUCCUC	GAGGAAAUGAACAAGUAGA	0.05
13	3724	AUCUACUUGUUCAUUUCCU	AGGAAAUGAACAAGUAGAU	0.15
14	3725	UAUCUACUUGUUCAUUUCC	GGAAAUGAACAAGUAGAUA	0.27
15	3726	UUAUCUACUUGUUCAUUUC	GAAAUGAACAAGUAGAUAA	0.06
16	4308	UUGUGGAUGAAUACUGCCA	UGGCAGUAUUCAUCCACAA	0.08
17	4380	AUGUCUGUUGCUAUUAUGU	ACAUAAUAGCAACAGACAU	0.29
18	4384	UUGUAUGUCUGUUGCUAUU	AAUAGCAACAGACAUACAA	0.11
19	4386	GUUUGUAUGUCUGUUGCUA	UAGCAACAGACAUACAAAC	0.01
20	4610	GUCUACUUGCCACACAAUC	GAUUGUGUGGCAAGUAGAC	0.06
21	7184	CUUCUCCAAUUGUCCCUCA	UGAGGGACAAUUGGAGAAG	0.59
22	7191	UAAUUCACUUCUCCAAUUG	CAAUUGGAGAAGUGAAUUA	0.4
23	7193	UAUAAUUCACUUCUCCAAU	AUUGGAGAAGUGAAUUAUA	0.19
24	8220	UGUCCCCUCAGCUACUGCU	AGCAGUAGCUGAGGGGACA	0.03
25	8221	CUGUCCCCUCAGCUACUGC	GCAGUAGCUGAGGGGACAG	0.05
26	8302	UCCUUUCCAAGCCCUGUCU	AGACAGGGCUUGGAAAGGA	0.03

3.8 Appendix 3

Free energy values for test shRNA sequences calculated using two 2,500 nucleotide folds of HIV-1 genome segments. SHAPE data were included for only the central 500 nucleotides of each fold.

		Partial fold (2500 nt)		Complete fold without SHAPE (9173 nt)		Complete fold with SHAPE (9173 nt)		Relative viral production
Fold	shRNA	ΔG_{target}	ΔG_{total}	ΔG_{target}	ΔG_{total}	ΔG_{target}	ΔG_{total}	
601-3100	1876	0	-28.4	-4.7	-19.7	0	-27.5	0.02
	1877	0	-27.9	-6.5	-18.7	0	-27	0.01
	1882	0	-26	-9.2	-14.3	0	-26	0.02
	1883	0	-27	-9.5	-16.7	0	-27	0.02
	1884	0	-26	-8.4	-16.8	0	-26	0.30
	1959	0	-21.5	-9.2	-16	0	-27.7	0.77
3201-5700	4308	0	-31.8	-6.7	-15.7	0	-30.9	0.08
	4380	0	-27.6	-4.5	-24.3	0	-27.6	0.29
	4384	0	-27.4	-1.4	-29.2	0	-27.4	0.11
	4386	0	-29	-3.5	-30.8	0	-29	0.01
	4610	0	-28.4	-17	-18.3	0	-32.1	0.06

3.9 References

1. Cruz, JA, and Westhof, E. (2009). The dynamic landscapes of RNA architecture. *Cell* **136**: 604-609.

2. Mello, CC, and Conte, D, Jr. (2004). Revealing the world of RNA interference. *Nature* **431**: 338-342.

3. Wu, L, and Belasco, JG (2008). Let me count the ways: mechanisms of gene regulation by miRNAs and siRNAs. *Mol Cell* **29**: 1-7.

4. Umbach, JL, and Cullen, BR (2009). The role of RNAi and microRNAs in animal virus replication and antiviral immunity. *Genes Dev* **23**: 1151-1164.

5. Wadhwa, R, Kaul, SC, Miyagishi, M, and Taira, K (2004). Vectors for RNA interference. *Curr Opin Mol Ther* **6**: 367-372.

6. ter Brake, O, Konstantinova, P, Ceylan, M, and Berkhout, B (2006). Silencing of HIV-1 with RNA interference: a multiple shRNA approach. *Mol Ther* **14**: 883-892.

7. Naito, Y*, et al.* (2007). Optimal design and validation of antiviral siRNA for targeting HIV-1. *Retrovirology* **4**: 80.

8. McIntyre, GJ, Groneman, JL, Yu, YH, Jaramillo, A, Shen, S, and Applegate, TL (2009). 96 shRNAs designed for maximal coverage of HIV-1 variants. *Retrovirology* **6**: 55.

9. Reynolds, A, Leake, D, Boese, Q, Scaringe, S, Marshall, WS, and Khvorova, A (2004). Rational siRNA design for RNA interference. *Nat Biotechnol* **22**: 326-330.

10. Ui-Tei, K*, et al.* (2004). Guidelines for the selection of highly effective siRNA sequences for mammalian and chick RNA interference. *Nucleic Acids Res* **32**: 936-948.

11. Shabalina, SA, Spiridonov, AN, and Ogurtsov, AY (2006). Computational models with thermodynamic and composition features improve siRNA design. *BMC Bioinformatics* **7**: 65.

12. Huesken, D*, et al.* (2005). Design of a genome-wide siRNA library using an artificial neural network. *Nat Biotechnol* **23**: 995-1001.

13. Matveeva, O*, et al.* (2007). Comparison of approaches for rational siRNA design leading to a new efficient and transparent method. *Nucleic Acids Res* **35**: e63.

14. Tafer, H, *et al.* (2008). The impact of target site accessibility on the design of effective siRNAs. *Nat Biotechnol* **26**: 578-583.

15. Ding, Y, Chan, CY, and Lawrence, CE (2004). Sfold web server for statistical folding and rational design of nucleic acids. *Nucleic Acids Res* **32**: W135-141.

16. Shao, Y, Chan, CY, Maliyekkel, A, Lawrence, CE, Roninson, IB, and Ding, Y (2007). Effect of target secondary structure on RNAi efficiency. *RNA* **13**: 1631-1640.

17. Amarzguioui, M, and Prydz, H (2004). An algorithm for selection of functional siRNA sequences. *Biochem Biophys Res Commun* **316**: 1050-1058.

18. Katoh, T, and Suzuki, T (2007). Specific residues at every third position of siRNA shape its efficient RNAi activity. *Nucleic Acids Res* **35**: e27.

19. Takasaki, S, Kotani, S, and Konagaya, A (2004). An effective method for selecting siRNA target sequences in mammalian cells. *Cell Cycle* **3**: 790-795.

20. Ichihara, M, *et al.* (2007). Thermodynamic instability of siRNA duplex is a prerequisite for dependable prediction of siRNA activities. *Nucleic Acids Res* **35**: e123.

21. Vert, JP, Foveau, N, Lajaunie, C, and Vandenbrouck, Y (2006). An accurate and interpretable model for siRNA efficacy prediction. *BMC Bioinformatics* **7**: 520.

22. Lu, ZJ, and Mathews, DH (2008). Efficient siRNA selection using hybridization thermodynamics. *Nucleic Acids Res* **36**: 640-647.

23. Taxman, DJ, *et al.* (2006). Criteria for effective design, construction, and gene knockdown by shRNA vectors. *BMC Biotechnol* **6**: 7.

24. Schopman, NC, Liu, YP, Konstantinova, P, ter Brake, O, and Berkhout, B (2010). Optimization of shRNA inhibitors by variation of the terminal loop sequence. *Antiviral Res* **86**: 204-211.

25. Xia, T, *et al.* (1998). Thermodynamic parameters for an expanded nearest-neighbor model for formation of RNA duplexes with Watson-Crick base pairs. *Biochemistry* **37**: 14719-14735.

26. Mathews, DH, Sabina, J, Zuker, M, and Turner, DH (1999). Expanded sequence dependence of thermodynamic parameters improves prediction of RNA secondary structure. *J Mol Biol* **288**: 911-940.

27. Deigan, KE, Li, TW, Mathews, DH, and Weeks, KM (2009). Accurate SHAPE-directed RNA structure determination. *Proc Natl Acad Sci U S A* **106**: 97-102.

28. Merino, EJ, Wilkinson, KA, Coughlan, JL, and Weeks, KM (2005). RNA structure analysis at single nucleotide resolution by selective 2'-hydroxyl acylation and primer extension (SHAPE). *J Am Chem Soc* **127**: 4223-4231.

29. Wilkinson, KA*, et al.* (2008). High-throughput SHAPE analysis reveals structures in HIV-1 genomic RNA strongly conserved across distinct biological states. *PLoS Biol* **6**: e96.

30. Mathews, DH, Disney, MD, Childs, JL, Schroeder, SJ, Zuker, M, and Turner, DH (2004). Incorporating chemical modification constraints into a dynamic programming algorithm for prediction of RNA secondary structure. *Proc Natl Acad Sci U S A* **101**: 7287-7292.

31. Watts, JM*, et al.* (2009). Architecture and secondary structure of an entire HIV-1 RNA genome. *Nature* **460**: 711-716.

32. Jackson, AL, and Linsley, PS (2010). Recognizing and avoiding siRNA off-target effects for target identification and therapeutic application. *Nat Rev Drug Discov* **9**: 57-67.

33. Judge, AD, Sood, V, Shaw, JR, Fang, D, McClintock, K, and MacLachlan, I (2005). Sequence-dependent stimulation of the mammalian innate immune response by synthetic siRNA. *Nat Biotechnol* **23**: 457-462.

34. Westerhout, EM, Ooms, M, Vink, M, Das, AT, and Berkhout, B (2005). HIV-1 can escape from RNA interference by evolving an alternative structure in its RNA genome. *Nucleic Acids Res* **33**: 796-804.

35. Schubert, S, Grunweller, A, Erdmann, VA, and Kurreck, J (2005). Local RNA target structure influences siRNA efficacy: systematic analysis of intentionally designed binding regions. *J Mol Biol* **348**: 883-893.

36. Westerhout, EM, and Berkhout, B (2007). A systematic analysis of the effect of target RNA structure an RNA interference. *Nucleic Acids Res* **35**: 4322-4330.

37. Ameres, SL, Martinez, J, and Schroeder, R (2007). Molecular basis for target RNA recognition and cleavage by human RISC. *Cell* **130**: 101-112.

38. Filipowicz, W (2005). RNAi: the nuts and bolts of the RISC machine. *Cell* **122**: 17-20.

39. Eekels JJM, PA, Schut AM, Geerts D, Jeeninga RE, Berkhout B (2011). A competitive cell growth assay for the detection of subtle effects of gene transduction on cell proliferation. *Gene Ther* **19**:1058-1064

40. Yuan, YR, *et al.* (2005). Crystal structure of A. aeolicus argonaute, a site-specific DNA-guided endoribonuclease, provides insights into RISC-mediated mRNA cleavage. *Mol Cell* **19**: 405-419.

41. Tomari, Y, and Zamore, PD (2005). Perspective: machines for RNAi. *Genes Dev* **19**: 517-529.

42. Fellmann, C, *et al.* (2011). Functional identification of optimized RNAi triggers using a massively parallel sensor assay. *Mol Cell* **41**: 733-746.

43. Schwarz, DS, Hutvagner, G, Du, T, Xu, Z, Aronin, N, and Zamore, PD (2003). Asymmetry in the assembly of the RNAi enzyme complex. *Cell* **115**: 199-208.

44. Elbashir, SM, Martinez, J, Patkaniowska, A, Lendeckel, W, and Tuschl, T (2001). Functional anatomy of siRNAs for mediating efficient RNAi in Drosophila melanogaster embryo lysate. *EMBO J* **20**: 6877-6888.

45. von Eije, KJ, ter Brake, O, and Berkhout, B (2008). Human immunodeficiency virus type I escape is restricted when conserved genome sequences are targeted by RNA interference. *Journal of Virology* **82**: 2895-2903.

46. Schopman, NC, ter Brake, O, and Berkhout, B (2010). Anticipating and blocking HIV-1 escape by second generation antiviral shRNAs. *Retrovirology* **7**: 52.

47. Brummelkamp, TR, Bernards, R, and Agami, R (2002). A system for stable expression of short interfering RNAs in mammalian cells. *Science* **296**: 550-553.

48. Seppen, J, Rijnberg, M, Cooreman, MP, and Oude Elferink, RP (2002). Lentiviral vectors for efficient transduction of isolated primary quiescent hepatocytes. *J Hepatol* **36**: 459-465.

49. Ruijter, JM, Thygesen, HH, Schoneveld, OJ, Das, AT, Berkhout, B, and Lamers, WH (2006). Factor correction as a tool to eliminate between-session variation in replicate experiments: application to molecular biology and retrovirology. *Retrovirology* **3**: 2.

50. Mathews, DH, Burkard, ME, Freier, SM, Wyatt, JR, and Turner, DH (1999). Predicting oligonucleotide affinity to nucleic acid targets. *RNA* **5**: 1458-1469.

CHAPTER 4

CONCLUSIONS AND CLINICAL RELEVANCE

4.1 Structural organization of the HIV-1 Gag-Pol frameshift element

In this work, we used LNA binding monitored by SHAPE to confirm a novel SHAPE-directed model of the HIV-1 group M Gag-Pol frameshift domain. The frameshift element comprises a larger, more complex domain of 140 nucleotides than the currently accepted model (1). We further discover that this domain is organized into both highly stable helices that are conserved across biological states, as well as less stable intervening helices that are capable of adopting two alternative conformations. The formation of the domain depends upon the existence of all 140 nucleotides of the domain. This larger domain should therefore be used in future frameshifting studies.

4.2 Structural requirements for effective shRNA targeting of HIV-1

Using a SHAPE-directed secondary structure model of an entire HIV-1 genome, we discovered that extremely simple thermodynamic rules can predict how well sequences within the HIV-1 genome can be inhibited by shRNAs (2). These rules are highly dependent on having an accurate, high resolution secondary structural model of the HIV-1 genome, underscoring the important role model accuracy can play for inferring biological functions. This work additionally makes the novel observation that effectively targeted HIV-1 sequences tend to have an unstructured region that extends

beyond the inhibitor binding site. These results motivate further research into the mechanistic significance of this novel structural requirement.

4.3 Applications to RNA structure probing

The LNA binding method used for verifying the SHAPE-directed frameshift element could be broadly applicable to similar efforts to ascertain the existence of specific RNA helices. This method requires heat-denaturing the RNA in the presence of LNA to achieve sufficient binding to stable helices. This heating step restricts the relevance of this method to RNA regions that can adopt the native fold following heat denaturation. For large RNAs extracted from biological environments, such as the *ex virio* HIV-1 RNA studied here, this necessitates a control experiment where SHAPE reactivities from the heat denatured and refolded RNA are compared to reactivities from the biological state. However, this method should be generally applicable to *in vitro* transcribed RNAs that typically undergo a heat denaturation step prior to refolding and structural interrogation.

Formamide denaturation of RNA analyzed by SHAPE probing could also be broadly useful for studying the relative stabilities of RNA structural elements. Additionally, identification of highly stable structural elements may provide an additional constraint for structure prediction of large, complex RNAs.

4.4 Clinical relevance

The rapid development of drug resistance and lack of an existing cure for HIV make the development of novel therapeutic approaches an important endeavor. In this work, we investigated the RNA genome itself as a new potential antiretroviral target.

We confirm a novel SHAPE-directed model of an important potential target in the HIV-1 genome, the Gag-Pol frameshift element. Frameshifting is the process by which all viral-encoded enzymes are generated and is therefore essential for viral fitness (3). As frameshifting depends critically on the RNA structure of the frameshift domain, this work should provide a more accurate framework for further mechanistic and therapeutic studies of this important drug target.

Additionally, we uncover key structural signatures of HIV-1 target sites that are effectively repressed by RNA interference (RNAi)-based inhibitors. Despite their attractiveness as a potential antiretroviral strategy, RNAi-based therapeutic approaches can saturate the cellular RNAi machinery and trigger undesirable immune-mediated cytotoxicity (4,5). Potential RNAi-based inhibition of HIV-1 should therefore include only the most highly potent shRNAs. The structural characteristics determined in this work should aid in ongoing efforts to identify these highly potent inhibitors. Additionally, some of the potent shRNA sequences identified in this work could be suitable candidates for pre-clinical studies.

4.5 References

1. Watts, J.M., Dang, K.K., Gorelick, R.J., Leonard, C.W., Bess, J.W., Jr., Swanstrom, R., Burch, C.L. and Weeks, K.M. (2009) Architecture and secondary structure of an entire HIV-1 RNA genome. *Nature*, **460**, 711-716.

2. Low, J.T., Knoepfel, S.A., Watts, J.M., ter Brake, O., Berkhout, B. and Weeks, K.M. (2012) SHAPE-directed discovery of potent shRNA inhibitors of HIV-1. *Mol Ther*, **20**, 820-828.

3. Brierley, I. and Dos Ramos, F.J. (2006) Programmed ribosomal frameshifting in HIV-1 and the SARS-CoV. *Virus Res*, **119**, 29-42.

4. Jackson, A.L. and Linsley, P.S. (2010) Recognizing and avoiding siRNA off-target effects for target identification and therapeutic application. *Nature reviews. Drug discovery*, **9**, 57-67.

5. Judge, A.D., Sood, V., Shaw, J.R., Fang, D., McClintock, K. and MacLachlan, I. (2005) Sequence-dependent stimulation of the mammalian innate immune response by synthetic siRNA. *Nat Biotechnol*, **23**, 457-462.